

# The GUAPOS project:

## III. Characterization of the O- and N-bearing complex organic molecules content and search for chemical differentiation

C. Mininni,<sup>1\*</sup> M. T. Beltrán<sup>2</sup>, L. Colzi<sup>3</sup>, V. M. Rivilla<sup>3</sup>, F. Fontani<sup>2</sup>, A. Lorenzani<sup>2</sup>,  
Á. López-Gallifa<sup>3</sup>, S. Viti<sup>4,5</sup>, Á. Sánchez-Monge<sup>6,7,8,9</sup>, P. Schilke<sup>9</sup>, L. Testi<sup>10</sup>

<sup>1</sup> INAF IAPS, Via del Fosso del Cavaliere 100, 00133 Roma, Italy

<sup>2</sup> INAF Osservatorio Astrofisico di Arcetri, Largo E. Fermi 5, 50125 Firenze, Italy

<sup>3</sup> Centro de Astrobiología (CSIC, INTA), Ctra. de Ajalvir, km. 4, Torrejón de Ardoz, E-28850 Madrid, Spain

<sup>4</sup> Leiden Observatory, Leiden University, Huygens Laboratory, Niels Bohrweg 2, NL-2333 CA Leiden, The Netherlands

<sup>5</sup> Department of Physics and Astronomy, University College London, Gower Street, WC1E 6BT, London, UK

<sup>6</sup> Institut de Ciències de l'Espai (ICE, CSIC), Can Magrans s/n, E-08193, Bellaterra, Barcelona, Spain

<sup>7</sup> Institut d'Estudis Espacials de Catalunya (IEEC), Barcelona, Spain

<sup>8</sup> Observatorio Astronómico Nacional (OAN), Alfonso XII, 3 28014, Madrid, Spain

<sup>9</sup> I. Physikalisches Institut, Universität zu Köln, Zùlpicher Str. 77, 50937 Köln, Germany

<sup>10</sup> Dipartimento di Fisica e Astronomia, Università di Bologna, Via Gobetti 93/2, 40122 Bologna, Italy

Received ; accepted

### ABSTRACT

**Context.** The G31.41+0.31 Unbiased ALMA sPectral Observational Survey (GUAPOS) project targets the hot molecular core (HMC) G31.41+0.31 (G31), to unveil the complex chemistry of one of the most chemically rich high-mass star-forming regions outside the Galactic Center (GC).

**Aims.** In the third paper of the project we present a study of nine O-bearing ( $\text{CH}_3\text{OH}$ ,  $^{13}\text{CH}_3\text{OH}$ ,  $\text{CH}_3^{18}\text{OH}$ ,  $\text{CH}_3\text{CHO}$ ,  $\text{CH}_3\text{OCH}_3$ ,  $\text{CH}_3\text{COCH}_3$ ,  $\text{C}_2\text{H}_5\text{OH}$ ,  $\text{aGg}'\text{-(CH}_2\text{OH)}_2$ , and  $\text{gGg}'\text{-(CH}_2\text{OH)}_2$ ) and six N-bearing ( $\text{CH}_3\text{CN}$ ,  $^{13}\text{CH}_3\text{CN}$ ,  $\text{CH}_3^{13}\text{CN}$ ,  $\text{C}_2\text{H}_5\text{CN}$ ,  $\text{C}_2\text{H}_5^{13}\text{CN}$ , and  $\text{C}_2\text{H}_5^{13}\text{CN}$ ) complex organic molecules toward G31. The aim of this work is to characterize the abundances in G31 and to compare them with the values estimated in other sources. Moreover, we search for a possible chemical segregation between O-bearing and N-bearing species in G31, which hosts four compact sources as seen with higher angular resolution data. In the discussion we also include the three isomers of  $\text{C}_2\text{H}_4\text{O}_2$  and the O- and N-bearing molecular species  $\text{NH}_2\text{CHO}$ ,  $\text{CH}_3\text{NCO}$ ,  $\text{CH}_3\text{C(O)CH}_2$ , and  $\text{CH}_3\text{NHCHO}$ , analyzed in previous GUAPOS papers.

**Methods.** Observations were carried out with the interferometer ALMA and cover the entire Band 3 from 84 to 116 GHz ( $\sim 32$  GHz bandwidth) with an angular resolution of  $1.2'' \times 1.2''$  ( $\sim 4400 \text{ au} \times 4400 \text{ au}$ ) and a spectral resolution of  $\sim 0.488 \text{ MHz}$  ( $\sim 1.3\text{--}1.7 \text{ km s}^{-1}$ ). The transitions of the fourteen molecular species have been analyzed with the tool SLIM of MADCUBA to determine the physical parameters of the emitting gas. Moreover, we have analyzed the morphology of the emission of the molecular species.

**Results.** The values of abundances w.r.t  $\text{H}_2$  in G31 range from  $10^{-6}$  to  $10^{-10}$  for the different species. We have compared the abundances w.r.t methanol of O-bearing, N-bearing, and O- and N-bearing COMs in G31 with other twenty-seven sources, including other hot molecular cores inside and outside the Galactic Center, hot corinos, shocked regions, envelopes around young stellar objects, and quiescent molecular clouds, and with chemical models.

**Conclusions.** From the comparison with other sources there is not a unique template for the abundances in hot molecular cores, pointing towards the importance of the thermal history for the chemistry of the various sources. The abundances derived from the chemical models are well in agreement, within a factor ten, with those of G31. From the analysis of the maps we derived the peak positions of all the molecular species toward G31. Different species peak at slightly different positions, and this, together with the different central velocities of the lines obtained from the spectral fitting, point to chemical differentiation of selected O-bearing species.

**Key words.** Astrochemistry – ISM: molecules – Stars: formation – ISM: individual objects: G31.41+0.31

### 1. Introduction

The spectrum of hot molecular cores (HMCs) reveals a very rich chemistry with many rotational transitions of a large number of molecular species, including complex organic molecules (COMs, i.e. molecules containing carbon with 6 or more atoms, Herbst & van Dishoeck 2009). These regions are associated with an evolved phase of high-mass star-formation, when a protostellar object(s) has been already formed in the core, leading to an

increase of the temperature up to a few hundred K. The high temperatures ( $> 100 \text{ K}$ ) reached in HMCs cause the release (by thermal desorption) of the products of the grain-surface reactions into the gas-phase. Furthermore, also the presence of shocks can lead to the release in gas-phase of COMs (e.g. Palau et al. 2011). The study of these regions is important to unveil the chemistry that occurs during the star-formation process and to constrain the chemical pathways responsible for the abundance variations of several species under the physical conditions present in these cores.

\* E-mail: chiara.mininni@inaf.it

The abundances of chemical species in HMCs are influenced by several factors, e.g. the physical conditions of the gas (density,  $n$ , and temperature,  $T$ ), the cosmic rays (CRs) flux, the age of the embedded source, external heating, and protostellar outflows that produce shocked regions (e.g. Garrod 2013; Sipilä et al. 2021). Inhomogeneities in each of these factors potentially can lead to favor, or inhibit, the chemical processes responsible for the formation of different species in different regions of the source. Ultimately, this could also produce chemical differentiation, with the abundances of some molecular species enhanced in regions where others are, on the contrary, less abundant (or even with such low abundances as not to be detected).

As an example, Blake et al. (1987) found spatial segregation between N-bearing molecules and O-bearing molecules toward Orion-KL, the closest high-mass star-forming region. In their study, the emission of N-bearing molecules was detected toward the hot core, while the O-bearing species were detected toward the compact ridge. This has been confirmed by further single-dish and interferometric studies (e.g. Friedel & Snyder 2008; Crockett et al. 2015). However, this simple distinction does not provide the full picture. In fact, several studies have shown that some O-bearing molecular species, e.g. acetone ( $\text{CH}_3\text{COCH}_3$ ), are more co-spatial to N-bearing species than to other O-bearing species, and also among O-bearing species the emitting regions vary (e.g. Widicus Weaver & Friedel 2012; Peng et al. 2013; Feng et al. 2015; Tercero et al. 2018). Tercero et al. (2018) concluded that among O-bearing molecules in Orion-KL, spatial segregation is observed between molecules containing a C-O-C bond and those containing a C-O-H bond. The strong chemical differentiation seen in this source could be a peculiar case, caused by an explosive event in the central region of Orion (e.g. Bally & Zinnecker 2005; Bally et al. 2017), as also indicated by the elongated emission of several molecular species observed by Paganí et al. (2019). However, the chemical differentiation observed in Orion-KL seems to be not unique. Chemical differentiation has also been observed toward other high-mass star-forming regions. Wyrowski et al. (1999), Remijan et al. (2004), Kalenskii & Johansson (2010), Zernickel et al. (2012), Allen et al. (2017), van der Walt et al. (2021), and Peng et al. (2022) observed chemical differentiation between O-bearing and N-bearing molecules toward W3(OH), W51 e1/e2, W75N, G19.61-0.23, NGC 6334I, G35.20-0.74N, CygX-N30 (W75N B), and G9.62+0.19 (especially between core MM8 and MM4), respectively, while Jiménez-Serra et al. (2012) found chemical segregation of selected species in AFGL2591. Jiménez-Serra et al. (2016) also detected chemical differentiation in the cold prestellar core L1544. Bøgelund et al. (2019) have shown that in the high-mass star-forming region AFGL4176 the peak of the emission of O-bearing molecules is offset  $0.2''$  from the peak of N-bearing species, and that the mean excitation temperature is higher for N-bearing than for O-bearing species:  $\sim 120 - 160$  K for O-bearing and  $\sim 190 - 240$  K for N-bearing species. A higher excitation temperature of N-bearing species with respect to O-bearing species were also reported by Widicus Weaver et al. (2017) from the analysis of the spectra of 30 star-forming regions, half of which were HMCs. Recently, Qin et al. (2022) have reported a clear shift of the peak of emission of  $\text{CH}_3\text{OCHO}$  and  $\text{C}_2\text{H}_5\text{CN}$  in 29 hot cores, over a sample of 60, while the other 28 sources show no shift in the position of the two molecules.

In these regions the origin of the observed chemical differentiation is still unclear. Caselli et al. (1993) proposed that the chemical differentiation between the Orion Hot Core and Compact Ridge could be related to differences in the thermal history of the sources. The use of time-dependent evaporation in chemi-

cal models by Viti & Williams (1999) and Viti et al. (2004), and later study such as Suzuki et al. (2018) and Garrod et al. (2022) have confirmed that such a chemical differentiation can be related to differences in the evolution of temperature within the sources. Thus the presence of multiple young stellar objects embedded in high-mass star-forming regions, with different thermal history, could explain the chemical differentiation. Another possible explanation is the presence of accretion shocks at the centrifugal barrier around an accreting protostar, like for example, in the case of the source G328.2551-0.5321 (Csengeri et al. 2019). In summary, the suggested chemical differentiation between O- and N-bearing molecules has not found a clear explanation, and further studies are needed to fully understand the underlying processes.

The target of the G31.41+0.31 (hereafter, G31) Unbiased ALMA sPectral Observational Survey (GUAPOS, Mininni et al. 2020; Colzi et al. 2021) is a well-known and studied HMC located at a distance of 3.75 kpc (Immer et al. 2019) with a luminosity of  $4.4 \times 10^4 L_\odot$  and a gas mass  $M \sim 70 M_\odot$  (respectively from Osorio et al. 2009; Cesaroni 2019, after rescaling the value to the new distance estimate adopted). The core presents a velocity gradient observed in methyl cyanide and other COMs, such as methyl formate, firstly observed by Cesaroni et al. (1994), associated with a rotating toroid (Beltrán et al. 2004, 2005, 2018; Girart et al. 2009; Cesaroni et al. 2010, 2011, 2017). Observations of molecular lines detected the presence of molecular outflows and infall in this source (Girart et al. 2009; Cesaroni et al. 2011; Mayen-Gijon et al. 2014; Beltrán et al. 2018), which is also associated with free-free sources at 0.7 and 1.3 cm (Cesaroni et al. 2010; Beltrán et al. 2021). Previous observations of this source have always revealed a single millimeter compact core, until observations by Beltrán et al. (2021) made with ALMA at 1.4 mm and 3.5 mm and with the Very Large Array (VLA) at 7 mm and 1.3 cm with a resolution of  $\sim 0''.15$ ,  $\sim 0''.075$ ,  $\sim 0''.05$ , and  $\sim 0''.07$ , respectively, have revealed the presence of four separated cores, named source A, B, C, and D (gas masses of  $16 M_\odot$ ,  $15 M_\odot$ ,  $26 M_\odot$ , and  $26 M_\odot$ , respectively) all having part (and in two cases the predominant fraction) of the emission at wavelengths equal or above 7 mm coming from free-free emission. The total mass of the four fragments is  $83 \pm 19 M_\odot$ , consistent within the errors with the mass of  $70 M_\odot$  estimated by Cesaroni (2019). Further high angular resolution analysis (at  $\sim 0.09''$ ) have revealed the presence of infall in all the four cores and the presence of at least six outflows detected in SiO, suggesting that each of the four sources embedded in the Main core drives a molecular outflow (Beltrán et al. 2022a). This reveals that all of the sources are still accreting material. Moreover, complementary large scale observation of  $\text{N}_2\text{H}^+$  performed with IRAM 30m telescope by Beltrán et al. (2022b) have shown that the environment in which G31 has formed is a typical hub-filament system resulting from a cloud-cloud collision.

Previous studies have explored the chemical richness of this HMC (e.g. Beltrán et al. 2005, 2009; Fontani et al. 2007; Isokoski et al. 2013; Calcutt et al. 2014; Rivilla et al. 2017; Gorai et al. 2021; Colzi et al. 2021; García de la Concepción et al. 2022), revealing the presence of several O-bearing and N-bearing COMs. Mininni et al. (2020) presented the GUAPOS project (G31.41+0.31 Unbiased ALMA sPectral Observational Survey), aimed at studying the full  $\sim 32$  GHz bandwidth spectrum at 3 mm, namely the whole Atacama Large Millimeter/submillimeter Array (ALMA) Band 3. The preliminary line identification has revealed an extremely chemically-rich source, with the spectrum showing only a few channels free of molecular line emission. Thus, G31 is an ideal candidate to investigate

**Table 1.** Molecular species discussed in this work.

<i>O</i> -bearing species					
CH <sub>3</sub> OH	<sup>13</sup> CH <sub>3</sub> OH	CH <sub>3</sub> <sup>18</sup> OH	CH <sub>3</sub> CHO	CH <sub>3</sub> OCHO <sup>a</sup>	CH <sub>3</sub> COOH <sup>a</sup>
CH <sub>2</sub> OHCHO <sup>a</sup>	CH <sub>3</sub> OCH <sub>3</sub>	CH <sub>3</sub> COCH <sub>3</sub>	C <sub>2</sub> H <sub>5</sub> OH	aGg'-(CH <sub>2</sub> OH) <sub>2</sub>	gGg'-(CH <sub>2</sub> OH) <sub>2</sub>
<i>N</i> -bearing species					
CH <sub>3</sub> CN	<sup>13</sup> CH <sub>3</sub> CN	CH <sub>3</sub> <sup>13</sup> CN	C <sub>2</sub> H <sub>3</sub> CN	C <sub>2</sub> H <sub>5</sub> CN	C <sub>2</sub> H <sub>5</sub> <sup>13</sup> CN
<i>O</i> - and <i>N</i> -bearing species					
CH <sub>3</sub> NCO <sup>b</sup>	NH <sub>2</sub> CHO <sup>b</sup>	CH <sub>3</sub> C(O)NH <sub>2</sub> <sup>b</sup>	CH <sub>3</sub> NHCHO <sup>b</sup>		

**Notes.** *a*) molecular species previously analyzed by Mininni et al. (2020); *b*) molecular species previously analyzed by Colzi et al. (2021).

the complex chemistry in high-mass star-forming regions outside the Galactic Center (GC), because the extreme conditions in the GC, in terms of interstellar radiation field and cosmic-rays flux can have an impact on the chemistry (see e.g. Bonfand et al. 2019 and references therein). Most of the line emission in G31 arises from COMs, including both *O*-bearing and *N*-bearing species. Therefore, we aim to characterize the emission of these COMs in G31 and to investigate whether spatial segregation between *N*-bearing and *O*-bearing species is present also in this source. A first attempt to search for chemical segregation in G31, together with other five HMCs, was done by Fontani et al. (2007), who found a velocity difference of  $\sim 0.6 \text{ km s}^{-1}$  in the peak velocity of C<sub>2</sub>H<sub>5</sub>CN and CH<sub>3</sub>OCH<sub>3</sub>, with observations taken with the IRAM 30m telescope.

In this paper we analyze the emission of the following COMs: methanol, CH<sub>3</sub>OH, and its isotopologues <sup>13</sup>CH<sub>3</sub>OH and CH<sub>3</sub><sup>18</sup>OH, acetaldehyde, CH<sub>3</sub>CHO, dimethyl ether, CH<sub>3</sub>OCH<sub>3</sub>, acetone, CH<sub>3</sub>COCH<sub>3</sub>, ethanol, C<sub>2</sub>H<sub>5</sub>OH, ethylene glycol, aGg'-(CH<sub>2</sub>OH)<sub>2</sub> and gGg'-(CH<sub>2</sub>OH)<sub>2</sub> conformers, methyl cyanide, CH<sub>3</sub>CN, and its isotopologues <sup>13</sup>CH<sub>3</sub>CN and CH<sub>3</sub><sup>13</sup>CN, vinyl cyanide, C<sub>2</sub>H<sub>3</sub>CN, and ethyl cyanide, C<sub>2</sub>H<sub>5</sub>CN, and its isotopologue, C<sub>2</sub>H<sub>5</sub><sup>13</sup>CN. Moreover, in the discussion we will consider the results from the analysis presented in this paper together with the results from the analysis of the three isomers of C<sub>2</sub>H<sub>4</sub>O<sub>2</sub> by Mininni et al. (2020), and of the *O*- and *N*-bearing COMs formamide, NH<sub>2</sub>CHO, methyl isocyanate, CH<sub>3</sub>NCO, acetamide, CH<sub>3</sub>C(O)CH<sub>2</sub>, and *N*-methylformamide, CH<sub>3</sub>NHCHO, by Colzi et al. (2021) (see Table 1). In this work, molecules including both *O* and *N* atoms will be considered as a separate class in the discussion, unlike other works in literature where those molecules are considered among the *N*-bearing species. This choice would allow us, in case of observed spatial segregation in G31, to better investigate the behavior of these species and study whether their emission is spatially closer to that of *O*-bearing species or *N*-bearing species.

In Section 2 we present the observations; in Section 3 we present the spectral analysis (Sect. 3.1) and the analysis of the maps (Sect. 3.2); in Section 4 we discuss the results of both the analysis of the spectrum and of the maps, to reveal the possible presence of chemical differentiation between *N*-bearing and *O*-bearing species, or between selected molecular species. We also compare the abundances of COMs in G31 with other high-mass and low-mass star-forming regions, shocked regions and quiescent clouds, and with chemical models. In section 5 we summarize the main conclusions.

## 2. Observations

The observations were carried out with ALMA during Cycle 5, (project 2017.1.00501.S, P.I.: M. T. Beltrán), and cover the complete spectral range of ALMA band 3, between 84.05 GHz and 115.91 GHz ( $\sim 32 \text{ GHz}$  bandwidth), with a spectral resolution

of  $\sim 0.488 \text{ MHz}$  ( $\sim 1.3 - 1.7 \text{ km s}^{-1}$ ). The observations were divided in nine correlator configurations, and for each of them four contiguous basebands were observed. The data have been firstly presented by Mininni et al. (2020), where it is possible to find more details about the spectral setups, the flux and phase calibrators, and the configurations of the correlators. The uncertainties in the flux calibration are  $\sim 5\%$  (from Quality Assessment 2 reports), in good agreement with ALMA Band 3 flux uncertainties reported by Bonato et al. (2018).

The data were calibrated and imaged with CASA<sup>1</sup> (the *Common Astronomy Software Applications* package, McMullin et al. 2007). The maps were created using a robust parameter of Briggs (1995) set equal to 0 and a common restoring synthesized beam of  $1''.2 \times 1''.2$ . The noise of the maps, *rms*, varies between 0.5 mJy/beam and 1.9 mJy/beam.

For all the observed basebands, the spectra have been extracted from an area equal to the size of the beam and centered toward the peak of the continuum. Mininni et al. (2020) described the steps made to align the spectra of the different correlator configurations and basebands to obtain the final spectrum. The baseline has been analyzed by Colzi et al. (2021) with the software STATCONT (Sánchez-Monge et al. 2018), to statistically determine the value of the continuum level and then subtract it from the spectrum.

Both from the alignment of the different spectra and from the statistical analysis performed with STATCONT on the final spectrum, the uncertainty on the determination of the continuum level is  $\sim 11\%$ .

## 3. Analysis

### 3.1. Spectral fitting

The baseline-subtracted spectrum has been analyzed with the SLIM (Spectral Line Identification and Modeling) tool within the MADCUBA package<sup>2</sup> (Martín et al. 2019). The spectroscopic data were taken from the Cologne Database for Molecular Spectroscopy<sup>3</sup> (CDMS, Müller et al. 2001, 2005) and from the JPL database of molecular spectroscopy<sup>4</sup> (Pickett et al. 1998). Precise reference papers for each molecule analyzed in this work are given in Appendix A. For all the molecular species, except C<sub>2</sub>H<sub>5</sub>CN and its isotopologues, and C<sub>2</sub>H<sub>5</sub>OH, the partition function from the chosen catalog has either been calculated using also the first excited states or their contribution has been estimated to be less than 3% at temperatures below 300 K. For

<sup>1</sup> <https://casa.nrao.edu>

<sup>2</sup> Madrid Data Cube Analysis (MADCUBA) is a software developed in the Center of Astrobiology (Madrid) to visualize and analyze data cubes and single spectra: <https://cab.inta-csic.es/madcuba/>

<sup>3</sup> <https://cdms.astro.uni-koeln.de>

<sup>4</sup> <https://spec.jpl.nasa.gov/>

**Table 2.** Results of the spectral analysis

species	$T_{\text{ex}}$ [K]	$N$ [ $10^{17}\text{cm}^{-2}$ ]	$X$ [ $10^{-8}$ ]	FWHM [ $\text{km s}^{-1}$ ]	$V-V_0$ [ $\text{km s}^{-1}$ ]
<i>O-bearing species</i>					
$\text{CH}_3\text{OH } v_t = 1$	$208 \pm 24$	$100 \pm 12$	$100 \pm 30$	$8.3 \pm 0.4$	$0.94 \pm 0.15$
$^{13}\text{CH}_3\text{OH}$	$152 \pm 20$	$9.6 \pm 1.7$	$10 \pm 3$	$7.2 \pm 0.3$	$1.09 \pm 0.10$
$\text{CH}_3^{18}\text{OH}$	$153 \pm 20$	$2.4 \pm 0.4$	$2.4 \pm 0.7$	$7.0^a$	$1.28 \pm 0.13$
$\text{CH}_3\text{OH}^b$		$800 \pm 130$	$800 \pm 200$		
$\text{CH}_3\text{CHO}$	$82 \pm 20$	$0.34 \pm 0.16$	$0.34 \pm 0.18$	$7.5^a$	$0.45 \pm 0.11$
$\text{CH}_3\text{OCH}_3$	$98 \pm 11$	$8.1 \pm 1.0$	$8 \pm 2$	$7.0^a$	$1.07 \pm 0.06$
$\text{CH}_3\text{COCH}_3$	$170 \pm 21$	$5.6 \pm 1.3$	$5.6 \pm 1.4$	$7.0^a$	$0.84 \pm 0.06$
$\text{C}_2\text{H}_5\text{OH}$	$119 \pm 14$	$4.7 \pm 0.6^c$	$4.7 \pm 1.2^c$	$7.02 \pm 0.09$	$1.00 \pm 0.04$
$\text{aGg}'-(\text{CH}_2\text{OH})_2$	$120^a$	$1.45 \pm 0.17$	$1.5 \pm 0.4$	$7.2^a$	$0.48 \pm 0.06$
$\text{gGg}'-(\text{CH}_2\text{OH})_2$	$120 \pm 28$	$0.87 \pm 0.19$	$0.9 \pm 0.3$	$7.2^a$	$1.0 \pm 0.2$
<i>N-bearing species</i>					
$\text{CH}_3\text{CN } v_8 = 1$	$197 \pm 51$	$3.2 \pm 0.9$	$3.2 \pm 1.1$	$8.6 \pm 0.3$	$0.68 \pm 0.15$
$^{13}\text{CH}_3\text{CN}$	$111 \pm 17$	$0.073 \pm 0.011$	$0.073 \pm 0.019$	$7.1 \pm 0.2$	$0.95 \pm 0.09$
$\text{CH}_3^{13}\text{CN}$	$54 \pm 10$	$0.069 \pm 0.011$	$0.069 \pm 0.018$	$7.2 \pm 0.5$	$0.97 \pm 0.19$
$\text{CH}_3\text{CN}^d$		$2.7 \pm 0.4$	$2.7 \pm 0.7$		
$\text{C}_2\text{H}_3\text{CN}$	$104 \pm 17$	$0.21 \pm 0.04$	$0.21 \pm 0.06$	$9.7^a$	$1.05 \pm 0.15$
$\text{C}_2\text{H}_5\text{CN}$	$83 \pm 10$	$0.56 \pm 0.08^e$	$0.56 \pm 0.14^e$	$7.94 \pm 0.13$	$1.37 \pm 0.06$
$\text{C}_2\text{H}_5^{13}\text{CN}$	$126 \pm 37$	$0.042 \pm 0.012^f$	$0.042 \pm 0.017^f$	$6.0^a$	$1.8 \pm 0.3$
$\text{C}_2\text{H}_5\text{CN}^g$		$1.6 \pm 0.5$	$1.6 \pm 0.7$		

**Notes.** Excitation temperature,  $T_{\text{ex}}$ , column density,  $N$ , abundance w.r.t  $\text{H}_2$ ,  $X$ , FWHM, and velocity with respect to  $V_0 = 96.5 \text{ km s}^{-1}$ ,  $V-V_0$ . The abundances have been calculated using  $N_{\text{H}_2} = (1.0 \pm 0.2) \times 10^{25} \text{ cm}^{-2}$  (Mininni et al. 2020); to calculate the corrected values of column densities and abundances of a species from the analysis of its  $^{13}\text{C}$  or  $^{18}\text{O}$  isotopologue, we have used the ratios  $^{12}\text{C}/^{13}\text{C} = 37 \pm 12$  (from Yan et al. 2019) and  $^{16}\text{O}/^{18}\text{O} = 333 \pm 143$  (from Wilson & Rood 1994), considering the Galactocentric distance of G31,  $D_{\text{GC}} = 5.02 \text{ kpc}$ ; a): quantity kept fixed during the fitting; b) corrected values for column density and abundance derived from the values of  $\text{CH}_3^{18}\text{OH}$ ; c) corrected for the partition function factor at 119 K of 1.13; d) corrected values for column density and abundance derived from the values of  $^{13}\text{CH}_3\text{CN}$  (the estimate using the  $\text{CH}_3^{13}\text{CN}$  would give corrected  $N = (2.6 \pm 0.4) \times 10^{17} \text{ cm}^{-2}$  and  $X = 2.6 \pm 0.7$ ); e) corrected for the partition function factor at 83 K of 1.062; f) corrected for the partition function factor at 126 K of 1.24; g) corrected values for column density and abundance derived from the values of  $\text{C}_2\text{H}_5^{13}\text{CN}$ .

$\text{C}_2\text{H}_5\text{CN}$  and its isotopologues the correction factor to the partition function is given in CDMS<sup>5</sup> and is above 3% from 75 K. Therefore, for  $\text{C}_2\text{H}_5\text{CN}$  and  $\text{C}_2\text{H}_5^{13}\text{CN}$  we will apply the correction factor (interpolated at the T resulting from the fit) to the column density obtained with MADCUBA. In the case of  $\text{C}_2\text{H}_5\text{OH}$  the partition function has been calculated in CDMS (and also in JPL) taking into account the ground vibrational states only, but correction factors for temperatures different than 150 K (correction factor 1.24 Müller et al. 2016) are not available yet. Because the temperature for this specie in G31 is of 119 K (see Sect. 3.1.1), we have not applied any correction. Once the correction factors will be available, authors who want to use the column density value of G31 can rescale it.

The analysis has been performed after a preliminary line identification, where we identified a large fraction of the molecular species present in the source (see Appendix E of Colzi et al. 2021). This line identification has allowed us to check the presence of possible blendings of the transitions of the molecular species analyzed in this work with other species and thus to select the most unblended transitions for each species to be used to constrain the fit.

To obtain the physical parameters of the molecular emission (column density,  $N$ , excitation temperature,  $T_{\text{ex}}$ , full width at half maximum, FWHM, and velocity,  $V_{\text{LSR}}$ ) from the data, we assumed a single temperature component that fills the beam and used the AUTOFIT tool of MADCUBA-SLIM, which finds the

best agreement, minimizing the  $\chi^2$ , between the observed spectra and the predicted LTE model, taking into account also the optical depth. The simultaneous fit of multiple transitions for each molecular species allows the determination of  $V_{\text{LSR}}$  with an error smaller than the resolution in velocity of the spectrum ( $\sim 1.5 \text{ km/s}$ ). During the fit we have assumed local thermodynamic equilibrium (LTE), justified by the high density of G31 (rough estimate of  $n \sim 10^8 \text{ cm}^{-3}$ , Mininni et al. 2020). The molecular species analyzed in this work are listed in Table 1.

The emission of methanol, methyl cyanide, and ethyl cyanide is optically thick, especially for the first two species, thus we have analyzed their isotopologues with  $^{13}\text{C}$  and for  $\text{CH}_3\text{OH}$  and  $\text{CH}_3\text{CN}$ , also the transitions of the torsionally or vibrationally excited state (as already done in Colzi et al. 2021). To obtain the column density of the species containing only  $^{12}\text{C}$  (i.e. the most abundant isotopologues) we have multiplied the column density derived from the analysis of the  $^{13}\text{C}$  isotopologues for the  $^{12}\text{C}/^{13}\text{C}$  ratio. We have adopted a value of  $^{12}\text{C}/^{13}\text{C} = 37 \pm 12$ , derived from Yan et al. (2019), and of  $^{16}\text{O}/^{18}\text{O} = 333 \pm 143$ , derived from Wilson & Rood (1994), using the galactocentric distance of 5.02 kpc for G31<sup>6</sup>.

For all the species we have assumed an error of 11% on the values of  $N$  and  $T_{\text{ex}}$ , to reflect the uncertainty on the level of continuum. The best LTE fit results are listed in Table 2. For the species in which the fit of the spectra has been performed in previous GUAPOS papers (see Table 1, Mininni et al. 2020; Colzi

<sup>5</sup> <https://cdms.astro.uni-koeln.de/classic/predictions/catalog/archive/EtCN/Qvib.txt>

<sup>6</sup> Calculated from the heliocentric distance of 3.75 kpc (Immer et al. 2019)

et al. 2021) the results are listed in Table 3. The abundances have been calculated using the column density of  $H_2$  derived in the first paper of the GUAPOS project,  $N_{H_2} = (1.0 \pm 0.2) \times 10^{25} \text{ cm}^{-2}$  (Mininni et al. 2020).

From the spectral analysis it is already possible to infer preliminary hints of chemical differentiation. These are given by a clear difference in  $V_{LSR}$ , FWHM or  $T_{ex}$  between O-bearing species, N-bearing species, and O- and N-bearing species or between selected molecular species. A difference in  $V_{LSR}$  would be the strongest indication, since different embedded sources - resolved with observations at angular resolution of  $\sim 0''.075$  by Beltrán et al. (2021) - would likely have slightly different velocities, while the values of FWHM or  $T_{ex}$  could be affected not only by a different position of the peak of the emission, but also by a different size of the emission. Figure 1 shows the mean maps of the emission of the different molecular species (see Sect. 3.2 for more details), where we can see that different species have different emission sizes.

The parameters derived from the best fit are given in Table 2, where instead of the absolute value of  $V_{LSR}$ , we give the difference  $V - V_0$  using as reference velocity  $V_0 = 96.5 \text{ km s}^{-1}$  (Beltrán et al. 2018).

### 3.1.1. O-bearing species

**Methanol:**  $CH_3OH$ ,  $^{13}CH_3OH$ , and  $CH_3^{18}OH$  We have not been able to constrain the fit of  $CH_3OH v=0$  with a single temperature component. This could be connected both to the presence of a temperature gradient in the source, studied with high angular resolution data by Beltrán et al. (2018), and to the high abundance of this molecular species that leads to optically thick transitions. In Fig. B.1 we show some of the brightest transitions and we can see that some of them, which correspond to those having the lowest energies of the lower level and the highest Einstein coefficients, show inverse P Cygni profiles. Taking into account that the minimum maximum recoverable scale of the GUAPOS project is  $\sim 11''$ , it is unlikely that the filtering effect has a major impact. Therefore, we conclude that the inverse P-Cygni profiles observed are due to the high optical depths of the lines and the presence of infall in the core, as reported by Beltrán et al. (2018, 2022a).

We have analyzed the emission of the rotational transitions in the first torsionally excited state,  $v_t = 1$ , whose transitions have optical depths estimated by MADCUBA between 0.1 and 0.2, with only two exceptions. We have constrained the fit using the 7 unblended transitions available (see Table C.1). Both the observed spectrum and the synthetic spectrum from the best fit are given in Fig. B.2. The best-fit parameters are given in Table 2. These parameters are consistent with those found by the best visual agreement of the simulated spectrum with the transitions of  $CH_3OH$  in the ground state (Fig. B.1), with the exception of the column density which is a factor  $\sim 2$  larger.

We also analyzed the emission of  $^{13}CH_3OH$  and  $CH_3^{18}OH$ , whose lines are optically thin. The 12 unblended transitions used to constrain the fit of  $^{13}CH_3OH$  are given in Table C.2, and the result of the fit is given in Table 2. The 12 transitions cover a broad range in  $E_U$  (energy of the upper state), from  $\sim 7 \text{ K}$  to  $\sim 330 \text{ K}$ . The spectrum of the transitions used to constrain the fit and the synthetic spectrum obtained with the best-fit parameters are given in Fig. B.3. The column density for  $CH_3OH$  derived multiplying the column density from the fit of  $^{13}CH_3OH$  for the ratio  $^{12}C/^{13}C=37$  is  $(3.6 \pm 0.7) \times 10^{19} \text{ cm}^{-2}$ .

For  $CH_3^{18}OH$  we selected 15 transitions to constrain the fit (see Table C.3). These transitions cover a broad range in  $E_U$

from  $\sim 5 \text{ K}$  to  $\sim 330 \text{ K}$ . The spectrum of the transitions used to constrain the fit and the synthetic spectrum obtained with the best-fit parameters are given in Fig. B.4, while the results of the fit are given in Table 2. The column density for  $CH_3OH$  derived multiplying the column density from the fit of  $CH_3^{18}OH$  for the ratio  $^{16}O/^{18}O=333$  is  $(8.0 \pm 1.3) \times 10^{19} \text{ cm}^{-2}$ . The estimate of the column density of  $CH_3OH v_t=1$  is a factor 4 and 8 lower than the one derived for  $CH_3OH$  from  $^{13}CH_3OH$  and  $CH_3^{18}OH$ , respectively. This could be due to the different energy range covered by the transitions of the species: for  $CH_3OH v_t=1$  the available transitions have all  $E_U/k_B > 300 \text{ K}$ , while for the two isotopologues the transitions used to constrain the fit are in the range  $\sim 5 \text{ K} - \sim 330 \text{ K}$ . From the second-last column of Table C.2, and C.3 we can see that  $CH_3^{18}OH$  is optically thinner than  $^{13}CH_3OH$ , therefore in the discussion we will adopt the value derived from  $CH_3^{18}OH$  for the column density of  $CH_3OH$ , since the two isotopologues give estimates of column density that differs by a factor 2.

**Acetaldehyde:**  $CH_3CHO$  We have detected 10 unblended lines of acetaldehyde. The spectral parameters of the corresponding transitions are given in Table C.4. The energy range of the upper level covers only energy transitions below  $100 \text{ K}$  ( $\sim 15 - 80 \text{ K}$ ). To help the fitting algorithm to converge, we have fixed the FWHM to  $7.5 \text{ km s}^{-1}$ . This value has been selected visually evaluating the best value of FWHM simulating the emission of individual transitions. The plot of the selected transitions with superimposed the synthetic spectrum calculated using the parameters from the best fit is given in Fig. B.5. The estimate of  $T_{ex}$  is lower than the mean value found for the rest of the molecular species, and could be due to the small range of  $E_U$  of the unblended transitions. To quantify how the column density would change if the temperature were higher, we have performed a fit using the same transitions and fixing the value of  $T_{ex}$  to  $120 \text{ K}$ . The column density value from this fit is  $6.0 \times 10^{16} \text{ cm}^{-2}$ , changing by a factor of  $\sim 2$  from the column density derived from the best fit.

**Dimethyl ether:**  $CH_3OCH_3$  We have identified 33 unblended transitions of dimethyl ether covering energies from  $\sim 11 \text{ K}$  to  $\sim 230 \text{ K}$ , listed in Table C.5. To help the fitting algorithm to converge, we have fixed the FWHM to  $7.0 \text{ km s}^{-1}$ , the best value after a visual inspection. The results of the fit are given in Table 2. We found  $T_{ex} \sim 100 \text{ K}$ , only slightly lower than that of some other molecular species. However, this value of  $T_{ex}$  is likely real and not biased by the selected transitions used for the fit, since in the fit we have included several high-energy transitions. We have plotted the synthetic spectrum derived with the parameters of the best fit in Fig. B.6.

**Acetone:**  $CH_3COCH_3$  We have identified 38 unblended transitions of acetone, covering energies from  $\sim 15 \text{ K}$  to  $\sim 170 \text{ K}$ , listed in Table C.6. We report the best-fit parameters in Table 2. A small number of transitions of  $CH_3COCH_3$  are overestimated by the best-fit model. A better agreement over the whole spectra would require a more accurate description of the temperature gradient of the source G31, as already seen for other molecular species (e.g. methanol, Sect. 3.1.1.1). In Fig. B.7 and B.8 we plot the most unblended transitions and the synthetic spectra obtained with the parameters of the fitting procedure.

**Table 3.** Results from the spectral and map analysis for O-bearing and O- and N-bearing COMs analyzed in previous papers of the GUAPOS project.

species	$T_{\text{ex}}$ [K]	$N$ [ $10^{17} \text{ cm}^{-2}$ ]	$X$ [ $10^{-8}$ ]	FWHM [ $\text{km s}^{-1}$ ]	$V-V_0$ [ $\text{km s}^{-1}$ ]	R.A. (J2000) [18h 47m s]	Dec. (J2000) [-01° 12' '' ]	reference
<i>O-bearing species</i>								
CH <sub>3</sub> OCHO	221 ± 27	20 ± 4	20 ± 6	6.8 <sup>a</sup>	1.1 <sup>a</sup>	34.318	46.054	Mininni et al. (2020)
CH <sub>3</sub> COOH	250 ± 50 <sup>b</sup>	6.4 ± 2.1 <sup>b</sup>	6.2 ± 1.9 <sup>b</sup>	7.8 <sup>a</sup>	0.0 <sup>a</sup>	34.315	46.057	Mininni et al. (2020)
CH <sub>2</sub> OHCHO	128 ± 17	0.5 ± 0.09	0.50 ± 0.14	8.8 <sup>a</sup>	0.0 <sup>a</sup>	34.309	46.094	Mininni et al. (2020)
<i>O- and N-bearing species</i>								
CH <sub>3</sub> NCO <sup>c</sup>	91 ± 37	1.2 ± 0.3	1.2 ± 0.4	7.15 <sup>a</sup>	0.5 <sup>a</sup>	34.313	46.054	Colzi et al. (2021)
NH <sub>2</sub> CHO <sup>d</sup>	150 <sup>a</sup>	1.7 ± 0.6	1.7 ± 0.7	8.6 <sup>a</sup>	0.5 <sup>a</sup>	34.316	46.062	Colzi et al. (2021)
CH <sub>3</sub> C(O)NH <sub>2</sub>	285 ± 50	0.8 ± 0.4	0.8 ± 0.4	6.2 ± 0.4	0.2 <sup>a</sup>	34.310	46.044	Colzi et al. (2021)
CH <sub>3</sub> NHCHO	285 <sup>a</sup>	0.37 ± 0.16	0.37 ± 0.17	7.0 <sup>a</sup>	0.0 <sup>a</sup>	34.307	46.058	Colzi et al. (2021)

**Notes:** The coordinates of the center of the emission of each species are derived from the task *imfit* applied to the mean maps. *a*): quantity kept fixed during the fitting procedure; *b*): for CH<sub>3</sub>COOH Mininni et al. (2020) found that the values of  $T_{\text{ex}}$ ,  $N$ , and  $X$  could range from 200–299 K,  $4.3 - 8.4 \times 10^{17} \text{ cm}^{-2}$ , and  $4.3 - 8 \times 10^{-8}$ , respectively. The values reported in this table are the mean values of the ranges, while the errors cover the entire ranges. *c*) from CH<sub>3</sub>NCO  $v_b = 1$ ; *d*) from NH<sub>2</sub><sup>13</sup>CHO, where the column density has been multiplied by the factor  $^{12}\text{C}/^{13}\text{C} = 37$ .

**Ethanol: C<sub>2</sub>H<sub>5</sub>OH** We have detected 39 unblended transitions of ethanol. They are listed in Table C.7 and plotted in Figs. B.9 and B.10. The energy of the upper level  $E_U$  covers a broad range,  $\sim 17 - 350$  K. The results of the best fit are given in Table 2, and the synthetic spectrum obtained using the parameters of the best fit is plotted in red over the observed spectrum in Figs. B.9 and B.10. We note that the partition function from the catalog considers the ground vibrational state only, so we used the values of the energy of the vibrational states by Durig et al. (2011) to calculate the correction factor. For a temperature of 119 K the correction factor is 1.13, which we applied to correct the value of the column density.

**Ethylene glycol: gGg'-(CH<sub>2</sub>OH)<sub>2</sub> and aGg'-(CH<sub>2</sub>OH)<sub>2</sub>** We have detected 7 most unblended transitions of gGg'-(CH<sub>2</sub>OH)<sub>2</sub>, covering energies from  $\sim 20$  K to  $\sim 120$  K. They are listed in table C.8 and plotted in Fig. B.11. To help the fitting algorithm to converge, we have fixed the FWHM to  $7.2 \text{ km s}^{-1}$ . This value has been selected visually evaluating the best value of FWHM simulating the emission of individual transitions. The results of the best fit are given in Table 2, and the synthetic spectrum obtained using the parameters of the best fit is plotted in red over the observed spectrum in Fig B.11.

For the conformer aGg'-(CH<sub>2</sub>OH)<sub>2</sub>, already detected in G31 by Rivilla et al. (2017), we have detected 20 unblended transitions. They are listed in Table C.9 and plotted in Fig. B.12. The energy of the upper level  $E_U$  covers an extremely narrow range between  $\sim 15 - 55$  K, with the exception of two transitions with  $E_U \sim 100$  K (at 85522.2 and 96259.9 MHz), which are blended with other transitions of lower energy of the same specie. Therefore, to help the fitting algorithm to converge, we have fixed the excitation temperature to the value found for gGg'-(CH<sub>2</sub>OH)<sub>2</sub> and the FWHM to  $7.2 \text{ km s}^{-1}$ . The results of the best fit are given in Table 2, and the synthetic spectrum obtained using the parameters of the best fit is plotted in red over the observed spectrum in Fig B.12. The ratio of the column density of the conformers aGg'/gGg' is  $> 1$ .

**Isomers of C<sub>2</sub>H<sub>4</sub>O<sub>2</sub>: CH<sub>3</sub>OCHO, CH<sub>3</sub>COOH, and CH<sub>2</sub>OHCHO**  
The analysis of methyl formate, acetic acid and glycolaldehyde has been presented in Mininni et al. (2020). For CH<sub>3</sub>OCHO, CH<sub>3</sub>COOH, and CH<sub>2</sub>OHCHO Mininni et al. (2020) selected 22, 14, and 12 most unblended transitions to perform the fit, respectively. These transitions covered a range in the energy of the up-

per level from  $\sim 20$  K to 220 K for CH<sub>3</sub>OCHO,  $\sim 20$  K to 270 K for CH<sub>3</sub>COOH, and  $\sim 20$  K to 190 K for CH<sub>2</sub>OHCHO. The transitions were optically thin. The physical parameters derived from the spectral fitting are summarized in Table 3.

### 3.1.2. N-bearing species

**Methyl cyanide: CH<sub>3</sub>CN, <sup>13</sup>CH<sub>3</sub>CN, and CH<sub>3</sub><sup>13</sup>CN** The transitions of CH<sub>3</sub>CN  $v=0$  present within the observed GUAPOS bandwidth are CH<sub>3</sub>CN( $5_K - 4_K$ ) and CH<sub>3</sub>CN( $6_K - 5_K$ ). For CH<sub>3</sub>CN  $v=0$ , it has not been possible to have a good convergence of the fit because the majority of the transitions ( $K=0, 1, \text{ and } 2$ ) have high optical depths. The spectrum is plotted in Fig. B.13. Note that the lower K-components show a lower synthesised beam temperature than higher-K components, a clear indication that the lower-K transitions are optically thick.

Because of the optical thickness of the ground transitions, we have analyzed the vibrationally excited ones, CH<sub>3</sub>CN  $v_8 = 1$ . The transitions used to constrain the fit are given in Table C.10. The results of the fit are given in Table 2, and the synthetic spectrum obtained with the best-fit parameters is given in Fig. B.14.

As for CH<sub>3</sub>OH, we have also analyzed the emission of the isotopologue <sup>13</sup>CH<sub>3</sub>CN. We detected only 5 transitions not affected by blending, with  $E_U$  between  $\sim 10$  K and  $\sim 80$  K. They are reported in Table C.11. The results of the best fit are given in Table 2 and plotted in Fig. B.15. Moreover, we have analyzed the isotopologue CH<sub>3</sub><sup>13</sup>CN. We detected only 3 unblended transitions, listed in Table C.12. The range in  $E_U$  is in between  $\sim 40$  and  $\sim 80$  K. The results of the best fit are given in Table 2, and the spectrum is shown in Fig. B.16. The value of  $T_{\text{ex}}$  is lower than that of CH<sub>3</sub>CN  $v_8 = 1$  and <sup>13</sup>CH<sub>3</sub>CN. This discrepancy in  $T_{\text{ex}}$  could be due to the different (lower) energy range of the transitions used in the fit. Fixing the value of  $T_{\text{ex}}$  to 100 K the column density from the fitting procedure would be  $8.1 \times 10^{15} \text{ cm}^{-2}$ , consistent inside the errors with the estimate leaving  $T_{\text{ex}}$  as a free parameter. From the second-last column of Table C.11 and C.12 we can see that <sup>13</sup>CH<sub>3</sub>CN is optically thinner than CH<sub>3</sub><sup>13</sup>CN, therefore in the discussion we will adopt the value derived from <sup>13</sup>CH<sub>3</sub>CN for the column density of CH<sub>3</sub>CN.

**Vinyl cyanide:  $C_2H_3CN$**  We have detected 11 unblended transitions of vinyl cyanide. They are listed in Table C.13 and plotted in Fig. B.17. The range in  $E_U$  is limited, between  $\sim 30$  and  $\sim 90$  K. To better constrain the fit, we have fixed the value of the FWHM to  $9.7 \text{ km s}^{-1}$ . The results of the best fit, given in Table 2, show a low value of  $T_{\text{ex}}$ . Such a low value could be a consequence of the low energy of the unblended transitions used for the fit.

**Ethyl cyanide:  $C_2H_5CN$  and  $C_2H_5^{13}CN$**  We have detected 16 unblended transitions of  $C_2H_5CN$ , listed in Table C.14. The  $E_U$  ranges from  $\sim 25$  to  $\sim 120$  K. The best-fit parameters are given in Table 2 and the associated synthetic spectrum is shown in Fig. B.18. The column density given in Table 2 has been multiplied by the correction factor of the partition function at 83 K, which is 1.062. For  $C_2H_5CN$  the low value of  $T_{\text{ex}}$  could be a consequence of the low energy of the unblended transitions used for the fit. From Table C.14 we can see that some transitions have optical depths very close to unity, and in two cases above it. Therefore, the emission from this species is not optically thin and we decided to analyze also its isotopologue  $C_2H_5^{13}CN$  to have a better estimate of its column density and abundance.

We have detected only 7 most unblended transitions of  $C_2H_5^{13}CN$ , listed in Table C.15. The  $E_U$  ranges from  $\sim 30$  to  $\sim 110$  K. The intensity of the lines is weak, if compared to the intensity of the other COMs considered. The best-fit parameters are given in Table 2 and the associated synthetic spectrum is shown in Fig. B.18. The column density given in Table 2 has been multiplied by the correction factor of the partition function at 126 K, which is 1.24.

### 3.1.3. O- and N-bearing species

The COMs formamide,  $NH_2CHO$ , methyl isocyanate,  $CH_3NCO$ , acetamide,  $CH_3C(O)NH_2$ , and N-methylformamide,  $CH_3NHCHO$  have been analyzed by Colzi et al. (2021). The physical parameters derived from the spectral fitting are summarized in Table 3.  $NH_2CHO$  was detected in the ground vibrational state and in the first vibrational state. Moreover,  $NH_2^{13}CHO$  was detected and analyzed. The values listed in Table 3 refer to the analysis of  $NH_2^{13}CHO$ , whose emission is more optically thin, where the column density had been corrected for a factor  $^{12}C/^{13}C = 37 \pm 12$ . For  $CH_3NCO$ , the ground vibrational state and the first vibrational state were detected and analyzed, with  $^{13}CH_3NCO$  tentatively detected because most of the transitions are contaminated or blended with transitions of other species. The values listed in Table 3 are derived from the analysis of the first vibrational state.  $CH_3C(O)NH_2$  ground state and excited states ( $v_t = 1, 2$ ) had optical depths  $\ll 1$ , and were fitted together. For its isomer  $CH_3NHCHO$ , only transitions of the ground state were detected, and to perform the fit the temperature was fixed to the value derived for  $CH_3C(O)NH_2$ .

### 3.2. Analysis of the maps

To create the emission maps of the species analyzed in this work we selected for each of them eight of the most unblended lines<sup>7</sup>, or the maximum number possible for those species for which we

detect less than eight (mostly) unblended transitions to fit. We selected the lines for the maps among the range of the detected unblended transitions, to include both low and high upper state energy transitions  $E_U$ . The transitions corresponding to the selected lines are indicated in the last column of Tables C.1–C.15. To create the maps of each line, we first removed the continuum emission from the cubes using the software STATCONT (Sánchez-Monge et al. 2018), and then created the integrated intensity (moment 0) map for each line.

To obtain a mean map of each species, we normalized each map to its peak intensity and then averaged all the maps of the same species together, using the task *immath* of CASA. Normalizing the different maps before averaging allows us to give the same weight to every map, and to obtain a mean map in which the FWHM of the emitting region is not biased by the brightest lines.

The mean maps obtained with this procedure are shown in Fig. 1, and have been fitted with a 2D Gaussian using the task *imfit* inside CASA to obtain the position of the peak of emission and the size of the emission. The results of the 2D Gaussian fit are given in Table 4 for the molecular species analyzed in this paper. The maps of the emission of the three isomers of  $C_2H_4O_2$  and of O- and N-bearing species have been already presented in Mininni et al. (2020) and Colzi et al. (2021) and are not shown in this paper, while we have reported the position of the center of emission in Table 3. The coordinates of the peak of the emission for  $CH_3NCO$ ,  $NH_2CHO$ ,  $CH_3C(O)NH_2$ , and  $CH_3NHCHO$  have been derived from the maps presented in Colzi et al. (2021) following the same methodology presented in this paper and in Mininni et al. (2020).

The task *imfit* produces also the maps of the residuals (i.e. the difference between the maps in input and the best 2D models computed by the task itself), where it is possible to understand if there is some molecular emission not coming from the main core (modeled with the 2D Gaussian), but from more extended regions or from secondary spots in the map. The maps of the residuals are plotted in Fig. 2.

## 4. Discussion

### 4.1. Emission morphology

From the mean maps of the different species shown in Fig. 1, we can see that the emission of all the COMs analyzed is centered toward the continuum peak of the HMC, with some species showing a shape not perfectly Gaussian. Among the O-bearing species, we can see that the contours of the emission of  $CH_3CHO$  are shifted towards the South-West direction when compared to the contours of the continuum, unlike all the other O-bearing species ( $aGg'-(CH_2OH)_2$  shows a less significant shift in the same direction). Looking at the residual maps, in Fig. 2 (note that Fig. 2 shows a region  $\sim 2$  times larger around G31 w.r.t Fig.1), we can see that  $CH_3CHO$ ,  $CH_3OCH_3$ ,  $^{13}CH_3CN$ ,  $C_2H_3CN$ , and  $C_2H_5CN$  show a residual emission over 10 times the *rms* value (cyan contours). In all cases, this emission is concentrated in the West and South-West edge of the main core (excluding residuals in the center of the core), with the exception of  $CH_3CHO$  that shows very diffuse emission in all the envelope around the HMC, with spots over the 10 *rms* level, and a prominent more compact spot to the southern edge of the G31 main core. The origin of the residual emission could be related to the presence of outflows in the East–West direction and South West–North East direction on the plane of the sky, like those mapped in SiO by Beltrán et al. (2018, 2022a). The more extended morphology

<sup>7</sup> What here is called a *line* can be the result of the emission of multiple transitions of the same species, whose frequencies are closer than FWHM/2. Therefore, eight lines do not necessarily correspond to only eight transitions.

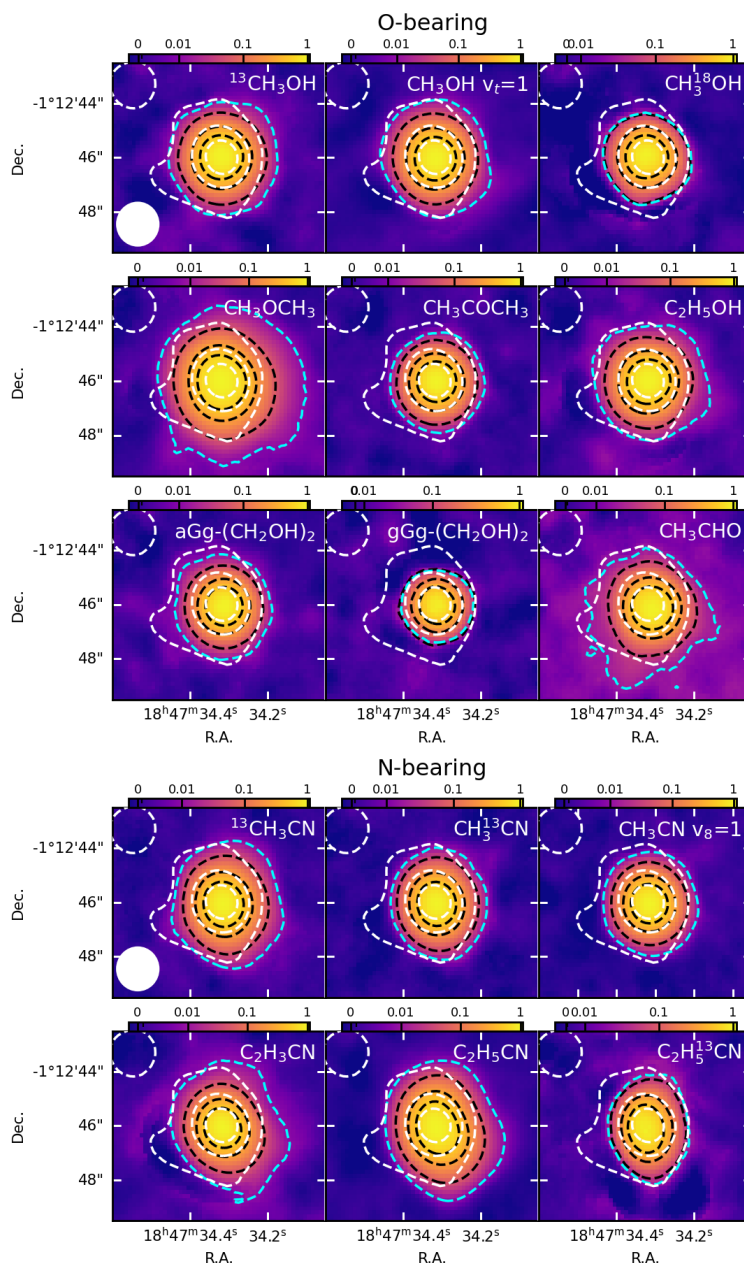


**Fig. 1.** Mean maps of the species for which the analysis has been presented in this work for the first time (see Table 1). The mean maps have been obtained averaging the normalized maps of different transitions of the same species, therefore they are in arbitrary units with peak close to unity. In dashed white line we have plotted the contour levels of the continuum map at 150, 60, and 20 times the value of  $rms = 0.8 \text{ mJy beam}^{-1}$  (from Mininni et al. 2020). The black dashed lines delimit the contour where the intensity of the mean map drops to 50%, 25%, and 5% of the peak value. The 2D Gaussian fit ellipse to the emission is coincident with the inner black-dashed contour (50% level) for all the molecular species. The cyan dashed line delimits the contour where the intensity of the mean map is equal to 10 times the  $rms$  of the map. The size of the  $1''.2$  beam is indicated in the lower-left corner of the first panel on top-left.

of  $\text{CH}_3\text{CHO}$  can not be explained only by the fact that we cover lower energy transition, even if the extended emission is more prominent in the lower energy state moment maps of  $\text{CH}_3\text{CHO}$  among those used to do the mean-moment map. In fact, in Appendix D we show the moment-0 maps of a low-energy transition for each molecular species, and none of the other moment-0 maps shows such an extended emission, even in the low-energy transitions.

All these regions are located outside the  $1''.2$  central region from which we extracted the spectrum. It has to be noted that the

brightness peak of this residual emission is two orders of magnitude below the brightness toward the main core (which is 1 in the units of Figs. 1 and 2, from the methodology used to obtain the mean maps described in Section 3.2), thus the column densities in those regions are expected to be accordingly smaller than those derived toward the center of the G31 HMC.



**Table 4.** Results of the 2D Gaussian fit to the mean maps.

species	$E_U/k_B$ [K]	R.A. (J2000) [18h 47m s]	Dec. (J2000) [-01° 12' '' ]	$\theta_{\max} \times \theta_{\min}$ [''x'']	P.A. [deg]
<i>O-bearing species</i>					
$\text{CH}_3\text{OH } v_t = 1$	$\sim 300 - 800$	34.317	46.035	$1.61 \times 1.58$	34
$^{13}\text{CH}_3\text{OH}$	$\sim 10 - 330$	34.319	45.990	$1.66 \times 1.62$	88
$\text{CH}_3^{18}\text{OH}$	$\sim 10 - 330$	34.323	45.972	$1.62 \times 1.57$	75
$\text{CH}_3\text{CHO}$	$\sim 10 - 70$	34.308	46.132	$1.64 \times 1.60$	50
$\text{CH}_3\text{OCH}_3$	$\sim 10 - 220$	34.319	46.052	$1.98 \times 1.83$	22
$\text{CH}_3\text{COCH}_3$	$\sim 10 - 170$	34.314	46.026	$1.51 \times 1.49$	80
$\text{C}_2\text{H}_5\text{OH}$	$\sim 10 - 280$	34.318	46.018	$1.67 \times 1.62$	113
aGg <sup>+</sup> -(CH <sub>2</sub> OH) <sub>2</sub>	$\sim 15 - 55$	34.312	46.068	$1.46 \times 1.44$	57
gGg <sup>+</sup> -(CH <sub>2</sub> OH) <sub>2</sub>	$\sim 25 - 115$	34.313	46.035	$1.42 \times 1.38$	66
<i>N-bearing species</i>					
$\text{CH}_3\text{CN } v_8 = 1$	$\sim 530 - 590$	34.316	46.047	$1.47 \times 1.43$	24
$^{13}\text{CH}_3\text{CN}$	$\sim 10 - 80$	34.313	46.069	$1.71 \times 1.57$	16
$\text{CH}_3^{13}\text{CN}$	$\sim 40 - 80$	34.314	46.056	$1.64 \times 1.51$	14
$\text{C}_2\text{H}_3\text{CN}$	$\sim 20 - 80$	34.316	46.084	$1.57 \times 1.41$	35
$\text{C}_2\text{H}_5\text{CN}$	$\sim 20 - 120$	34.311	46.094	$1.95 \times 1.59$	20
$\text{C}_2\text{H}_5^{13}\text{CN}$	$\sim 20 - 100$	34.322	46.105	$1.77 \times 1.41$	7

**Notes:** Results of the 2D Gaussian fit only for the species for which the analysis has been presented in this work for the first time (see Table 1), performed with the task *imfit*. In the second column we give the range in upper state energy  $E_u$  of the transitions used to create the mean maps.

#### 4.2. Positions of molecular species emission peaks

To reveal the existence of chemical differentiation inside this source we calculated the position of the peak of the emission for each molecular species, as described in Section 3.2. The coordinates are reported in Table 4 for the molecular species analyzed in this work, and in Table 3 for the molecular species presented in Mininni et al. (2020) and Colzi et al. (2021).

The distances between the center of emission of the different species are smaller than the beam (1''2), therefore the spatial resolution of the observations is not sufficient to have conclusive results about the possible presence of spatial segregation for some classes of molecular species, or for selected species.

Nevertheless, to give a visual reference to be confirmed by higher angular resolution data, in Fig. 3 we have plotted the continuum emission of the GUAPOS data and the high-resolution continuum data at 3.5 mm from Beltrán et al. (2021), marking with blue stars the position of the peaks of the emission of O-bearing COMs, with red stars the peak positions of N-bearing COMs, and with green stars the peak positions of O- and N-bearing COMs. The error bars on the peak position given in the output of the 2D Gaussian fit performed with the *imfit* tool of CASA are below the dimension of the maps pixel for all the molecular species. This is due to the fact that the emission is nearly Gaussian, with the residual values contributing at maximum for a factor of 3% with respect to the peak emission. These error bars were not plotted in the right-side panel of Fig. 3 because they are of the same dimension as the star-shaped markers used for the peak positions. The highest spatial separation is found among the majority of O-bearing molecules and the position of the peak of  $\text{CH}_3\text{CHO}$  and  $\text{CH}_2\text{OHCHO}$ . In the previous section, we also highlighted a shift of the contour of emission of  $\text{CH}_3\text{CHO}$  w.r.t. the emission of the other O-bearing COMs.

Only one molecular species,  $\text{C}_2\text{H}_5^{13}\text{CN}$ , is located far away from the position of any of the cores.

#### 4.3. Spectral analysis

The abundances w.r.t  $\text{H}_2$  of the COMs analyzed in G31 range from  $\sim 10^{-6}$  ( $\text{CH}_3\text{OH}$ ) to  $\sim 10^{-10}$  ( $\text{C}_2\text{H}_5^{13}\text{CN}$ ). In the case of methanol, the estimate for the column density derived from the  $v_t = 1$  state is a factor 4 lower than the estimate obtained from the  $^{13}\text{C}$  isotopologue, rescaled with the factor  $^{12}\text{C}/^{13}\text{C}$ , indicating that the fit of the torsionally excited state might still be affected by optical depths effect. On the contrary, the estimates for the column density and abundance of  $\text{CH}_3\text{CN}$  from the  $v_8 = 1$  state and from its two  $^{13}\text{C}$  isotopologues are well consistent within the errors, despite the large differences in  $T_{\text{ex}}$  derived for the three species. The estimate for ethyl cyanide from the  $^{13}\text{C}$  isotopologue is a factor 2 larger than the estimate from the emission of the main isotopologue, whose transitions have optical depths close to 1 (see Table C.14). Figure 4 shows the comparison among the physical parameters of the molecular species presented in this work, together with  $\text{CH}_3\text{OCHO}$ ,  $\text{CH}_3\text{COOH}$ ,  $\text{CH}_2\text{OHCHO}$ ,  $\text{CH}_3\text{NCO}$ ,  $\text{NH}_2\text{CHO}$ ,  $\text{CH}_3\text{C}(\text{O})\text{NH}_2$ , and  $\text{CH}_3\text{NHCHO}$  from Mininni et al. (2020) and Colzi et al. (2021). We have summarized the data for these molecular species in Table 3.

As discussed in Section 3.1, the analysis of the physical parameters of the emitting gas derived from the spectral analysis of the COMs can give further hints on the presence of a chemical differentiation. The most robust hints are given by a difference in the peak velocity of different molecular species. Other authors have reported also clear differences in  $T_{\text{ex}}$  among O-bearing and N-bearing species (e.g. Bøgelund et al. 2019), but in G31 part of the discrepancy in  $T_{\text{ex}}$  might be due to the difference in size of the emitting regions of different species, since there are clear evidences of a temperature gradient inside this HMC (Beltrán et al. 2005).

From Fig. 4,  $T_{\text{ex}}$  does not show a clear difference between O-bearing species, N-bearing species, and O- and N-bearing species. The values of  $T_{\text{ex}}$  range from  $\sim 60$  K to  $\sim 300$  K depending on the molecular species. This broad range might be

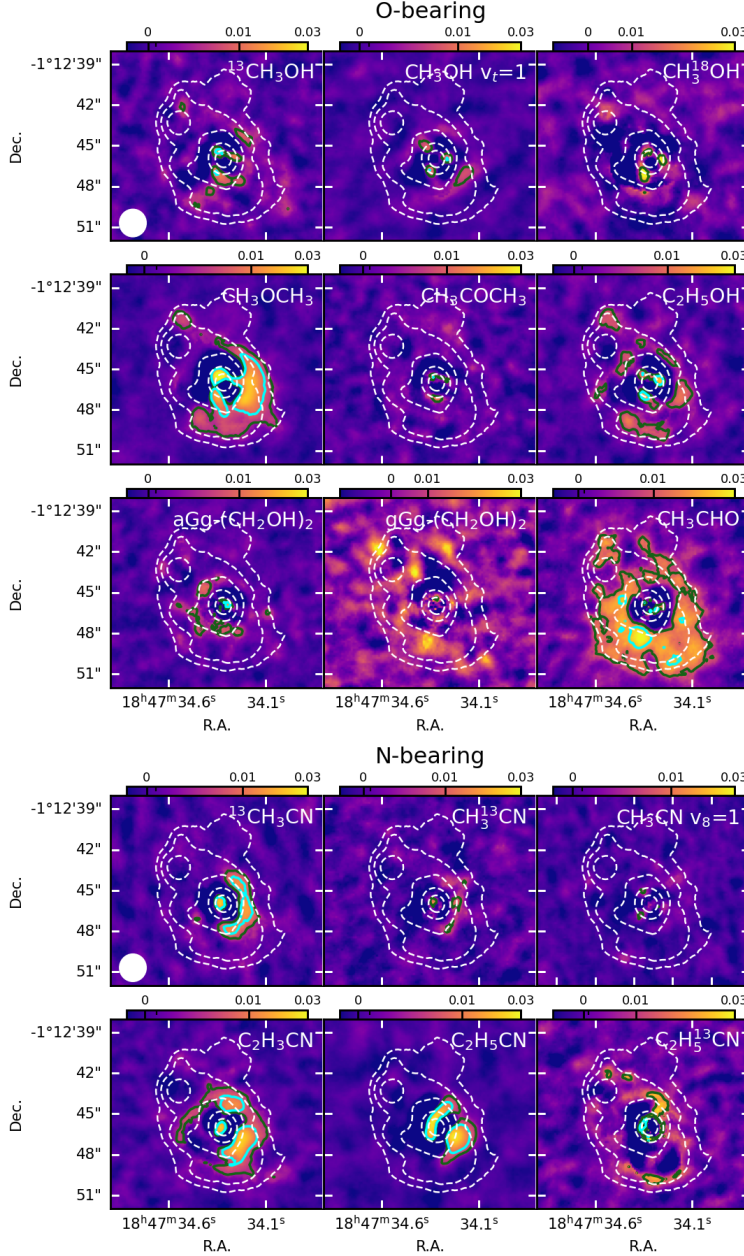


**Fig. 2.** Maps of residuals after the 2D Gaussian fit to the mean maps, for the species for which the analysis has been presented in this work for the first time (see Table 1). The size of the plotted region is larger than that plotted in Fig. 1. The units are the arbitrary units of the mean maps. In white we have plotted the contours level of the continuum map at 150, 60, 20, 10, and 5 times the value of  $rms = 0.8 \text{ mJy beam}^{-1}$  (from Mininni et al. 2020). The green and cyan solid lines delimit the contours of the regions where the emission in the residual map is larger than 5 and 10 times the  $rms$ , respectively. The size of the  $1''.2$  beam is indicated in the lower-left corner of the top-left panel.

due to emission arising from different regions (see Table 4), or from the fact that some of the molecular species presented in this work do not have unblended transitions with  $E_U > 100 \text{ K}$ , leading to possibly underestimated excitation temperatures.

The FWHM values vary between 6 to  $10 \text{ km s}^{-1}$ , not showing any particular trend among molecular species. On the contrary in  $V-V_0$  we can see that the majority of the molecular species have  $V-V_0$  close to  $1 \text{ km s}^{-1}$  (including  $\text{C}_2\text{H}_5^{13}\text{CN}$  since its value is consistent with  $\sim 1 \text{ km s}^{-1}$  inside the large uncertainty), with the exception of  $\text{CH}_3\text{CHO}$ ,  $\text{CH}_3\text{COOH}$ ,  $\text{CH}_2\text{OHCHO}$ ,  $\text{aGg}'-(\text{CH}_2\text{OH})_2$ , and the four O- and N-bearing

species  $\text{CH}_3\text{NCO}$ ,  $\text{NH}_2\text{CHO}$ ,  $\text{CH}_3\text{C}(\text{O})\text{NH}_2$ , and  $\text{CH}_3\text{NHCHO}$ . In particular,  $\text{CH}_3\text{COOH}$ ,  $\text{CH}_2\text{OHCHO}$ ,  $\text{CH}_3\text{C}(\text{O})\text{NH}_2$ , and  $\text{CH}_3\text{NHCHO}$  have  $V-V_0 \sim 0.2-0.0 \text{ km s}^{-1}$ , while for  $\text{CH}_3\text{CHO}$ ,  $\text{CH}_3\text{NCO}$ ,  $\text{aGg}'-(\text{CH}_2\text{OH})_2$ , and  $\text{NH}_2\text{CHO}$  the difference is less pronounced, with  $V-V_0 \sim 0.5 \text{ km s}^{-1}$ . A previous study by Fontani et al. (2007) found a discrepancy of  $\sim 0.6 \text{ km s}^{-1}$  between the velocity of  $\text{C}_2\text{H}_5\text{CN}$  and  $\text{CH}_3\text{OCH}_3$  in G31 from IRAM 30m telescope data, while in the interferometric data at a resolution of  $1''.2$  presented in this paper the discrepancy is of only  $\sim 0.3 \text{ km s}^{-1}$ .

From these results and the tentative analysis on the positions of the peak of the emission presented in the previous section,

there are possible indications of chemical differentiation. The stronger indications are for  $\text{CH}_3\text{CHO}$  and  $\text{CH}_2\text{OHCHO}$ , which have the largest separation in the peak position from all the other O-bearing species, and a discrepancy also in  $V-V_0$ , while for  $\text{CH}_3\text{COOH}$ ,  $\text{aGg}^-(\text{CH}_2\text{OH})_2$  and O- and N-bearing species we have a difference in peak velocity, but not a clear difference in peak position in our  $1''2$  resolution maps.

#### 4.4. Comparison with other sources

In Fig. 5 we plot the abundances w.r.t. methanol of the O-bearing, N-bearing, and O- and N-bearing species detected in G31, together with the abundances of the same COMs found in other twenty-seven sources in literature. These include the HMCs SgrB2 N2/N3/N4/N5 (Belloche et al. 2016; Bonfand et al. 2019), AFGL4176 (Bøgelund et al. 2019), NGC 6334I-SMA1 and SMA2 (Zernickel et al. 2012), Orion-KL observation toward the methyl formate peak (MF), ethylene glycol peak (EG), and ethanol peak (ET) of O-bearing molecules only (Tercero et al. 2018), the protostellar source CygX-N30 in the position 1, 2, and 3 analyzed by van der Walt et al. (2021), G35.20–0.74N A and B3, the two most-chemically rich sources in G35.20–0.74N analyzed by Allen et al. (2017), the two most chemically rich sources MM8 (HMC) and MM4 (late HMC or hyper compact HII region) in the source G9.62+0.19 (Peng et al. 2022), the low-mass hot corinos IRAS 16293-2422 A and B (Jørgensen et al. 2016; Manigand et al. 2020), NGC 1333 IRAS 4A2 (López-Sepulcre et al. 2017; Taquet et al. 2019), B1-c and S68N (van Gelder et al. 2020; Nazari et al. 2021), the positions of accretion shocks in high-mass star-forming regions G328.2551-0.532 A and B (Csengeri et al. 2019), the shocked region L1157-B1 associated with a low-mass young stellar object (YSO, Lefloch et al. 2017; Codella et al. 2009), the inner envelope position around a HMC precursor G328.2551-0.532-env (Csengeri et al. 2019), and the molecular cloud G+0.693-0.027 (Requena-Torres et al. 2006, 2008; Zeng et al. 2018; Biz-zocchi et al. 2020; Rodríguez-Almeida et al. 2021; Rivilla et al. 2022; Sanz-Novo et al. 2022) located toward the North-East of the SgrB2 star-forming complex in the Central Molecular Zone (CMZ). Even though we are interested in discussing the relative abundances of these molecular species in different sources, in Fig. 5 we also report the absolute value of the abundance (or the column density if abundance was not available) of methanol in each source. For G+0.693-0.027 we rescaled all the abundances to the value of  $N(\text{H}_2)$  derived by Martín et al. (2008), used in all the recent works toward this source.

Before comparing the abundances in G31 with the other HMCs, we have checked the presence of a possible beam-dilution effect in the column density and abundance estimates of G31, given that the beam of  $1''2$  is probing a linear scale of  $\sim 4400$  AU, larger than the scale resolved in some of the other studies toward HMCs we included in the comparison. Colzi et al. (2021) presented the emission maps of O- and N-bearing species at a higher resolution of  $0''2$  and confirmed that for these species the emission fills the beam of  $1''2$  of the data analyzed in this paper. Moreover, the estimate of the column density from the high-resolution data is consistent within a factor 2 with the estimate obtained with our resolution. We also compared the column density of  $\text{CH}_3\text{OCHO}$  derived from the data at  $1''2$  with that obtained from the analysis of the data at  $0''2$  presented by Beltrán et al. (2018), and they are well in agreement. Beltrán et al. (2018) also show the high-resolution map of the integrated emission of  $\text{CH}_3\text{CN}$  (12-11)  $K=2$  which covers the region of our  $1''2$  beam. Therefore, we conclude that possible beam-dilution effects will

be minor if present, and will not affect the discussion below.

Comparing the abundances found in G31 and in the other high-mass protostars we found discrepancies: the four sources located toward the GC (SgrB2 N2/N3/N4/N5) show in general higher abundances - of around  $\sim 1$  order of magnitude or more in most of the cases - of O-bearing species (only  $\text{CH}_3\text{OCHO}$  and  $\text{C}_2\text{H}_5\text{OH}$ ) and especially of N-bearing species and O- and N-bearing species. This enrichment of COMs with respect to methanol toward the GC may be the result of the peculiar conditions found in those regions, such as the cosmic-ray ionization rate being a factor  $\sim 50$  larger than the solar neighborhood value (Bøgelund et al. 2019), that can lead to enhance the efficiency of some chemical pathways. For AFGL4176 we found a good general agreement of the abundances with those in G31, with some smaller differences for  $\text{CH}_3\text{CHO}$ ,  $\text{aGg}^-(\text{CH}_2\text{OH})_2$ ,  $\text{gGg}^-(\text{CH}_2\text{OH})_2$ , and  $\text{C}_2\text{H}_3\text{CN}$ . The absolute abundance of methanol w.r.t.  $\text{H}_2$  in this source is higher by a factor  $\sim 4$  than the value derived for G31. The abundances of  $\text{CH}_3\text{OCH}_3$ ,  $\text{CH}_3\text{COCH}_3$ , and  $\text{NH}_2\text{CHO}$  toward NGC 6334I-SMA1 show clear discrepancies with the values in G31, while  $\text{CH}_3\text{OCHO}$  and  $\text{C}_2\text{H}_5\text{CN}$  abundances are well in agreement. Also in the case of NGC 6334I-SMA2, only half of the COMs selected have abundances comparable to those found in G31. The comparison with the three positions in Orion-KL is limited to only five O-bearing species:  $\text{CH}_3\text{OCH}_3$ ,  $\text{C}_2\text{H}_5\text{OH}$ ,  $\text{CH}_3\text{OCHO}$ ,  $\text{CH}_3\text{COOH}$ , and  $\text{aGg}^-(\text{CH}_2\text{OH})_2$ . The best agreement is found between G31 and the ethylene glycol peak (EG see Tercero et al. 2018). Also in the case of CygX-N30 (van der Walt et al. 2021) the comparison is limited only to four species:  $\text{CH}_3\text{OCH}_3$ ,  $\text{C}_2\text{H}_5\text{OH}$ ,  $\text{CH}_3\text{OCHO}$ , and  $\text{CH}_3\text{CN}$ . The abundances w.r.t. methanol of the three O-bearing species do not vary significantly toward the 3 positions identified by van der Walt et al. (2021) and are in good agreement with the values measured toward G31, while the abundance of  $\text{CH}_3\text{CN}$  presents more variability with position 1 having a value close to G31.

The abundances of  $\text{C}_2\text{H}_5\text{OH}$ ,  $\text{CH}_3\text{OCHO}$ ,  $\text{CH}_3\text{CN}$ ,  $\text{C}_2\text{H}_5\text{CN}$ , and  $\text{NH}_2\text{CHO}$  in G35.20–0.74N A by Allen et al. (2017) are comparable with those in G31, while the other molecular species are in general more abundant than in G31. For G35.20-0.74N B3, the abundance of  $\text{C}_2\text{H}_3\text{CN}$  is similar to that of G31, while the abundance of  $\text{C}_2\text{H}_5\text{CN}$  is clearly lower. The rest of the molecular species have abundances w.r.t. methanol close to those found for G35.20–0.74N A. The abundances in cores MM8 and MM4 of G9.62+0.19 are in general higher than those found toward G31, in particular  $\text{CH}_3\text{CHO}$  in both sources and  $\text{C}_2\text{H}_5\text{CN}$  in MM8 which show a very high abundance w.r.t. methanol, similar to the values found toward the GC.

Overall, it seems that there is not a unique template for the abundances of COMs in HMCs. This could be the result of the peculiar physical properties (and their evolution with time) of each source, together with different environmental conditions that can affect the chemistry. In fact, the thermal history of each source has an impact on the reactions that can occur and their efficiency, likely leading to different values of abundance (Caselli et al. 1993; Viti & Williams 1999; Viti et al. 2004; Suzuki et al. 2018). As example, in the chemical models by Garrod et al. (2022) the abundances of N-bearing molecules are more sensitive to the time evolution of the warm-up phase (see Sect. 4.5), while the O-bearing species are more representative of the low-temperature dust-grain chemistry. Thus the different thermal evolution with time of each source can lead to different abundances w.r.t.  $\text{H}_2$  of N-bearing and O-bearing species, and also of the abundances w.r.t. methanol. Moreover, other environmental factors, such as the cosmic-ray ionization rate and the different

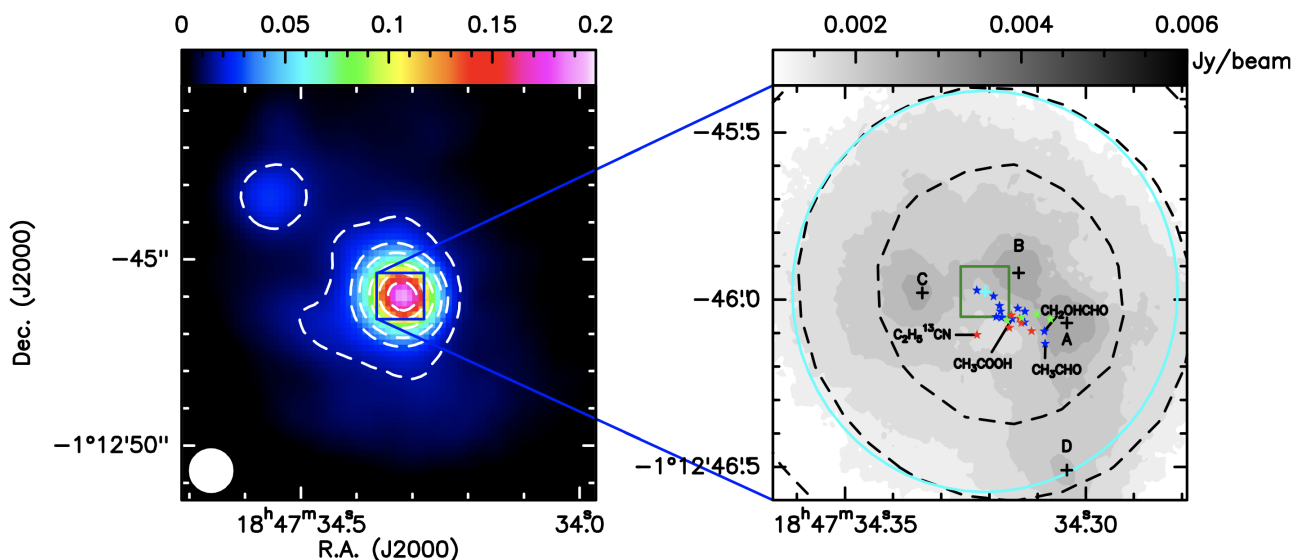


**Fig. 3.** Left panel: continuum map from Mininni et al. (2020). The beam of  $1''.2$  of the GUAPOS data is given in the lower-left corner. Contour levels are at 20, 40, 60, 100, 150, and 200 times the value of  $\text{rms} = 0.8 \text{ mJy beam}^{-1}$ . Right panel: zoom in of the left panel, where the black dashed contours are the two inner (150 and 200 times the rms) contours of the continuum image from the GUAPOS data at a resolution of  $1''.2$ , while the gray-levels (0.08, 0.12, 0.2, 0.4  $\text{mJy/beam}$ ) map is the continuum map at 3.5 mm from Beltrán et al. (2021) with an angular resolution of  $\sim 0''.075$ . The dimension of the beam is given in the lower-left corner, while the  $1''.2$  beam of the GUAPOS data is depicted by the cyan circular contour. The four black crosses marks the position of the four compact sources detected by Beltrán et al. (2021) and the green square indicates the dimension of the pixel in the GUAPOS maps and cubes, centered around the position of the peak of the GUAPOS continuum, indicated by the cyan cross. The blue stars indicate the positions of the peak of the emission of O-bearing species, red stars indicate the positions of the peak of the emission of N-bearing species, and green stars indicate the positions of the peak of the emission of O- and N-bearing species. The errors of the positions of the peak of molecular species are comparable to or below the dimension of the stars-shaped markers.

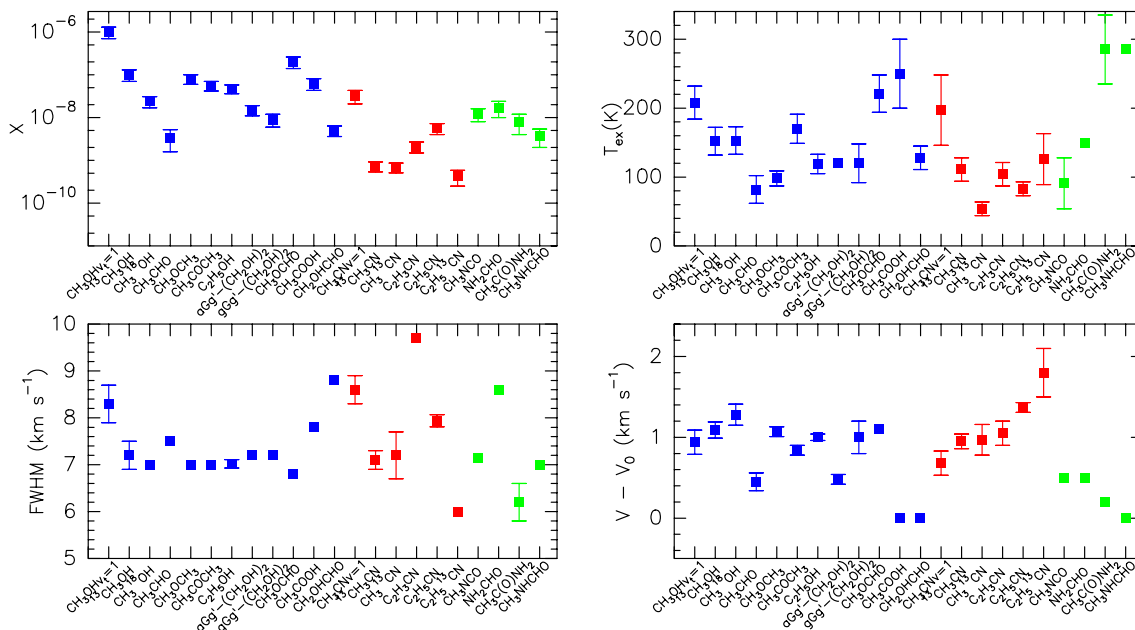


**Fig. 4.** Plots of abundance,  $X$ , excitation temperature,  $T_{\text{ex}}$ , full width at half maximum, FWHM, and line velocity,  $V - V_0$ . In blue the O-bearing species, in red the N-bearing species, while in green the O- and N-bearing species.

N/O elemental abundance in each particular region, have an impact on the chemistry.

In the case of hot corinos, the range of abundances w.r.t. methanol of the COMs is similar to the range of abundances found toward G31 and other HMCs. However, among the five sources (IRAS 16293–2422 A and B, NGC 1333 IRAS 4A2,

B1-c and S68N) only S68N shows an overall agreement with the majority of the COMs abundances estimated in G31, with the exception of  $\text{NH}_2\text{CHO}$  which is one order of magnitude less abundant. In IRAS 16203–22422 B, we have couples of COMs which show inverted abundances compared with G31. Those are  $\text{CH}_3\text{CHO}$  and  $\text{CH}_3\text{COCH}_3$  together with the two isomers

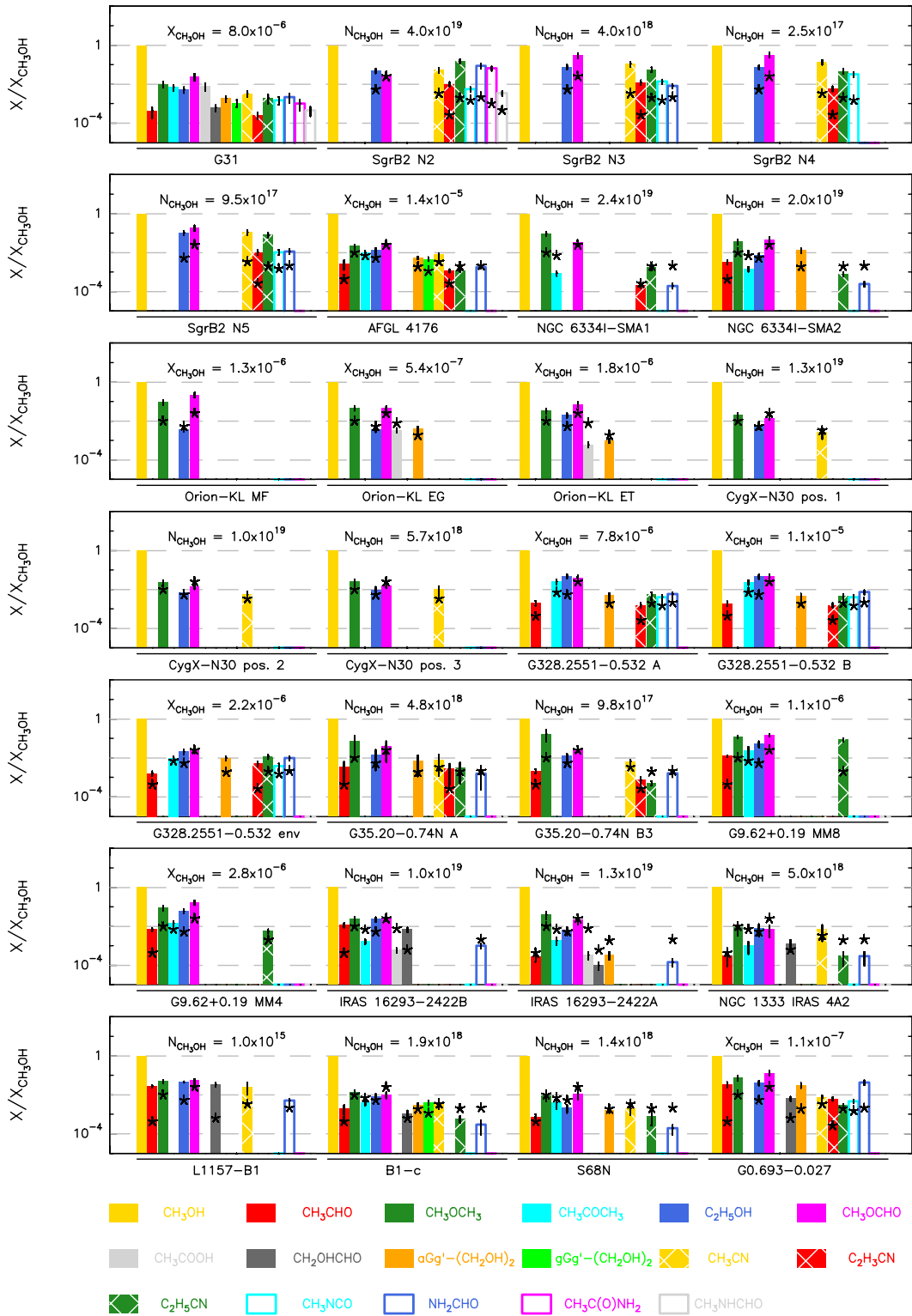


**Fig. 5.** Histograms of O-bearing, N-bearing, and O- and N-bearing COMs abundances with respect to methanol for G31 (this paper, Mininni et al. 2020, and Colzi et al. 2021), SgrB2-N2 (Belloche et al. 2016), SgrB2-N3/N4/N5 (Bonfand et al. 2019), AFGL4176 (Bøgelund et al. 2019), NGC 6334I-SMA1 and SMA2 (from SMA data analysis, Zernickel et al. 2012), Orion-KL methyl formate peak (MF), ethylene glycol peak (EG), and ethanol peak (ET) (Tercero et al. 2018), CygX-N30 at the position 1, 2, and 3 as described in van der Walt et al. (2021), G328.2551-0.532 A, B and inner-envelope position (Csengeri et al. 2019), G35.20-0.74N A and B3 (Allen et al. 2017), IRAS 16293-2422 A and B (Jørgensen et al. 2018; Coutens et al. 2016; Lykke et al. 2017; Manigand et al. 2020), NGC 1333 IRAS 4A2 (López-Sepulcre et al. 2017; Taquet et al. 2019), L1157-B1 (Lefloch et al. 2017), B1-c (van Gelder et al. 2020; Nazari et al. 2021), S68N (van Gelder et al. 2020; Nazari et al. 2021), and G+0.693-0.027 (Requena-Torres et al. 2006, 2008; Zeng et al. 2018; Bizzocchi et al. 2020; Rodríguez-Almeida et al. 2021; Rivilla et al. 2022; Sanz-Novo et al. 2022). For the sources for which the abundances were not available we have plotted the ratio of column densities, since  $X/X_{\text{CH}_3\text{OH}} = N/N_{\text{CH}_3\text{OH}}$ . In the upper part of each panel are reported the absolute values of  $X_{\text{CH}_3\text{OH}}$  (or  $N_{\text{CH}_3\text{OH}}$  in  $\text{cm}^{-2}$ , if the abundance is not available) for each source. To better compare the different sources with G31, we marked with asterisks the values of  $X/X_{\text{CH}_3\text{OH}}$  in G31 above the histogram of all the other sources.

CH<sub>3</sub>COOH and CH<sub>2</sub>OHCHO. In IRAS 16203–22422 A, quite all the COMs show lower abundances w.r.t. methanol than in G31, except for CH<sub>3</sub>OCH<sub>3</sub>, while for B1-c only half of the abundances are similar to those found towards G31.

The accretion-shock regions G328.2551–0.532 A and B display slightly higher abundances of quite all the COMs presented in Fig. 5 for comparison. This is also true for the shock position driven by a low-mass protostar, L1157-B1, where we have steeper increases of abundance for CH<sub>3</sub>CHO and CH<sub>2</sub>OCHO. The abundances in the envelope around a HMC precursor in G328-2551–0.532 also show, in general, higher values. Lastly, we compare the abundances found in G31 with those toward G+0.693–0.027, a giant molecular cloud located inside the CMZ. The abundances of CH<sub>3</sub>CHO, CH<sub>2</sub>OHCHO, aGg'-(CH<sub>2</sub>OH)<sub>2</sub>, C<sub>2</sub>H<sub>3</sub>CN, and NH<sub>2</sub>CHO w.r.t. CH<sub>3</sub>OH are a factor  $\sim 10$  or more higher than the abundances in G31, while the discrepancies with the other species are less pronounced. However, the value of column densities of CH<sub>3</sub>OH is 3 orders of magnitude lower than in G31. The presence of these complex molecules in this source is thought to be the result of sputtering of dust grains and their icy mantles (e.g. Requena-Torres et al. 2006, 2008), together with the action of high cosmic-ray fluxes that enhances the efficiency of ion-neutral reactions increasing the abundances of some molecular species, since this source is located in the GC.

From these comparisons, the chemical content of G31 in COMs is not comparable to that of sources in the GC due to the peculiar conditions found in those regions, and among other HMCs outside the central region of the galaxy we have a spread in chemical abundances among the sources. The only source with a remarkable similarity in chemical composition with G31, over the large number of molecules presented in this discussion, is AFGL4176. It is likely that the differences seen with respect to the other HMCs are due to different thermal histories of the various sources. Moreover, abundances w.r.t. methanol in hot corinos are mildly lower than those found in G31 as general trend, with the exception of IRAS 16293–2422 B, which however, does not show overall similar ratios. On the other hand, the abundances w.r.t. methanol found toward shocked regions, both in high-mass and low-mass star-forming regions show higher abundances than those of HMCs located outside the GC, like G31.

#### 4.5. Comparison with chemical models

In this section we compare the abundances of COMs in G31 with the results of the final models presented by Garrod et al. (2022). The work by Garrod et al. (2022) is one of the most comprehensive models of gas-grain chemistry up to date and predicts the abundances of several molecular species in HMCs and hot corinos, including a large number of COMs. In particular, nondiffusive reaction mechanism (Eley-Rideal mechanism, three-body reactions, three-body excited-formation reactions, and photodissociation-induced reaction mechanism) are implemented and the chemical network is updated with new routes proposed in recent years for the formation/destruction of dimethyl ether, formaldehyde, glycolaldehyde and ethylene glycol (e.g. Balucani et al. 2015; Ayouz et al. 2019).

The model has two physical phases: the first phase is the cold, free-fall collapse phase in which the gas temperature is fixed to 10 K, while density increases up to  $2 \times 10^8 \text{ cm}^{-3}$  (consistent with the rough estimate given for G31 of  $\sim 10^8 \text{ cm}^{-3}$  by Mininni et al. 2018). The second phase is the warm-up phase, where the density is constant and the temperature increases up to 200 K in with three different timescales for the three different models (*slow* timescale  $5 \times 10^4 \text{ yr}$ , *medium* timescale  $2 \times 10^5 \text{ yr}$ , and *fast*

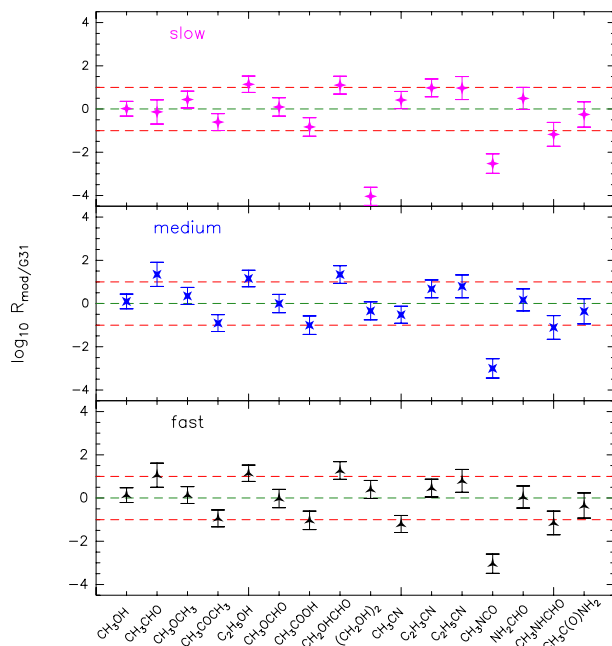


**Fig. 6.** Ratio of abundances from model by Garrod et al. (2022) and abundances derived for G31. The three panels use the abundances of the three different warm-up timescale chemical models. We considered an error of 30% on the values of abundances from chemical models. The green dashed line represent a ratio  $R_{\text{mod}/\text{G31}} = 1$ , while the two red dashed lines represent  $R_{\text{mod}/\text{G31}} = 0.1$  and 10.

timescale  $1 \times 10^6 \text{ yr}$ ). All the three models then continue until a temperature of 400 K is reached.

In Fig. 6 we plot the ratio between the peak abundances reached in the three final models (*slow* in the upper panel, *medium* in the middle panel, and *fast* in the lower panel) and the abundance derived in G31 for the COMs presented in this work. We assumed an error of 30% on the values derived from the chemical models. The agreement between the models and the abundances in G31 is remarkable, with only a few molecular species overabundant or underabundant in G31 by more than a factor 10 w.r.t. to the abundances derived by Garrod et al. (2022). The best overall agreement is with the *slow* model with a few exceptions, but the values from the *medium* model are also very close to those of G31. A large difference between these two models is seen in (CH<sub>2</sub>OH)<sub>2</sub>, for which the value found in G31 is in very good agreement ( $R_{\text{mod}/\text{G31}} \sim 1$ ) with the prediction of the *medium* model, while it is  $10^4$  times overabundant if compared with the *slow* model. In fact, in the latter model the destruction pathway of (CH<sub>2</sub>OH)<sub>2</sub> on the dust grains via H abstraction has more time to act, leading to the low value presented in Fig. 6. This might indicate that the best match with G31 could be with an intermediate timescale between the *slow* and the *medium* values. The only species that is not well reproduced by any of the models is CH<sub>3</sub>NCO, which is at least a factor 500 more abundant in G31. This species is underproduced by the models also when compared with SgrB2(N2) and IRAS 16293B; according to Garrod et al. (2022) this could be due to a not accurate estimate of

some activation-energy barriers or to the presence of other pathways for its production not present in the chemical network.

Overall, the agreement of the absolute values of the abundances derived in G31 with those of the model *slow* and *medium* is noteworthy. A good agreement for high-mass star-forming regions was found also for SgrB2(N2) with the *slow* model. However, for some molecular species the agreement was between the trend seen in the model and in the source among different COMs, while a significant fraction of COMs have absolute values that do not match well with the model predictions (Garrod et al. 2022), unlike the case of G31.

## 5. Conclusions

With the aim of characterizing the emission of the chemically rich HMC G31, and of understanding if chemical differentiation is present in this source, we have analyzed nine O-bearing and six N-bearing COMs using the data of the GUAPOS survey (Mininni et al. 2020; Colzi et al. 2021). In fact, Beltrán et al. (2021) highlighted the presence of four sources (labeled as A, B, C, and D) when observing this region at high angular resolution, which makes G31 an ideal laboratory to test whether different sources embedded in the same core show different chemistry. The analysis has been performed using the SLIM tool within the MADCUBA package. The molecular species analyzed include methanol, CH<sub>3</sub>OH, and its isotopologues <sup>13</sup>CH<sub>3</sub>OH and CH<sub>3</sub><sup>18</sup>OH, acetaldehyde, CH<sub>3</sub>CHO, dimethyl ether, CH<sub>3</sub>OCH<sub>3</sub>, acetone, CH<sub>3</sub>COCH<sub>3</sub>, ethanol, C<sub>2</sub>H<sub>5</sub>OH, methyl cyanide, CH<sub>3</sub>CN, and its isotopologues <sup>13</sup>CH<sub>3</sub>CN and CH<sub>3</sub><sup>13</sup>CN, vinyl cyanide, C<sub>2</sub>H<sub>3</sub>CN, and ethyl cyanide, C<sub>2</sub>H<sub>5</sub>CN, and its isotopologue, C<sub>2</sub>H<sub>5</sub><sup>13</sup>CN. Moreover, we have included in the analysis the three O-bearing isomers of C<sub>2</sub>H<sub>4</sub>O<sub>2</sub>, and the O- and N-bearing COMs CH<sub>3</sub>NCO, NH<sub>2</sub>CHO, CH<sub>2</sub>C(O)NH<sub>2</sub>, and CH<sub>3</sub>NHCHO, presented in previous work by Mininni et al. (2020) and Colzi et al. (2021).

The resolution of the maps is not sufficient to give conclusive results on the chemical segregation of molecules in G31. However, from the spectral analysis the most reliable parameter that can show hints of possible chemical differentiation is  $V-V_0$ . In G31 we have found that the values of  $V-V_0$  ( $V_0 = 96.5 \text{ km s}^{-1}$ ) are  $\sim 1.0 \text{ km s}^{-1}$  for the majority of the COMs analyzed in this and previous GUAPOS papers, with the exception of CH<sub>3</sub>CHO, CH<sub>3</sub>COOH, CH<sub>2</sub>OHCHO, and the four O- and N-bearing species CH<sub>3</sub>NCO, NH<sub>2</sub>CHO, CH<sub>3</sub>C(O)NH<sub>2</sub>, and CH<sub>3</sub>NHCHO. In particular, CH<sub>3</sub>COOH, CH<sub>2</sub>OHCHO, CH<sub>3</sub>C(O)NH<sub>2</sub>, and CH<sub>3</sub>NHCHO have  $V-V_0$  of  $\sim 0.2 - 0.0 \text{ km s}^{-1}$ , while for CH<sub>3</sub>CHO, aGg'-(CH<sub>2</sub>OH)<sub>2</sub>, CH<sub>3</sub>NCO, and NH<sub>2</sub>CHO the difference is less pronounced, with  $V-V_0 \sim 0.5 \text{ km s}^{-1}$ . Considering together the hints from spectral analysis and from map analysis, there are multiple indications of a possible chemical differentiation for the two O-bearing species CH<sub>3</sub>CHO and CH<sub>2</sub>OHCHO, with respect to the other O-bearing species. Other molecules show less pronounced differences in  $V-V_0$  and in shift of the position of the peak.

The values of abundances w.r.t. H<sub>2</sub> in G31 range from  $10^{-6}$  to  $10^{-10}$  for the different species. We have compared the abundances w.r.t. methanol of O-bearing, N-bearing, and O- and N-bearing COMs in G31 with other twenty-seven sources. These include other high-mass HMCs, hot corinos, shocked regions, the position of envelope gas around a HMC precursor, and molecular clouds. No clear trends among all the HMCs have been found. The sources SgrB2-N2/N3/N4/N5 show higher abundances, especially of N-bearing and O- and N-bearing species, when compared to the rest of the HMCs. The abun-

dances (w.r.t. methanol) found in G31 are in a good agreement with those found toward AFGL4176 (Bøgelund et al. 2019), and also the abundances of O-bearing species in G31 are in good agreement with those observed toward Orion-KL in the EG peak (Tercero et al. 2018). However, there is not a unique template for the abundances in HMCs. From the comparison with other types of sources we can see that as general trend hot corinos show mildly lower abundances w.r.t. methanol than those in G31, with the exception of the source IRAS 16293–2422 B, while in shocked regions the abundances w.r.t. methanol are enhanced, thanks to the sputtering of dust grains.

The abundances of COMs in G31 have been compared to the results of the three final chemical models of Garrod et al. (2022). The agreement is noteworthy, with most of the species in agreement within a factor ten with the estimate by the models. In particular, the *slow* model shows the best overall agreement, with the exception of (CH<sub>2</sub>OH)<sub>2</sub>, which is on the other hand well reproduced by the *medium* model. This might indicate that the best model to reproduce the abundances in G31 could have an intermediate timescale between the *slow* and the *medium* one, when (CH<sub>2</sub>OH)<sub>2</sub> is still not heavily destroyed.

## Acknowledgements

C. M. acknowledges funding from the European Research Council (ERC) under the European Union's Horizon 2020 program, through the ECOGAL Synergy grant (grant ID 855130). V.M.R. and L.C. have received funding from the Comunidad de Madrid through the Atracción de Talento Investigador (Doctores con experiencia) Grant (COOL: Cosmic Origins Of Life; 2019-T1/TIC-15379). L.C. has also received partial support from the Spanish State Research Agency (AEI; project number PID2019-105552RB-C41). A.S.M. acknowledges support from the RyC2021-032892-I grant funded by MCIN/AEI/10.13039/501100011033 and by the European Union 'Next GenerationEU'/PRTR, as well as the program Unidad de Excelencia María de Maeztu CEX2020-001058-M. This paper makes use of the following ALMA data: ADS/JAO.ALMA#2017.1.00501.S. ALMA is a partnership of ESO (representing its member states), NSF (USA) and NINS (Japan), together with NRC (Canada), MOST and ASIAA (Taiwan), and KASI (Republic of Korea), in cooperation with the Republic of Chile. The Joint ALMA Observatory is operated by ESO, AUI/NRAO and NAOJ.

## References

- Allen, V., van der Tak, F. F. S., Sánchez-Monge, Á., Cesaroni, R., & Beltrán, M. T. 2017, *A&A*, 603, A133
- Anderson, T., De Lucia, F., & Herbst, E. 1990, *ApJS*, 72, 797
- Ayouz, M. A., Yuen, C. H., Balucani, N., et al. 2019, *MNRAS*, 490, 1325
- Bally, J., Ginsburg, A., Arce, H., et al. 2017, *ApJ*, 837, 60
- Bally, J. & Zinnecker, H. 2005, *AJ*, 129, 2281
- Balucani, N., Ceccarelli, C., & Taquet, V. 2015, *MNRAS*, 449, L16
- Baskakov, O. I., Dyubko, S. F., Ilyushin, V. V., et al. 1996, *Journal of Molecular Spectroscopy*, 179, 94
- Bauer, A. & Godon, M. 1975, *Canadian Journal of Physics*, 53, 1154
- Belloche, A., Müller, H. S. P., Garrod, R. T., & Menten, K. M. 2016, *A&A*, 587, A91
- Belov, S. P., Winnewisser, G., & Herbst, E. 1995, *Journal of Molecular Spectroscopy*, 174, 253
- Beltrán, M. T., Cesaroni, R., Neri, R., et al. 2004, *ApJ*, 601, L187
- Beltrán, M. T., Cesaroni, R., Neri, R., et al. 2005, *A&A*, 435, 901
- Beltrán, M. T., Cesaroni, R., Rivilla, V. M., et al. 2018, *A&A*, 615, A141
- Beltrán, M. T., Codella, C., Viti, S., Neri, R., & Cesaroni, R. 2009, *ApJ*, 690, L93
- Beltrán, M. T., Rivilla, V. M., Cesaroni, R., et al. 2022a, *A&A*, 659, A81

- Beltrán, M. T., Rivilla, V. M., Cesaroni, R., et al. 2021, *A&A*, 648, A100
- Beltrán, M. T., Rivilla, V. M., Kumar, M. S. N., Cesaroni, R., & Galli, D. 2022b, *A&A*, 660, L4
- Bizzocchi, L., Prudenzeno, D., Rivilla, V. M., et al. 2020, *A&A*, 640, A98
- Blake, G. A., Sutton, E. C., Masson, C. R., & Phillips, T. G. 1987, *ApJ*, 315, 621
- Bøgelund, E. G., Barr, A. G., Taquet, V., et al. 2019, *A&A*, 628, A2
- Bonato, M., Liuzzo, E., Giannetti, A., et al. 2018, *MNRAS*, 478, 1512
- Bonfand, M., Belloche, A., Garrod, R. T., et al. 2019, *A&A*, 628, A27
- Boucher, D., Burie, J., Demaison, J., et al. 1977, *Journal of Molecular Spectroscopy*, 64, 290
- Boucher, D., Dubrulle, A., Demaison, J., & Dreizler, H. 1980, *Zeitschrift Naturforschung Teil A*, 35, 1136
- Briggs, D. S. 1995, in *American Astronomical Society Meeting Abstracts*, Vol. 187, American Astronomical Society Meeting Abstracts, 112.02
- Calcutt, H., Viti, S., Codella, C., et al. 2014, *MNRAS*, 443, 3157
- Caselli, P., Hasegawa, T. I., & Herbst, E. 1993, *ApJ*, 408, 548
- Cazzoli, G. & Kisiel, Z. 1988, *Journal of Molecular Spectroscopy*, 130, 303
- Cazzoli, G. & Puzzarini, C. 2006, *Journal of Molecular Spectroscopy*, 240, 153
- Cesaroni, R. 2019, *A&A*, 631, A65
- Cesaroni, R., Beltrán, M. T., Zhang, Q., Beuther, H., & Fallscheer, C. 2011, *A&A*, 533, A73
- Cesaroni, R., Hofner, P., Araya, E., & Kurtz, S. 2010, *A&A*, 509, A50
- Cesaroni, R., Olmi, L., Walmsley, C. M., Churchwell, E., & Hofner, P. 1994, *ApJ*, 435, L137
- Cesaroni, R., Sánchez-Monge, Á., Beltrán, M. T., et al. 2017, *A&A*, 602, A59
- Christen, D., Coudert, L. H., Larsson, J. A., & Cremer, D. 2001, *Journal of Molecular Spectroscopy*, 205, 185
- Christen, D., Coudert, L. H., Suenram, R. D., & Lovas, F. J. 1995, *Journal of Molecular Spectroscopy*, 172, 57
- Christen, D. & Müller, H. S. P. 2003, *Physical Chemistry Chemical Physics (Incorporating Faraday Transactions)*, 5, 3600
- Codella, C., Benedettini, M., Beltrán, M. T., et al. 2009, *A&A*, 507, L25
- Colmont, J. M., Włodarczak, G., Priem, D., et al. 1997, *Journal of Molecular Spectroscopy*, 181, 330
- Colzi, L., Rivilla, V. M., Beltrán, M. T., et al. 2021, *A&A*, 653, A129
- Coutens, A., Jørgensen, J. K., van der Wiel, M. H. D., et al. 2016, *A&A*, 590, L6
- Crockett, N. R., Bergin, E. A., Neill, J. L., et al. 2015, *ApJ*, 806, 239
- Csengeri, T., Belloche, A., Bontemps, S., et al. 2019, *A&A*, 632, A57
- Demaison, J., Cosleou, J., Bocquet, R., & Lesarri, A. G. 1994, *Journal of Molecular Spectroscopy*, 167, 400
- Demaison, J., Dubrulle, A., Boucher, D., Burie, J., & Typke, V. 1979, *Journal of Molecular Spectroscopy*, 76, 1
- Demyk, K., Mäder, H., Tercero, B., et al. 2007, *A&A*, 466, 255
- Durig, J. R., Deeb, H., Darkhalil, I. D., et al. 2011, *Journal of Molecular Structure*, 985, 202
- Endres, C. P., Drouin, B. J., Pearson, J. C., et al. 2009, *A&A*, 504, 635
- Feng, S., Beuther, H., Henning, T., et al. 2015, *A&A*, 581, A71
- Fisher, J., Paciga, G., Xu, L.-H., et al. 2007, *Journal of Molecular Spectroscopy*, 245, 7
- Fontani, F., Pascucci, I., Caselli, P., et al. 2007, *A&A*, 470, 639
- Friedel, D. N. & Snyder, L. E. 2008, *ApJ*, 672, 962
- Fukuyama, Y., Odashima, H., Takagi, K., & Tsunekawa, S. 1996, *ApJS*, 104, 329
- García de la Concepción, J., Colzi, L., Jiménez-Serra, I., et al. 2022, *A&A*, 658, A150
- Garrod, R. T. 2013, *ApJ*, 765, 60
- Garrod, R. T., Jin, M., Matis, K. A., et al. 2022, *ApJS*, 259, 1
- Gerry, M. C. L., Lees, R. M., & Winnewisser, G. 1976, *Journal of Molecular Spectroscopy*, 61, 231
- Gerry, M. C. L. & Winnewisser, G. 1973, *Journal of Molecular Spectroscopy*, 48, 1
- Girart, J. M., Beltrán, M. T., Zhang, Q., Rao, R., & Estalella, R. 2009, *Science*, 324, 1408
- Gorai, P., Das, A., Shimonishi, T., et al. 2021, *ApJ*, 907, 108
- Groner, P., Albert, S., Herbst, E., & De Lucia, F. C. 1998, *ApJ*, 500, 1059
- Groner, P., Albert, S., Herbst, E., et al. 2002, *ApJS*, 142, 145
- Herbst, E., Messer, J. K., De Lucia, F. C., & Helminger, P. 1984, *Journal of Molecular Spectroscopy*, 108, 42
- Herbst, E. & van Dishoeck, E. F. 2009, *ARA&A*, 47, 427
- Hoshino, Y., Ohishi, M., Akabane, K., et al. 1996, *ApJS*, 104, 317
- Hughes, R. H., Good, W. E., & Coles, D. K. 1951, *Physical Review*, 84, 418
- Ikedo, M., Duan, Y.-B., Tsunekawa, S., & Takagi, K. 1998, *ApJS*, 117, 249
- Immer, K., Li, J., Quiroga-Núñez, L. H., et al. 2019, *A&A*, 632, A123
- Isokoski, K., Bottinelli, S., & van Dishoeck, E. F. 2013, *A&A*, 554, A100
- Jiménez-Serra, I., Vasyunin, A. I., Caselli, P., et al. 2016, *ApJ*, 830, L6
- Jiménez-Serra, I., Zhang, Q., Viti, S., Martín-Pintado, J., & de Wit, W. J. 2012, *ApJ*, 753, 34
- Johnson, D. R., Lovas, F. J., Gottlieb, C. A., et al. 1977, *ApJ*, 218, 370
- Jørgensen, J. K., Müller, H. S. P., Calcutt, H., et al. 2018, *A&A*, 620, A170
- Jørgensen, J. K., van der Wiel, M. H. D., Coutens, A., et al. 2016, *A&A*, 595, A117
- Kalenskii, S. V. & Johansson, L. E. B. 2010, *Astronomy Reports*, 54, 1084
- Kleiner, I., Lovas, F. J., & Godefroid, M. 1996, *Journal of Physical and Chemical Reference Data*, 25, 1113
- Kukulich, S. G. 1982, *J. Chem. Phys.*, 76, 97
- Kukulich, S. G., Ruben, D. J., Wang, J. H. S., & Williams, J. R. 1973, *J. Chem. Phys.*, 58, 3155
- Lees, R. M. & Baker, J. G. 1968, *J. Chem. Phys.*, 48, 5299
- Lefloch, B., Ceccarelli, C., Codella, C., et al. 2017, *MNRAS*, 469, L73
- López-Sepulcre, A., Sakai, N., Neri, R., et al. 2017, *A&A*, 606, A121
- Lovas, F. J., Lutz, H., & Dreizler, H. 1979, *Journal of Physical and Chemical Reference Data*, 8, 1051
- Lykke, J. M., Coutens, A., Jørgensen, J. K., et al. 2017, *A&A*, 597, A53
- Mäder, H., Heise, H. M., & Dreizler, H. 1974, *Zeitschrift Naturforschung Teil A*, 29, 164
- Manigand, S., Jørgensen, J. K., Calcutt, H., et al. 2020, *A&A*, 635, A48
- Martín, S., Martín-Pintado, J., Blanco-Sánchez, C., et al. 2019, *A&A*, 631, A159
- Martín, S., Requena-Torres, M. A., Martín-Pintado, J., & Mauersberger, R. 2008, *ApJ*, 678, 245
- Matsushima, F., Evenson, K. M., & Zink, L. R. 1994, *Journal of Molecular Spectroscopy*, 164, 517
- Mayen-Gijón, J. M., Anglada, G., Osorio, M., et al. 2014, *MNRAS*, 437, 3766
- McMullin, J. P., Waters, B., Schiebel, D., Young, W., & Golap, K. 2007, *Astronomical Society of the Pacific Conference Series*, Vol. 376, *CASA Architecture and Applications*, ed. R. A. Shaw, F. Hill, & D. J. Bell, 127
- Mininni, C., Beltrán, M. T., Rivilla, V. M., et al. 2020, *A&A*, 644, A84
- Mininni, C., Fontani, F., Rivilla, V. M., et al. 2018, *MNRAS*, 476, L39
- Müller, H. S. P., Belloche, A., Menten, K. M., Comito, C., & Schilke, P. 2008, *Journal of Molecular Spectroscopy*, 251, 319
- Müller, H. S. P., Belloche, A., Xu, L.-H., et al. 2016, *A&A*, 587, A92
- Müller, H. S. P., Brown, L. R., Drouin, B. J., et al. 2015, *Journal of Molecular Spectroscopy*, 312, 22
- Müller, H. S. P. & Christen, D. 2004, *Journal of Molecular Spectroscopy*, 228, 298
- Müller, H. S. P., Drouin, B. J., & Pearson, J. C. 2009, *A&A*, 506, 1487
- Müller, H. S. P., Menten, K. M., & Mäder, H. 2004, *A&A*, 428, 1019
- Müller, H. S. P., Schlöder, F., Stutzki, J., & Winnewisser, G. 2005, *Journal of Molecular Structure*, 742, 215
- Müller, H. S. P., Thorwirth, S., Roth, D. A., & Winnewisser, G. 2001, *A&A*, 370, L49
- Nazari, P., van Gelder, M. L., van Dishoeck, E. F., et al. 2021, *A&A*, 650, A150
- Neustock, W., Guarnieri, A., Demaison, J., & Włodarczak, G. 1990, *Zeitschrift Naturforschung Teil A*, 45, 702
- Odashima, H., Matsushima, F., Nagai, K., Tsunekawa, S., & Takagi, K. 1995, *Journal of Molecular Spectroscopy*, 173, 404
- Oldag, F. & Sutter, D. H. 1992, *Zeitschrift Naturforschung Teil A*, 47, 527
- Osorio, M., Anglada, G., Lizano, S., & D'Alessio, P. 2009, *ApJ*, 694, 29
- Paganí, L., Bergin, E., Goldsmith, P. F., et al. 2019, *A&A*, 624, L5
- Palau, A., Fuente, A., Girart, J. M., et al. 2011, *ApJ*, 743, L32
- Pearson, J. C., Brauer, C. S., & Drouin, B. J. 2008, *Journal of Molecular Spectroscopy*, 251, 394
- Pearson, J. C. & Mueller, H. S. P. 1996, *ApJ*, 471, 1067
- Pearson, J. C., Sastry, K. V. L. N., Herbst, E., & De Lucia, F. C. 1994, *ApJS*, 93, 589
- Pearson, J. C., Sastry, K. V. L. N., Winnewisser, M., Herbst, E., & De Lucia, F. C. 1995, *Journal of Physical and Chemical Reference Data*, 24, 1
- Peng, T. C., Despois, D., Brouillet, N., et al. 2013, *A&A*, 554, A78
- Peng, Y., Liu, T., Qin, S.-L., et al. 2022, *MNRAS*, 512, 4419
- Peter, R. & Dreizler, H. 1965, *Zeitschrift Naturforschung Teil A*, 20, 301
- Pickett, H. M., Cohen, E. A., Brinza, D. E., & Schaefer, M. M. 1981, *Journal of Molecular Spectroscopy*, 89, 542
- Pickett, H. M., Poynter, R. L., Cohen, E. A., et al. 1998, *J. Quant. Spectr. Rad. Transf.*, 60, 883
- Predoi-Cross, A., Lees, R. M., Lichau, H., Winnewisser, M., & Drummond, J. R. 1997, *International Journal of Infrared and Millimeter Waves*, 18, 2047
- Qin, S.-L., Liu, T., Liu, X., et al. 2022, *MNRAS*, 511, 3463
- Remijan, A., Shiao, Y. S., Friedel, D. N., Meier, D. S., & Snyder, L. E. 2004, *ApJ*, 617, 384
- Requena-Torres, M. A., Martín-Pintado, J., Martín, S., & Morris, M. R. 2008, *ApJ*, 672, 352
- Requena-Torres, M. A., Martín-Pintado, J., Rodríguez-Franco, A., et al. 2006, *A&A*, 455, 971
- Richard, C., Margulès, L., Motiyenko, R. A., & Guillemin, J. C. 2012, *A&A*, 543, A135
- Rivilla, V. M., Beltrán, M. T., Cesaroni, R., et al. 2017, *A&A*, 598, A59
- Rivilla, V. M., Colzi, L., Jiménez-Serra, I., et al. 2022, *ApJ*, 929, L11
- Rodríguez-Almeida, L. F., Jiménez-Serra, I., Rivilla, V. M., et al. 2021, *ApJ*, 912, L11
- Sánchez-Monge, Á., Schilke, P., Ginsburg, A., Cesaroni, R., & Schmiedeke, A. 2018, *A&A*, 609, A101
- Sanz-Novo, M., Belloche, A., Rivilla, V. M., et al. 2022, *A&A*, 666, A114



- Sastry, K. V. L. N., Lees, R. M., & De Lucia, F. C. 1984, *Journal of Molecular Spectroscopy*, 103, 486
- Sipilä, O., Silsbee, K., & Caselli, P. 2021, *ApJ*, 922, 126
- Stolze, M. & Sutter, D. H. 1985, *Zeitschrift Naturforschung Teil A*, 40, 998
- Suzuki, T., Majumdar, L., Ohishi, M., et al. 2018, *ApJ*, 863, 51
- Taquet, V., Bianchi, E., Codella, C., et al. 2019, *A&A*, 632, A19
- Tercero, B., Cuadrado, S., López, A., et al. 2018, *A&A*, 620, L6
- Vacherand, J. M., Van Eijck, B. P., Burie, J., & Demaison, J. 1986, *Journal of Molecular Spectroscopy*, 118, 355
- van der Walt, S. J., Kristensen, L. E., Jørgensen, J. K., et al. 2021, *A&A*, 655, A86
- van Gelder, M. L., Tabone, B., Tychoniec, Ł., et al. 2020, *A&A*, 639, A87
- Viti, S., Collings, M. P., Dever, J. W., McCoustra, M. R. S., & Williams, D. A. 2004, *MNRAS*, 354, 1141
- Viti, S. & Williams, D. A. 1999, *MNRAS*, 305, 755
- Widicus Weaver, S. L. & Friedel, D. N. 2012, *ApJS*, 201, 16
- Widicus Weaver, S. L., Laas, J. C., Zou, L., et al. 2017, *ApJS*, 232, 3
- Wilson, T. L. & Rood, R. 1994, *ARA&A*, 32, 191
- Wyrowski, F., Schilke, P., Walmsley, C. M., & Menten, K. M. 1999, *ApJ*, 514, L43
- Xu, L.-H., Fisher, J., Lees, R. M., et al. 2008, *Journal of Molecular Spectroscopy*, 251, 305
- Xu, L.-H. & Lovas, F. J. 1997, *Journal of Physical and Chemical Reference Data*, 26, 17
- Yan, Y. T., Zhang, J. S., Henkel, C., et al. 2019, *ApJ*, 877, 154
- Zeng, S., Jiménez-Serra, I., Rivilla, V. M., et al. 2018, *MNRAS*, 478, 2962
- Zernickel, A., Schilke, P., Schmiedeke, A., et al. 2012, *A&A*, 546, A87

## Appendix A: Catalog entries documentation for the molecular species analyzed

### Appendix A.1: Methanol $\text{CH}_3\text{OH}$ , $^{13}\text{CH}_3\text{OH}$ , and $\text{CH}_3^{18}\text{OH}$

We have used the spectroscopy from the CDMS catalog. The entry of  $\text{CH}_3\text{OH}$  is based mainly on the work of Xu et al. (2008), with additional data from Lees & Baker (1968), Pickett et al. (1981), Sastry et al. (1984), Herbst et al. (1984), Anderson et al. (1990), Matsushima et al. (1994), Odashima et al. (1995), Belov et al. (1995), and Müller et al. (2004). More information is available at:

<https://cdms.astro.uni-koeln.de/cgi-bin/cdmsinfo?file=e032504.cat>

The entry of  $^{13}\text{CH}_3\text{OH}$  is based on the review work by Xu & Lovas (1997). More information available at:

<https://cdms.astro.uni-koeln.de/cgi-bin/cdmsinfo?file=e033502.cat>

The entry of  $\text{CH}_3^{18}\text{OH}$  is based on the work by Fisher et al. (2007) with the inclusion of other transitions from Hughes et al. (1951), Gerry et al. (1976), Hoshino et al. (1996), Predoi-Cross et al. (1997), and Ikeda et al. (1998). More information available at:

<https://cdms.astro.uni-koeln.de/cgi-bin/cdmsinfo?file=e034504.cat>

### Appendix A.2: Acetaldehyde $\text{CH}_3\text{CHO}$

We have used the spectroscopy from the JPL catalog. The entry is based on the work of Kleiner et al. (1996) and reference therein. More information is available at:

<https://spec.jpl.nasa.gov/ftp/pub/catalog/doc/d044003.pdf>

### Appendix A.3: Dimethyl ether $\text{CH}_3\text{OCH}_3$

We have used the spectroscopy from the CDMS catalog. The entry of  $\text{CH}_3\text{OCH}_3$  is based mainly on the work of Endres et al. (2009), Lovas et al. (1979), Neustock et al. (1990), and Groner et al. (1998). More information is available at:

<https://cdms.astro.uni-koeln.de/cgi-bin/cdmsinfo?file=e046514.cat>

### Appendix A.4: Acetone $\text{CH}_3\text{COCH}_3$

We have used the spectroscopy from the JPL catalog. The entry is based on the works of Peter & Dreizler (1965), Vacherand et al. (1986), Oldag & Sutter (1992), and Groner et al. (2002). More information is available at:

<https://spec.jpl.nasa.gov/ftp/pub/catalog/doc/d058003.pdf>

### Appendix A.5: Ethanol $\text{C}_2\text{H}_5\text{OH}$

We have used the spectroscopy from the CDMS catalog. The entry of  $\text{C}_2\text{H}_5\text{OH}$  is based mainly on the work of Pearson et al. (1995); Pearson & Mueller (1996); Pearson et al. (2008). More information is available at:

<https://cdms.astro.uni-koeln.de/cgi-bin/cdmsinfo?file=e046524.cat>

### Appendix A.6: Ethylene glycol $\text{aGg}^-(\text{CH}_2\text{OH})_2$ and $\text{gGg}^-(\text{CH}_2\text{OH})_2$

We have used the spectroscopy from the CDMS catalog. The entries of  $\text{aGg}^-(\text{CH}_2\text{OH})_2$  is based on the works by Christen

et al. (1995) and Christen & Müller (2003). More information is available at:

<https://cdms.astro.uni-koeln.de/cgi-bin/cdmsinfo?file=e062503.cat>

The entries of  $\text{gGg}^-(\text{CH}_2\text{OH})_2$  is based on the works by Christen et al. (2001) and Müller & Christen (2004). More information is available at:

<https://cdms.astro.uni-koeln.de/cgi-bin/cdmsinfo?file=e062504.cat>

### Appendix A.7: Methyl cyanide $\text{CH}_3\text{CN}$ , $^{13}\text{CH}_3\text{CN}$ , and $\text{CH}_3^{13}\text{CN}$

We have used the spectroscopy from the CDMS catalog. The entry of  $\text{CH}_3\text{CN}$  is mainly based on the works by Müller et al. (2015), Kukolich et al. (1973); Kukolich (1982), Boucher et al. (1977), Cazzoli & Puzzarini (2006), Bauer & Godon (1975). More information is available at:

<https://cdms.astro.uni-koeln.de/cgi-bin/cdmsinfo?file=e041505.cat>

The entry of  $^{13}\text{CH}_3\text{CN}$  is based on the works by Müller et al. (2009), Pearson & Mueller (1996), and Demaison et al. (1979). More information is available at:

<https://cdms.astro.uni-koeln.de/cgi-bin/cdmsinfo?file=e042508.cat>

The entry of  $\text{CH}_3^{13}\text{CN}$  is a combined CDMS and JPL entry and is based on the works by Müller et al. (2009), Pearson & Mueller (1996), Demaison et al. (1979), and Kukolich (1982). More information is available at:

<https://cdms.astro.uni-koeln.de/cgi-bin/cdmsinfo?file=e042509.cat>

### Appendix A.8: Vinyl cyanide $\text{C}_2\text{H}_3\text{CN}$

We have used the spectroscopy from the CDMS catalog. The entry of  $\text{C}_2\text{H}_3\text{CN}$  is based mainly on the works of Müller et al. (2008), Gerry & Winnewisser (1973), Stolze & Sutter (1985), Cazzoli & Kisiel (1988), Demaison et al. (1994), Baskakov et al. (1996), and Colmont et al. (1997). More information is available at:

<https://cdms.astro.uni-koeln.de/cgi-bin/cdmsinfo?file=e053515.cat>

### Appendix A.9: Ethyl cyanide $\text{C}_2\text{H}_5\text{CN}$ and $\text{C}_2\text{H}_5^{13}\text{CN}$

We have used the spectroscopy from the CDMS catalog. The entry of  $\text{C}_2\text{H}_5\text{CN}$  is based mainly on the works of Mäder et al. (1974), Johnson et al. (1977), Boucher et al. (1980), Pearson et al. (1994), and Fukuyama et al. (1996). More information is available at:

<https://cdms.astro.uni-koeln.de/cgi-bin/cdmsinfo?file=e055502.cat>

The entry of  $\text{C}_2\text{H}_5^{13}\text{CN}$  is based mainly on the works of Demyk et al. (2007) and Richard et al. (2012). More information is available at:

<https://cdms.astro.uni-koeln.de/cgi-bin/cdmsinfo?file=e056504.cat>

## Appendix B: Spectra

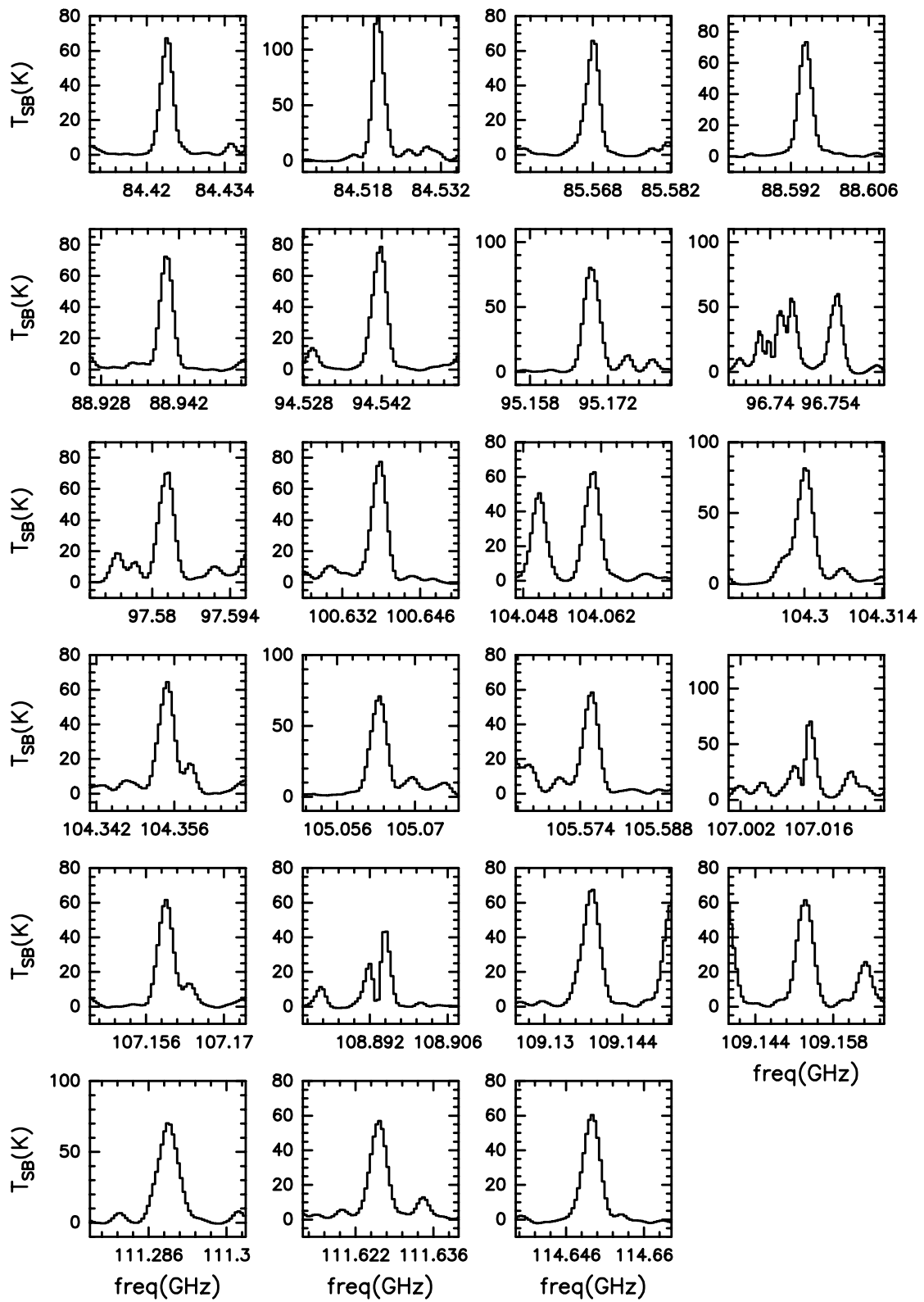


**Fig. B.1.** Observed spectrum of some of the brightest transitions of  $\text{CH}_3\text{OH } v_t = 0$ .  $T_{\text{SB}}$  stands for synthesized beam temperature.

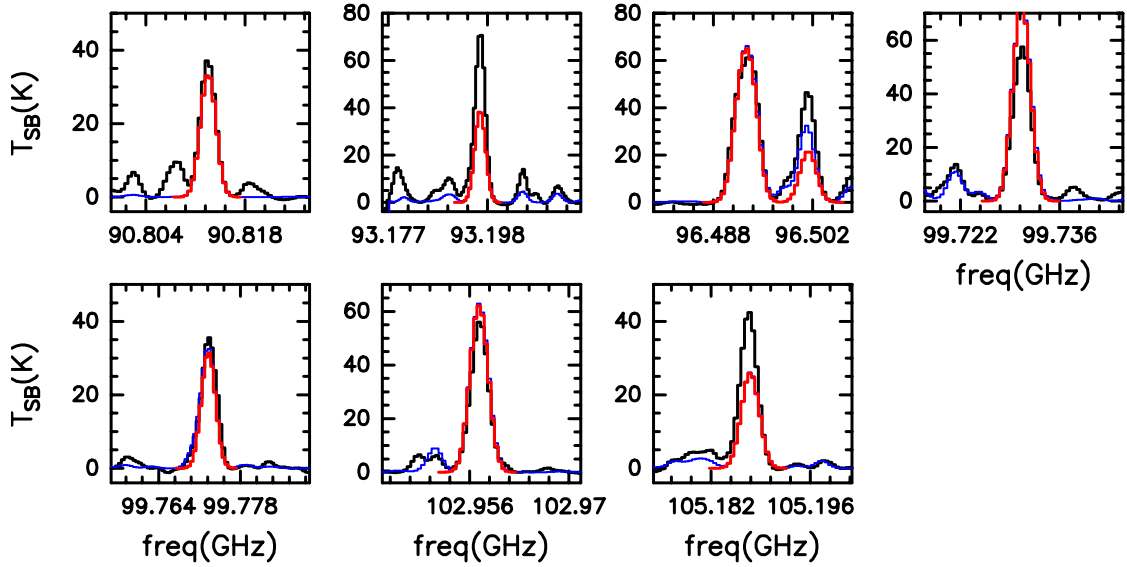


**Fig. B.2.** Transitions used to constrain the fit of  $\text{CH}_3\text{OH } v_t = 1$ . In black the observed spectrum, in red the synthetic spectrum of the best fit for  $\text{CH}_3\text{OH } v_t = 1$  only, while in blue the spectrum that takes into account all the species identified in the spectrum, including those published in Mininni et al. (2020); Colzi et al. (2021).  $T_{\text{SB}}$  stands for synthesized beam temperature.

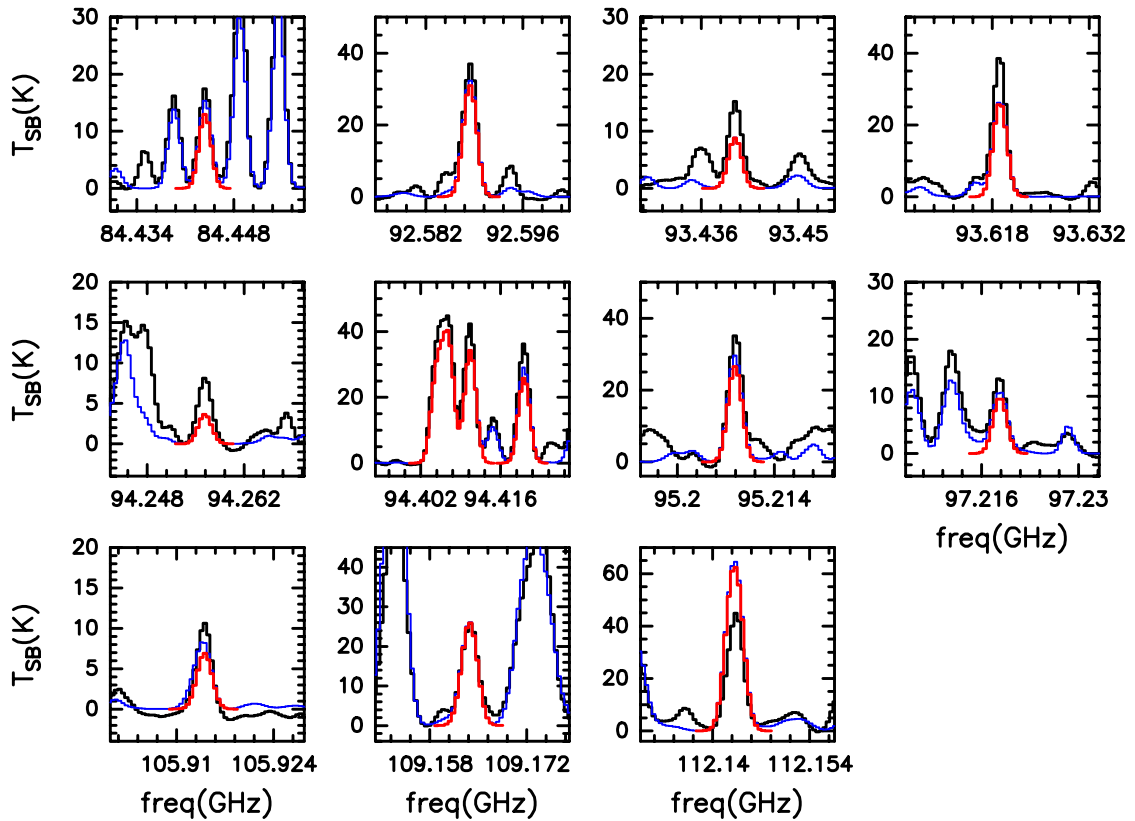


**Fig. B.3.** Transitions used to constrain the fit of  $^{13}\text{CH}_3\text{OH}$ . In black the observed spectrum, in red the synthetic spectrum of the best fit for  $^{13}\text{CH}_3\text{OH}$  only, while in blue the spectrum that takes into account all the species identified in the spectrum, including those published in Mininni et al. (2020); Colzi et al. (2021).  $T_{\text{SB}}$  stands for synthesized beam temperature.

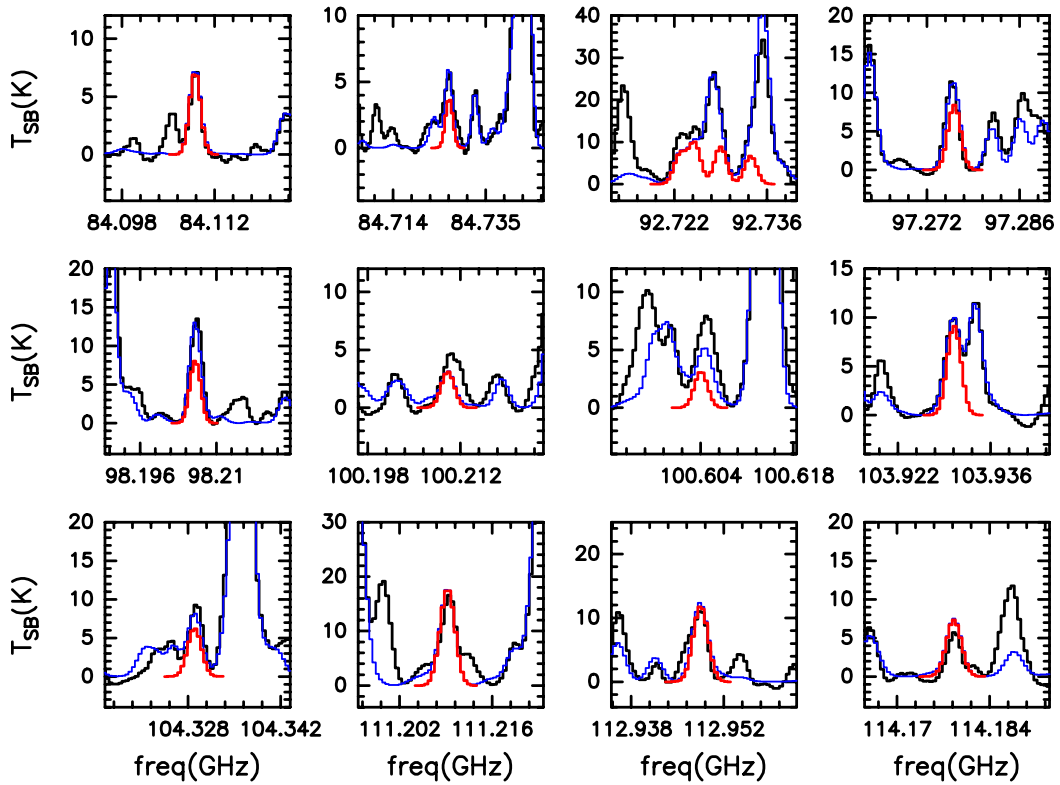


**Fig. B.4.** Transitions used to constrain the fit of  $\text{CH}_3^{18}\text{OH}$ . In black the observed spectrum, in red the synthetic spectrum of the best fit for  $\text{CH}_3^{18}\text{OH}$  only, while in blue the spectrum that takes into account all the species identified in the spectrum, including those published in Mininni et al. (2020); Colzi et al. (2021).  $T_{\text{SB}}$  stands for synthesized beam temperature.

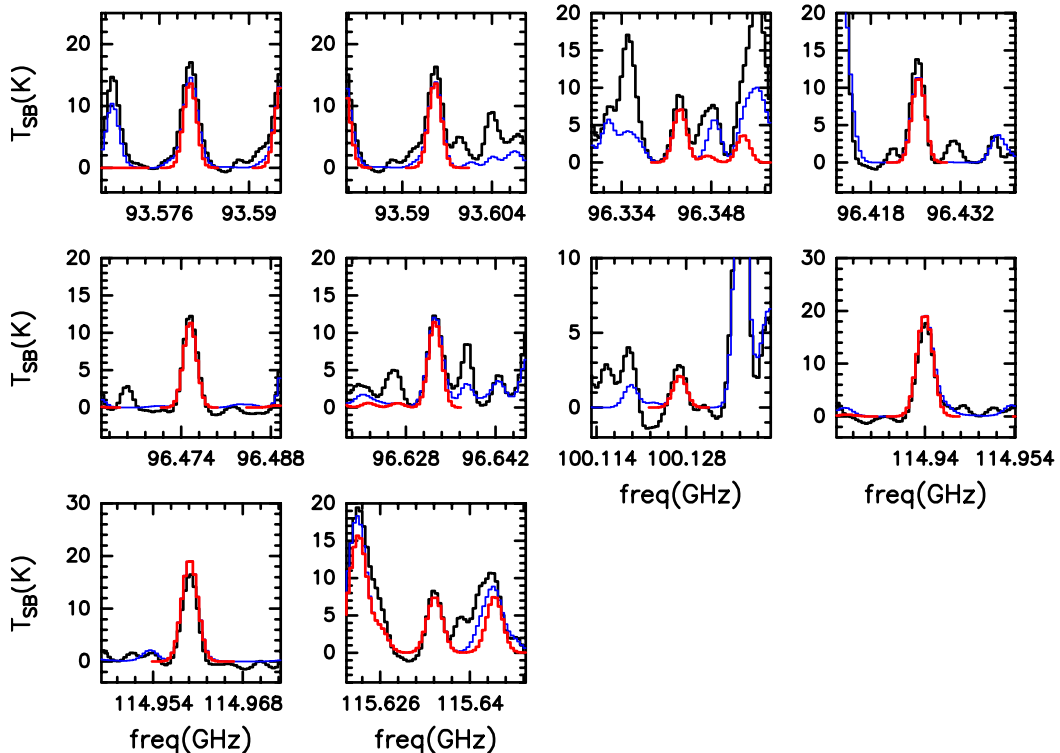


**Fig. B.5.** Transitions used to constrain the fit of  $\text{CH}_3\text{CHO}$ . In black the observed spectrum, in red the synthetic spectrum of the best fit for  $\text{CH}_3\text{CHO}$  only, while in blue the spectrum that takes into account all the species identified in the spectrum, including those published in Mininni et al. (2020); Colzi et al. (2021).  $T_{\text{SB}}$  stands for synthesized beam temperature.

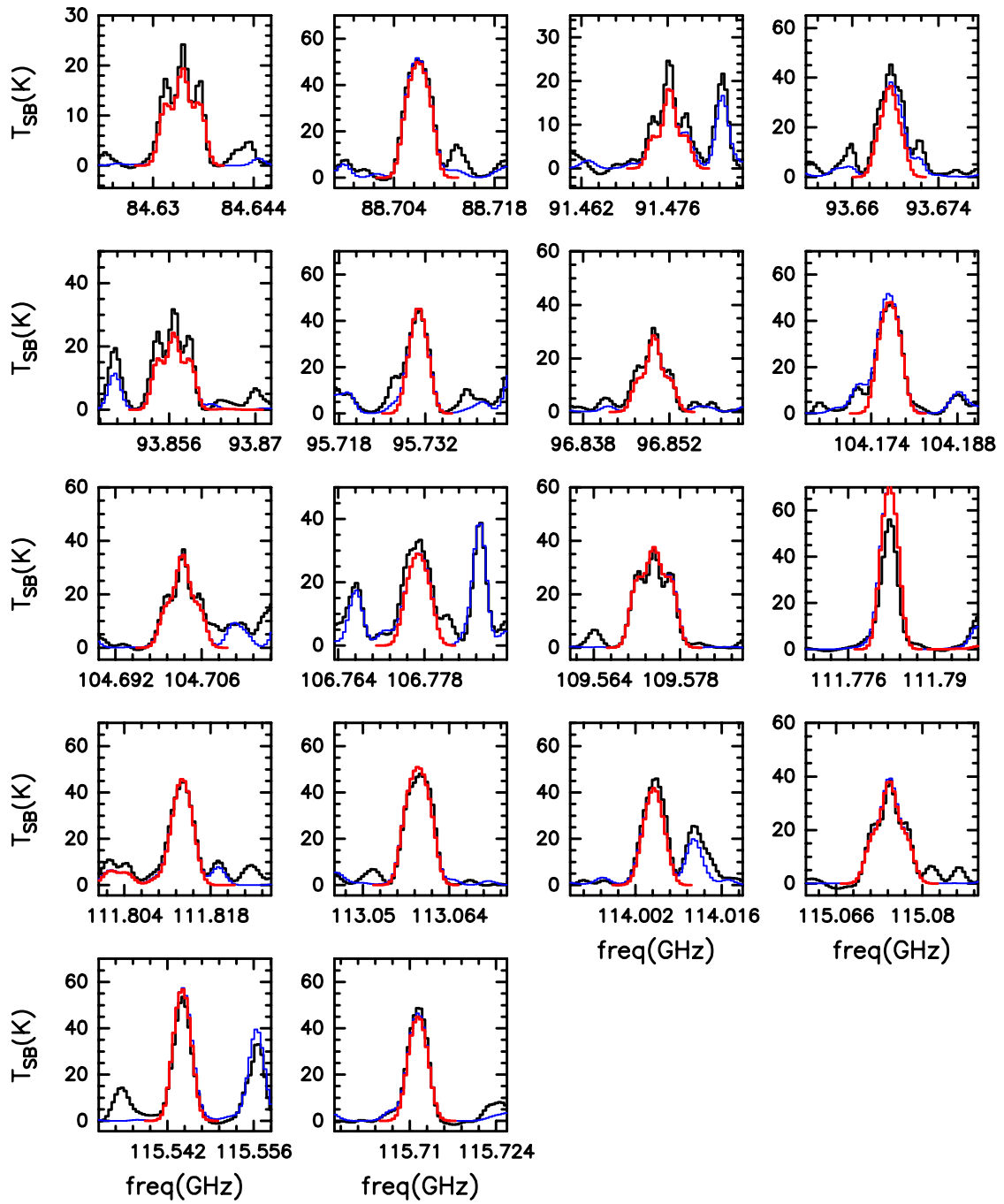


**Fig. B.6.** Transitions used to constrain the fit of  $\text{CH}_3\text{OCH}_3$ . In black the observed spectrum, in red the synthetic spectrum of the best fit for  $\text{CH}_3\text{OCH}_3$  only, while in blue the spectrum that takes into account all the species identified in the spectrum, including those published in Mininni et al. (2020); Colzi et al. (2021).  $T_{SB}$  stands for synthesized beam temperature.

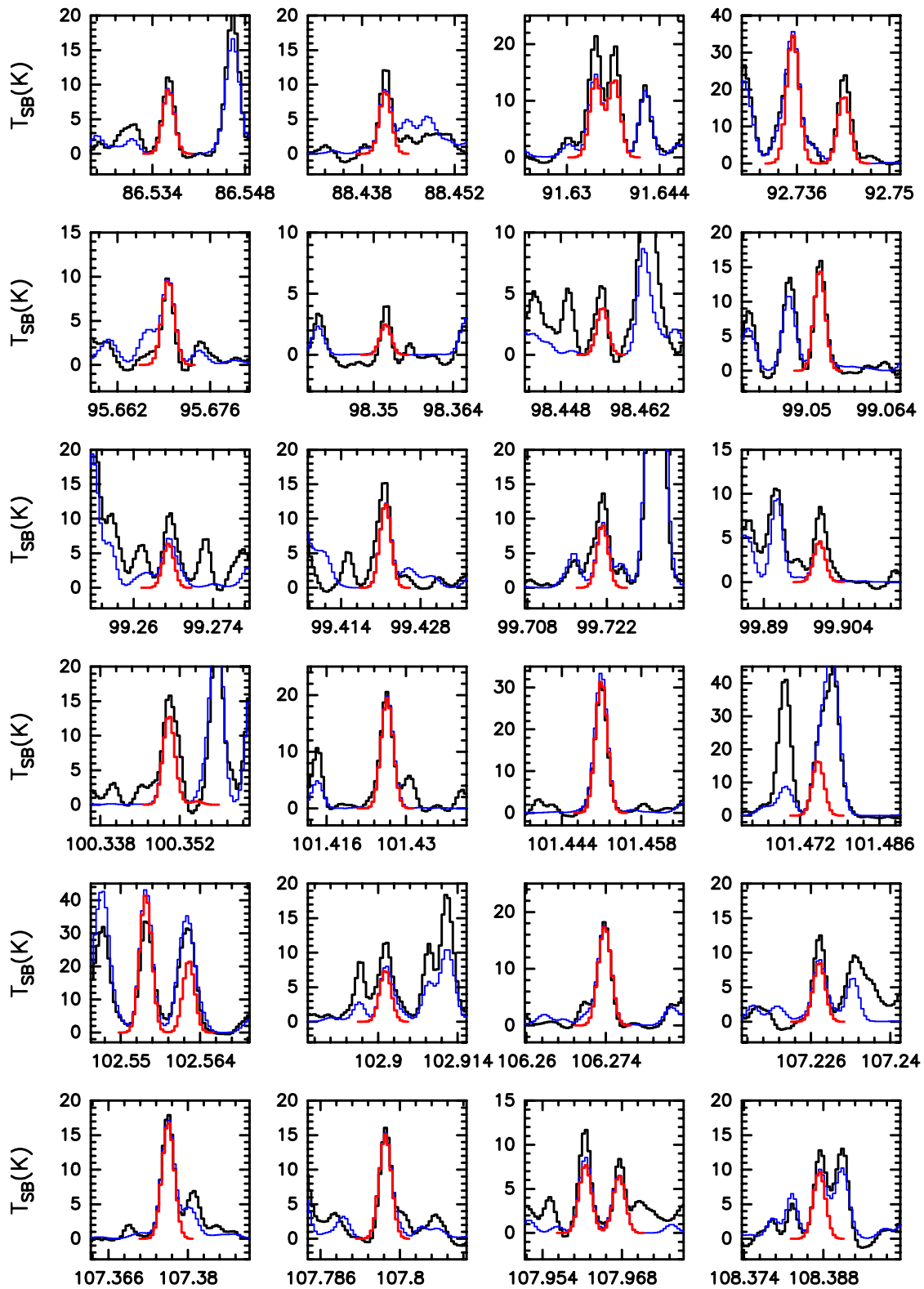


**Fig. B.7.** Transitions used to constrain the fit of  $\text{CH}_3\text{COCH}_3$ . In black the observed spectrum, in red the synthetic spectrum of the best fit for  $\text{CH}_3\text{COCH}_3$  only, while in blue the spectrum that takes into account all the species identified in the spectrum, including those published in Mininni et al. (2020); Colzi et al. (2021).  $T_{SB}$  stands for synthesized beam temperature.

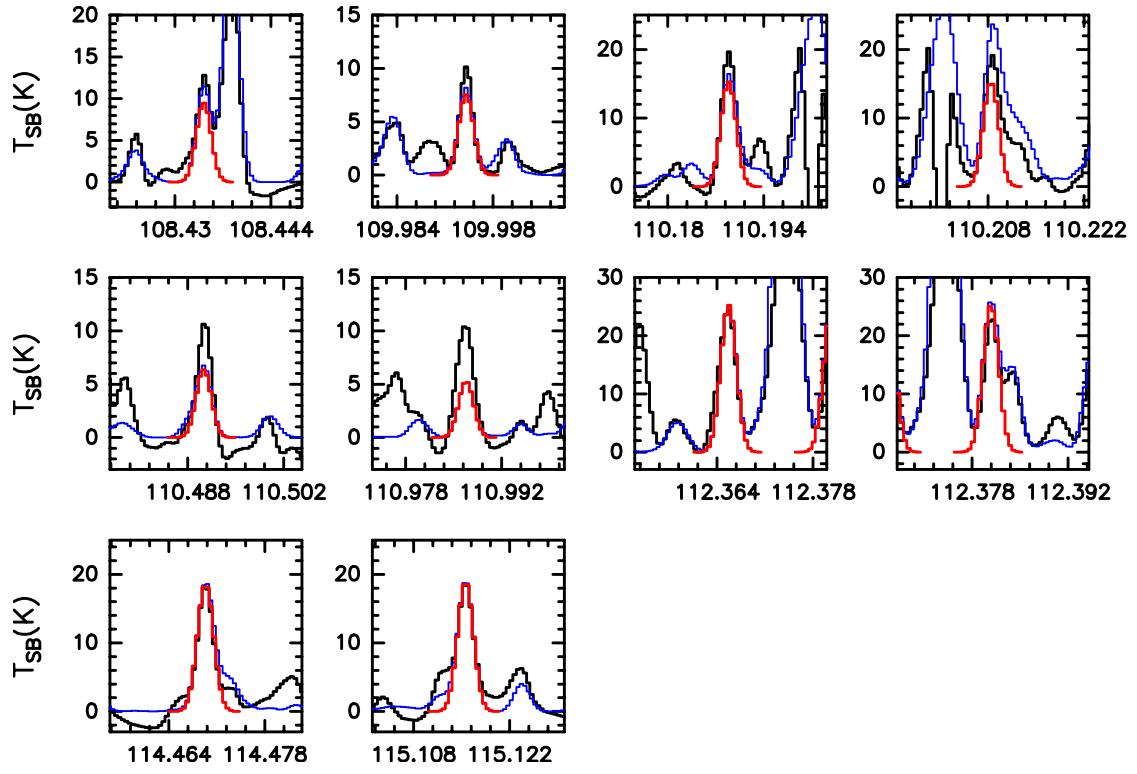
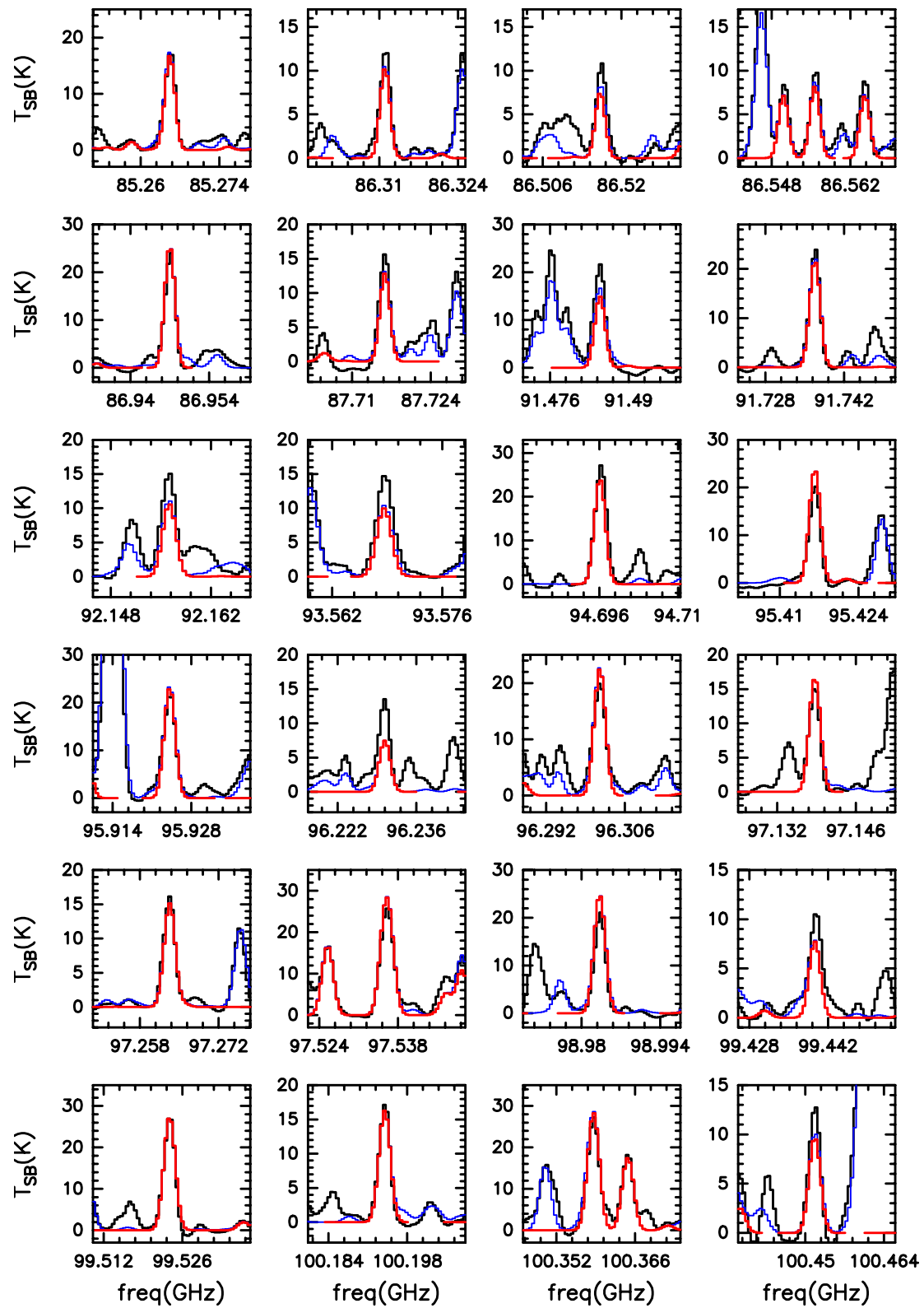


Fig. B.8. Continue





**Fig. B.9.** Transitions used to constrain the fit of  $C_2H_5OH$ . In black the observed spectrum, in red the synthetic spectrum of the best fit for  $C_2H_5OH$  only, while in blue the spectrum that takes into account all the species identified in the spectrum, including those published in Mininni et al. (2020); Colzi et al. (2021).  $T_{SB}$  stands for synthesized beam temperature.

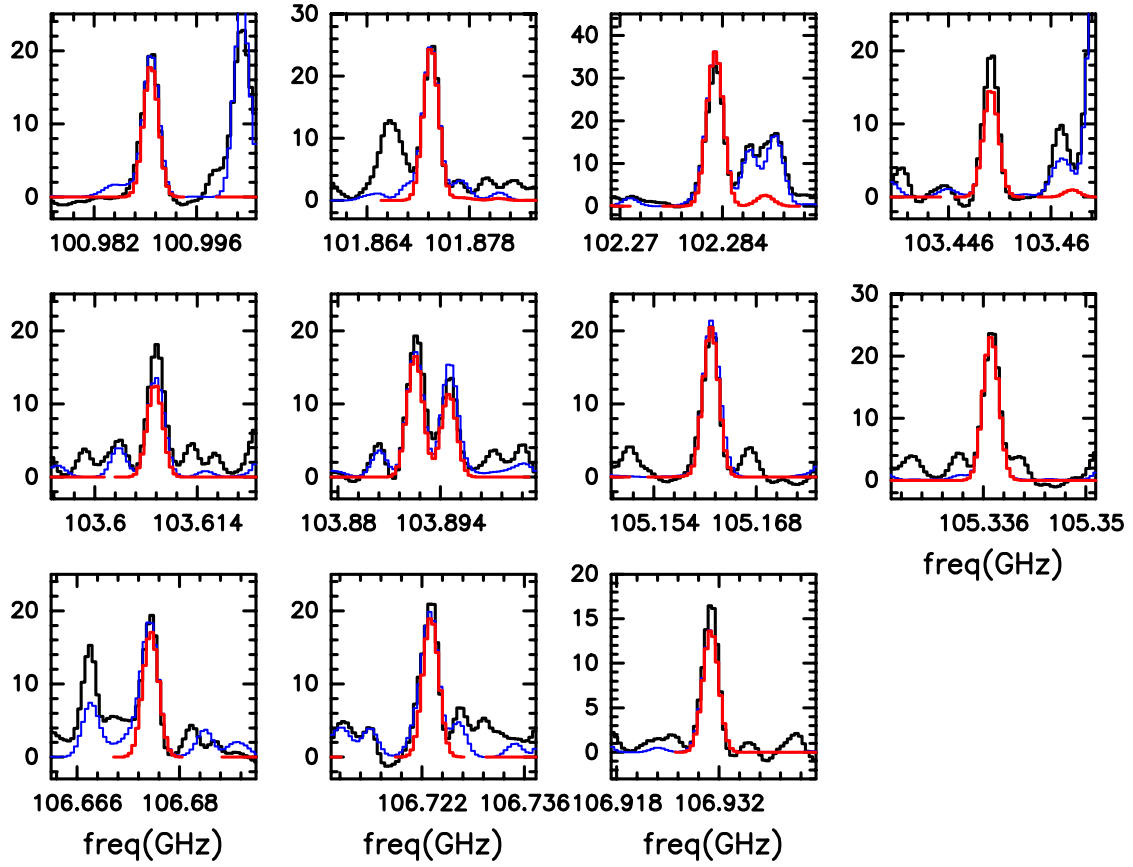
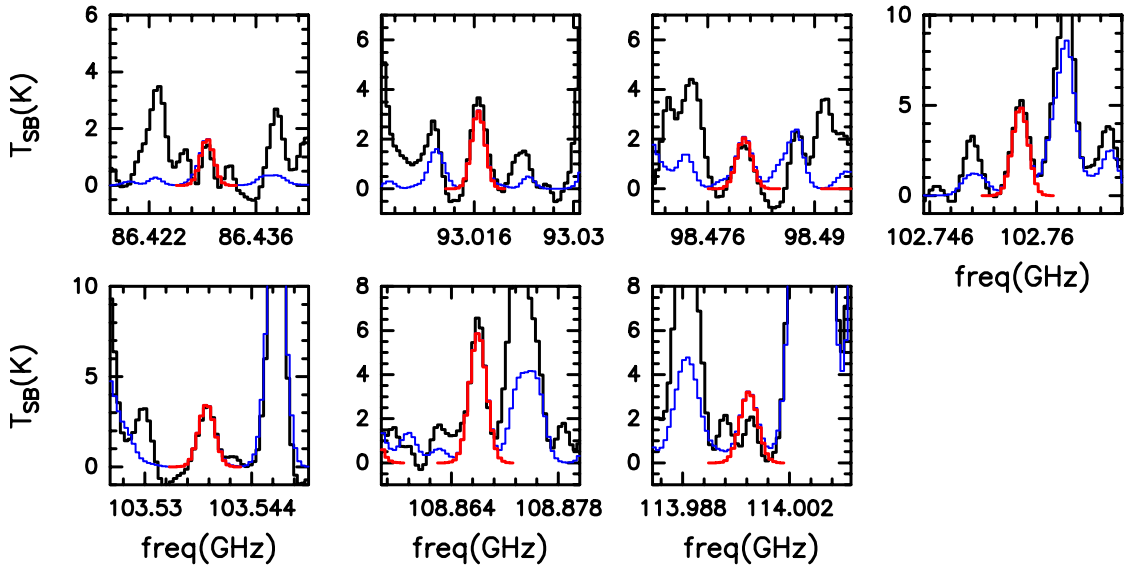
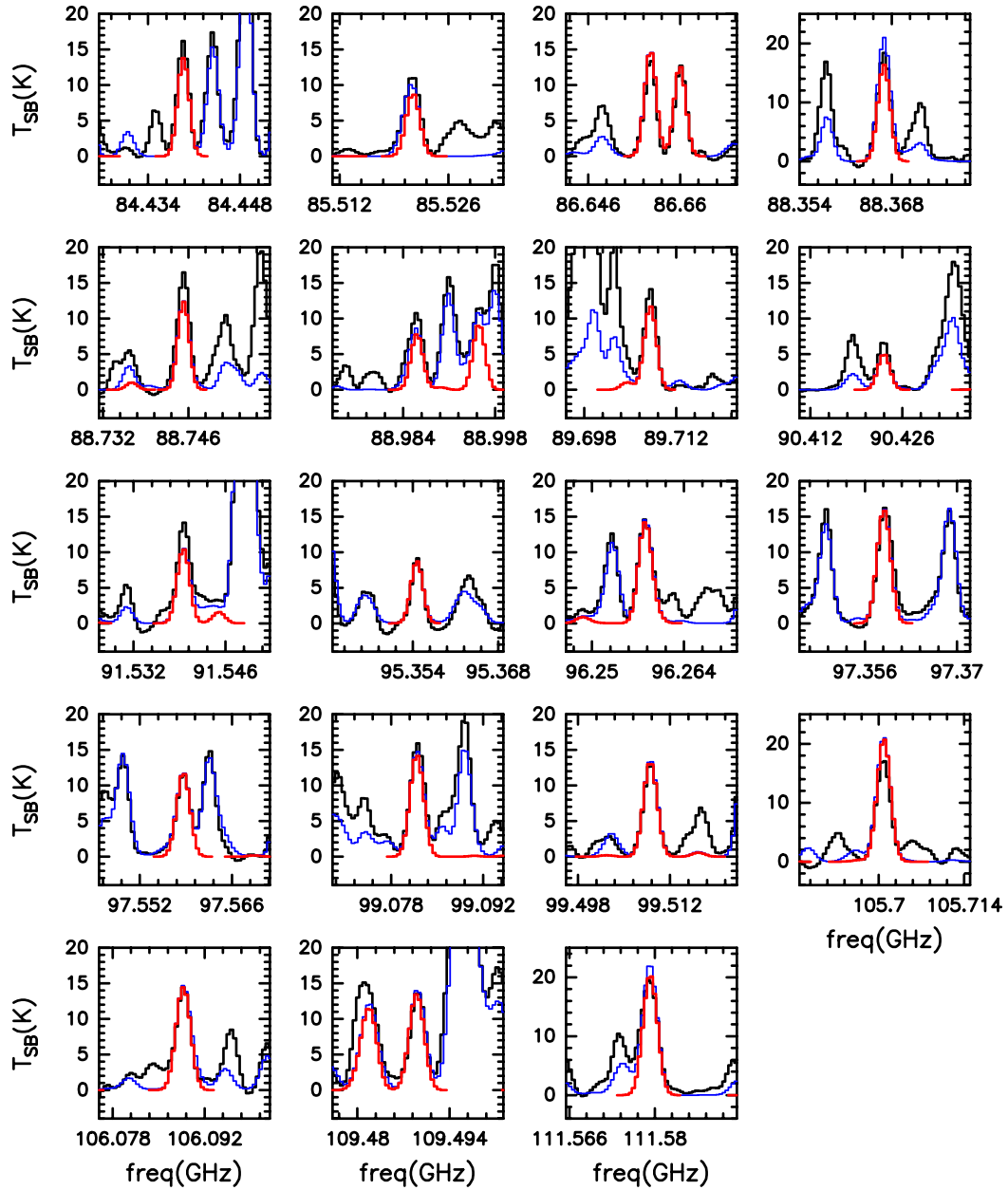


Fig. B.10. Continue



**Fig. B.11.** Transitions used to constrain the fit of  $gGg'-(CH_2OH)_2$ . In black the observed spectrum, in red the synthetic spectrum of the best fit for  $gGg'-(CH_2OH)_2$  only, while in blue the spectrum that takes into account all the species identified in the spectrum, including those published in Mininni et al. (2020); Colzi et al. (2021).  $T_{SB}$  stands for synthesized beam temperature.



**Fig. B.12.** Transitions used to constrain the fit of  $aGg'-(CH_2OH)_2$ . In black the observed spectrum, in red the synthetic spectrum of the best fit for  $aGg'-(CH_2OH)_2$  only, while in blue the spectrum that takes into account all the species identified in the spectrum, including those published in Mininni et al. (2020); Colzi et al. (2021).  $T_{SB}$  stands for synthesized beam temperature.

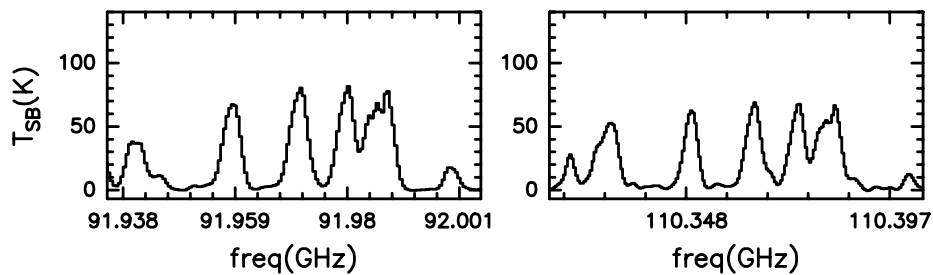


**Fig. B.13.** Observed spectrum of  $CH_3CN$   $v=0$ .  $T_{SB}$  stands for synthesized beam temperature.

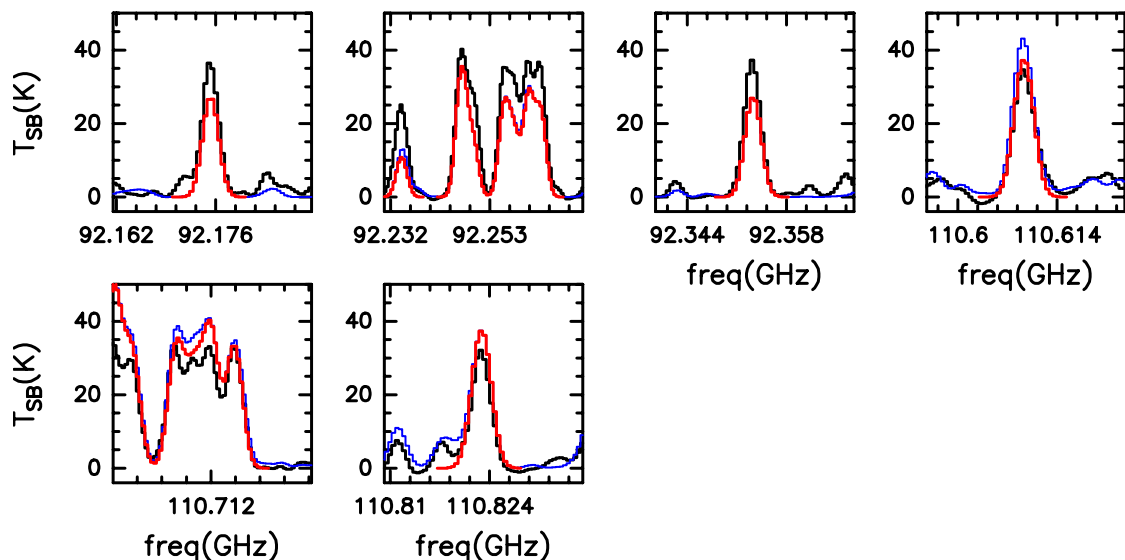


**Fig. B.14.** Transitions used to constrain the fit of  $\text{CH}_3\text{CN } v_8 = 1$ . In black the observed spectrum, in red the synthetic spectrum of the best fit for  $\text{CH}_3\text{CN } v_8 = 1$  only, while in blue the spectrum that takes into account all the species identified in the spectrum, including those published in Mininni et al. (2020); Colzi et al. (2021).  $T_{\text{SB}}$  stands for synthesized beam temperature.

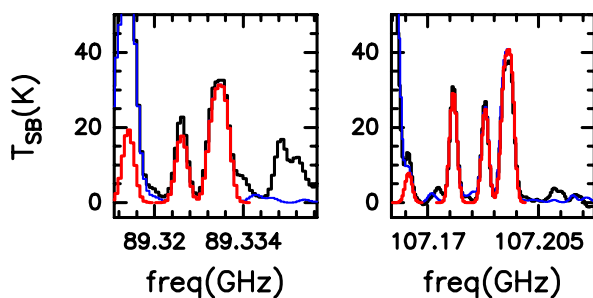


**Fig. B.15.** Transitions used to constrain the fit of  $^{13}\text{CH}_3\text{CN}$ . In black the observed spectrum, in red the synthetic spectrum of the best fit for  $^{13}\text{CH}_3\text{CN}$  only, while in blue the spectrum that takes into account all the species identified in the spectrum, including those published in Mininni et al. (2020); Colzi et al. (2021).  $T_{\text{SB}}$  stands for synthesized beam temperature.

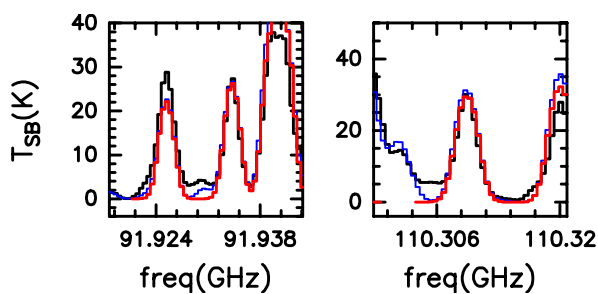


**Fig. B.16.** Transitions used to constrain the fit of  $\text{CH}_3^{13}\text{CN}$ . In black the observed spectrum, in red the synthetic spectrum of the best fit for  $\text{CH}_3^{13}\text{CN}$  only, while in blue the spectrum that takes into account all the species identified in the spectrum, including those published in Mininni et al. (2020); Colzi et al. (2021).  $T_{\text{SB}}$  stands for synthesized beam temperature.

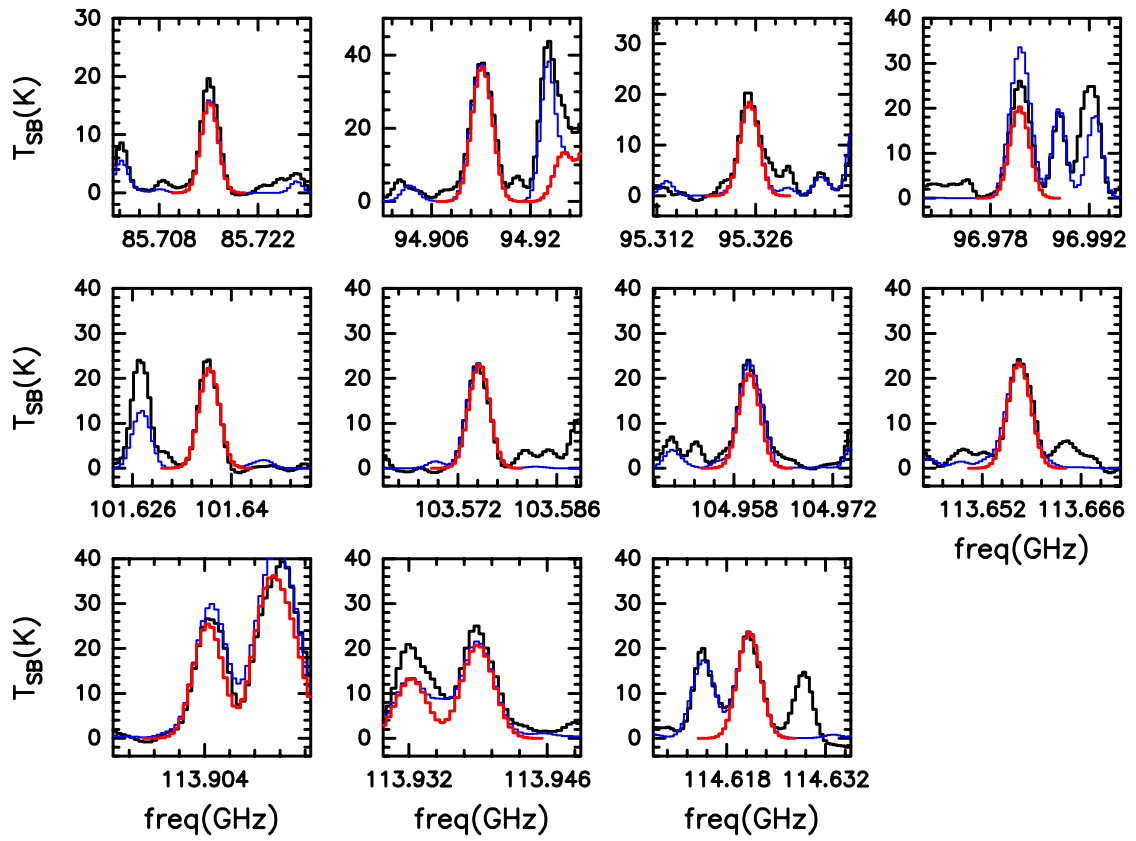


**Fig. B.17.** Transitions used to constrain the fit of  $C_2H_3CN$ . In black the observed spectrum, in red the synthetic spectrum of the best fit for  $C_2H_3CN$  only, while in blue the spectrum that takes into account all the species identified in the spectrum, including those published in Mininni et al. (2020); Colzi et al. (2021).  $T_{SB}$  stands for synthesized beam temperature.

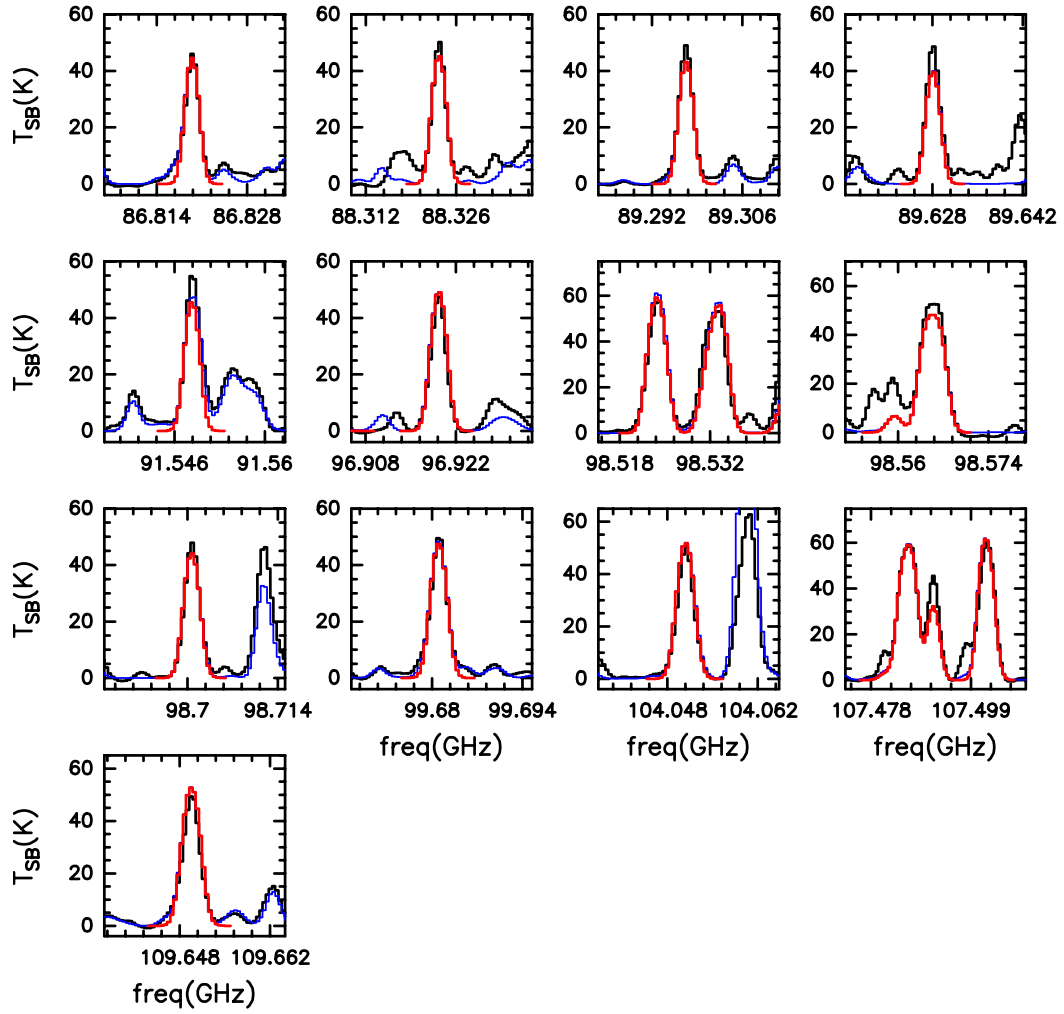


**Fig. B.18.** Transitions used to constrain the fit of  $C_2H_5CN$ . In black the observed spectrum, in red the synthetic spectrum of the best fit for  $C_2H_5CN$  only, while in blue the spectrum that takes into account all the species identified in the spectrum, including those published in Mininni et al. (2020); Colzi et al. (2021).  $T_{SB}$  stands for synthesized beam temperature.

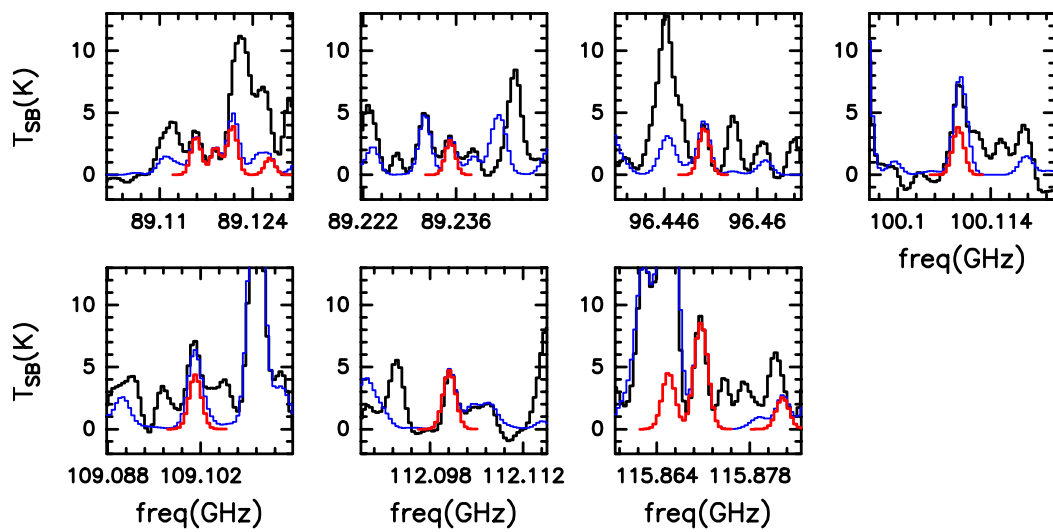


**Fig. B.19.** Transitions used to constrain the fit of  $C_2H_5^{13}CN$ . In black the observed spectrum, in red the synthetic spectrum of the best fit for  $C_2H_5^{13}CN$  only, while in blue the spectrum that takes into account all the species identified in the spectrum, including those published in Mininni et al. (2020); Colzi et al. (2021).  $T_{SB}$  stands for synthesized beam temperature.

## Appendix C: Selected transitions for the analysis

**Table C.1.** Most unblended transitions of CH<sub>3</sub>OH  $v_t = 1$  used to constrain the fit. Database used: CDMS

Frequency MHz	log(I)	$E_U/k_B$			$Q_U$			$Q_L$			$\tau_0$	
		K	J	$K_a$	$K_c$	J	$K_a$	$K_c$	J	$K_a$		
90813.078	-5.274	809.18	20	3	18	19	2	18	0.178	Y		
93196.672	-5.514	303.22	1	0	1	2	1	2	0.210	Y		
96492.163	-5.519	298.74	2	1	2	1	1	1	0.201	Y		
96493.551	-5.407	307.85	2	0	2	1	0	1	0.257	Y		
99730.940	-5.137	340.46	6	1	6	5	0	5	0.442	Y		
99772.834	-5.202	903.29	20	3	17	21	4	18	0.167	Y		
102957.672	-5.019	642.91	15	2	14	16	3	14	0.361	Y		
105187.877	-5.434	646.65	7	7	0	6	6	0	0.135	Y		

**Notes:** Frequency: rest frequency of the transitions in units MHz; log(I): logarithm of the line intensity;  $E_U/k_B$ : energy of the upper state of the transition in units K;  $Q_U$ : quantum numbers of the upper level;  $Q_L$ : quantum numbers of the lower level;  $\tau_0$ : optical depth at the center of the line, calculated with the parameters of best fit; flag indicating which transitions have been used to create the mean map.

**Table C.2.** Most unblended transitions of <sup>13</sup>CH<sub>3</sub>OH used to constrain the fit. Database used: CDMS

Frequency MHz	log(I)	$E_U/k_B$			$Q_U$			$Q_L$			$\tau_0$	
		K	J	$K_a$	$K_c$	J	$K_a$	$K_c$	J	$K_a$		
84444.140	-5.174	269.32	1	3	-3	1	2	-4	0.091	Y		
92588.704	-4.964	101.33	7	2		8	1		0.235	Y		
93441.190	-5.204	339.40	6	1		5	0		0.061	Y		
93619.460	-5.155	21.32	2	1		1	1		0.194	Y		
94256.648	-5.599	332.51	2	1		1	1		0.025			
94405.163	-5.135	12.41	2	-1		1	-1		0.207			
94407.129	-5.002	6.80	2	0		1	0		0.287			
94411.016	-5.021	19.93	2	0		1	0		0.263			
94420.449	-5.146	27.88	2	1		1	1		0.192	Y		
95208.660	-5.141	21.43	2	1		1	1		0.197	Y		
97219.021	-5.154	331.12	1	3	-5	1	4	-4	0.068			
105914.401	-5.413	232.53	1	3	-2	1	3	1	0.047	Y		
109164.120	-5.103	13.12	0	0		1	-1		0.193	Y		
112143.546	-4.614	28.06	3	1		4	0		0.553			

**Notes:** Frequency: rest frequency of the transitions in units MHz; log(I): logarithm of the line intensity;  $E_U/k_B$ : energy of the upper state of the transition in units K;  $Q_U$ : quantum numbers of the upper level;  $Q_L$ : quantum numbers of the lower level;  $\tau_0$ : optical depth at the center of the line, calculated with the parameters of best fit; flag indicating which transitions have been used to create the mean map.

**Table C.3.** Most unblended transitions of CH<sub>3</sub><sup>18</sup>OH used to constrain the fit. Database used: CDMS

Frequency MHz	log(I)	$E_U/k_B$			$Q_U$			$Q_L$			$\tau_0$	
		K	J	$K_a$	$K_c$	J	$K_a$	$K_c$	J	$K_a$		
84109.417	-5.000	144.29	11	1	11	10	2	9	0.048	Y		
84727.078	-5.179	217.58	11	4	7	12	3	10	0.025			
92723.286	-5.158	7.62	2	1	2	1	1	1	0.048			
92725.469	-5.026	2.16	2	0	2	1	0	1	0.066			
92729.399	-5.045	14.66	2	0	2	1	0	1	0.061			
92733.939	-5.163	22.35	2	1	1	1	1	0	0.045			
97276.539	-4.938	92.54	7	2	6	8	1	7	0.057	Y		
98206.527	-4.986	66.06	6	2	5	7	1	7	0.055			
100210.505	-5.011	338.39	16	3	14	15	4	11	0.021			

**Table C.3.** Continued.

Frequency MHz	log(I)	$E_U/k_B$		$Q_U$			$Q_L$			$\tau_0$
		K	J	$K_a$	$K_c$	J	$K_a$	$K_c$		
100604.491	-5.007	338.39	16	3	13	15	4	12	0.021	
103930.931	-4.747	179.31	12	1	11	11	2	10	0.063	
104329.446	-5.162	7.62	0	0	0	1	1	1	0.042	
111209.731	-4.639	21.65	3	1	3	4	0	4	0.126 Y	
112948.991	-4.773	52.67	6	0	6	5	1	4	0.082	
114179.077	-4.890	119.23	8	3	5	9	2	7	0.050 Y	

**Notes:** Frequency: rest frequency of the transitions in units MHz; log(I): logarithm of the line intensity;  $E_U/k_B$ : energy of the upper state of the transition in units K;  $Q_U$ : quantum numbers of the upper level;  $Q_L$ : quantum numbers of the lower level;  $\tau_0$ : optical depth at the center of the line, calculated with the parameters of best fit; flag indicating which transitions have been used to create the mean map.

**Table C.4.** Most unblended transitions of CH<sub>3</sub>CHO used to constrain the fit. Database used: JPL

Frequency MHz	log(I)	$E_U/k_B$		$Q_U$			$Q_L$			$\tau_0$
		K	J	$K_a$	$K_c$	J	$K_a$	$K_c$		
93580.909	-4.409	15.76	5	1	5	4	1	4	0.201 Y	
93595.235	-4.409	15.84	5	1	5	4	1	4	0.201	
96343.265	-4.859	50.11	5	4	2	4	4	1	0.050 Y	
96343.279	-4.859	50.11	5	4	1	4	4	0	0.050 Y	
96425.614	-4.454	22.40	5	2	4	4	2	3	0.000 Y	
96475.524	-4.454	23.05	5	2	3	4	2	2	0.164 Y	
96632.663	-4.450	22.99	5	2	3	4	2	2	0.166	
100127.164	-4.980	76.28	12	1	11	12	0	12	0.028 Y	
114940.175	-4.139	19.47	6	0	6	5	0	5	0.296 Y	
114959.902	-4.139	19.37	6	0	6	5	0	5	0.297 Y	
115634.704	-4.440	55.60	6	4	2	5	4	1	0.104 Y	

**Notes:** Frequency: rest frequency of the transitions in units MHz; log(I): logarithm of the line intensity;  $E_U/k_B$ : energy of the upper state of the transition in units K;  $Q_U$ : quantum numbers of the upper level;  $Q_L$ : quantum numbers of the lower level;  $\tau_0$ : optical depth at the center of the line, calculated with the parameters of best fit; flag indicating which transitions have been used to create the mean map.

**Table C.5.** Most unblended transitions of CH<sub>3</sub>OCH<sub>3</sub> used to constrain the fit. Database used: CDMS

Frequency MHz	log(I)	$E_U/k_B$		$Q_U$			$Q_L$			$\tau_0$
		K	J	$K_a$	$K_c$	J	$K_a$	$K_c$		
84631.897	-6.145	11.10	3	2	1	3	1	2	0.083 Y	
84632.274	-6.322	11.10	3	2	1	3	1	2	0.055 Y	
84634.421	-5.720	11.10	3	2	1	3	1	2	0.223 Y	
84636.757	-5.923	11.10	3	2	1	3	1	2	0.139 Y	
88706.231	-5.399	116.98	15	2	13	15	1	14	0.215 Y	
88706.231	-5.575	116.98	15	2	13	15	1	14	0.143 Y	
88707.704	-4.973	116.98	15	2	13	15	1	14	0.574 Y	
88709.177	-5.177	116.98	15	2	13	15	1	14	0.359 Y	
91473.762	-6.304	11.10	3	2	2	3	1	3	0.053	
91474.139	-6.605	11.10	3	2	2	3	1	3	0.027	
91476.607	-5.702	11.10	3	2	2	3	1	3	0.215	
91479.263	-6.128	11.09	3	2	2	3	1	3	0.081	
93664.597	-5.788	74.09	12	1	11	12	0	12	0.112	
93664.597	-6.089	74.09	12	1	11	12	0	12	0.056	
93666.463	-5.186	74.09	12	1	11	12	0	12	0.448	
93668.329	-5.612	74.09	12	1	11	12	0	12	0.168	
93854.438	-6.152	14.73	4	2	3	4	1	4	0.072 Y	
93854.560	-5.976	14.73	4	2	3	4	1	4	0.109 Y	
93857.113	-5.550	14.73	4	2	3	4	1	4	0.290 Y	
93859.727	-5.754	14.73	4	2	3	4	1	4	0.181 Y	



Table C.5. Continued.

Frequency MHz	log(I)	$E_U/k_B$		$Q_U$			$Q_L$			$\tau_0$
		K	J	$K_a$	$K_c$	J	$K_a$	$K_c$		
95729.780	-5.526	131.94	16	2	14	16	1	15	0.134	
95729.781	-5.827	131.94	16	2	14	16	1	15	0.067	
95731.253	-4.924	131.94	16	2	14	16	1	15	0.539	
95732.726	-5.350	131.94	16	2	14	16	1	15	0.202	
96847.241	-6.039	19.28	5	2	4	5	1	5	0.088	
96847.292	-6.340	19.28	5	2	4	5	1	5	0.044	
96849.890	-5.437	19.28	5	2	4	5	1	5	0.354	
96852.514	-5.863	19.28	5	2	4	5	1	5	0.133	
104175.880	-5.300	147.81	17	2	15	17	1	16	0.187 Y	
104175.880	-5.476	147.81	17	2	15	17	1	16	0.124 Y	
104177.381	-4.874	147.81	17	2	15	17	1	16	0.498 Y	
104178.881	-5.078	147.81	17	2	15	17	1	16	0.311 Y	
104700.568	-5.866	31.09	7	2	6	7	1	7	0.112	
104700.581	-6.167	31.09	7	2	6	7	1	7	0.056	
104703.262	-5.264	31.09	7	2	6	7	1	7	0.451	
104705.949	-5.690	31.09	7	2	6	7	1	7	0.169	
106775.679	-5.641	43.48	9	1	8	8	2	7	0.170	
106777.372	-5.436	43.48	9	1	8	8	2	7	0.273	
106779.061	-5.862	43.48	9	1	8	8	2	7	0.102	
106779.069	-6.038	43.48	9	1	8	8	2	7	0.068	
109571.391	-5.795	38.35	8	2	7	8	1	8	0.120	
109571.398	-5.619	38.35	8	2	7	8	1	8	0.181	
109574.127	-5.193	38.35	8	2	7	8	1	8	0.483	
109576.860	-5.397	38.35	8	2	7	8	1	8	0.302	
111782.249	-8.579	60.70	7	4	4	8	5	3	0.000	
111782.600	-5.305	25.28	7	0	7	6	1	6	0.400	
111783.117	-5.101	25.28	7	0	7	6	1	6	0.641	
111783.633	-5.527	25.28	7	0	7	6	1	6	0.240	
111783.634	-5.703	25.28	7	0	7	6	1	6	0.160	
111812.252	-5.663	169.97	18	3	15	18	2	16	0.064	
111812.253	-5.362	169.97	18	3	15	18	2	16	0.129	
111812.705	-7.413	60.70	7	4	4	8	5	3	0.002	
111813.812	-4.760	169.97	18	3	15	18	2	16	0.519	
111815.372	-5.186	169.97	18	3	15	18	2	16	0.194	
111817.549	-8.579	60.70	7	4	3	8	5	4	0.000	
113057.591	-5.190	153.24	17	3	14	17	2	15	0.214 Y	
113057.593	-5.366	153.24	17	3	14	17	2	15	0.142 Y	
113059.352	-4.764	153.24	17	3	14	17	2	15	0.571 Y	
113061.112	-4.968	153.24	17	3	14	17	2	15	0.356 Y	
114003.844	-5.427	164.60	18	2	16	18	1	17	0.113	
114003.844	-5.728	164.60	18	2	16	18	1	17	0.056	
114005.401	-4.825	164.60	18	2	16	18	1	17	0.455	
114006.957	-5.251	164.60	18	2	16	18	1	17	0.170	
115072.305	-5.731	46.51	9	2	8	9	1	9	0.126 Y	
115072.310	-6.032	46.51	9	2	8	9	1	9	0.063 Y	
115075.094	-5.129	46.51	9	2	8	9	1	9	0.505 Y	
115077.881	-5.554	46.51	9	2	8	9	1	9	0.189 Y	
115543.994	-5.760	14.63	5	1	5	4	0	4	0.146 Y	
115543.996	-6.061	14.63	5	1	5	4	0	4	0.073 Y	
115544.807	-5.158	14.63	5	1	5	4	0	4	0.585 Y	
115545.619	-5.584	14.63	5	1	5	4	0	4	0.219 Y	
115710.648	-5.161	225.94	21	3	18	21	2	19	0.135 Y	
115710.648	-5.337	225.94	21	3	18	21	2	19	0.090 Y	
115711.738	-4.735	225.94	21	3	18	21	2	19	0.361 Y	
115712.828	-4.939	225.94	21	3	18	21	2	19	0.226 Y	

**Notes:** Frequency: rest frequency of the transitions in units MHz; log(I): logarithm of the line intensity;  $E_U/k_B$ : energy of the upper state of the transition in units K;  $Q_U$ : quantum numbers of the upper level;  $Q_L$ : quantum numbers of the lower level;  $\tau_0$ : optical depth at the center of the line, calculated with the parameters of best fit.

**Table C.6.** Most unblended transitions of CH<sub>3</sub>COCH<sub>3</sub> used to constrain the fit. Database used: JPL

Frequency MHz	log(I)	$E_U/k_B$ K	$Q_U$			$Q_L$			$\tau_0$	
			$J$	$K_a$	$K_c$	$J$	$K_a$	$K_c$		
86536.667	-5.598	143.21	19	10	10	19	9	11	0.057	Y
88441.793	-5.636	110.59	17	7	10	17	6	11	0.056	
91634.636	-5.540	17.47	8	1	7	7	2	6	0.085	
91637.465	-5.540	17.47	8	2	7	7	1	6	0.085	
92735.670	-5.401	18.75	9	0	9	8	1	8	0.116	
92735.672	-5.401	18.75	9	1	9	8	0	8	0.116	
92743.361	-5.605	18.64	9	0	9	8	1	8	0.072	Y
92743.364	-5.827	18.64	9	1	9	8	0	8	0.043	Y
95669.941	-5.529	156.20	20	10	11	20	9	12	0.059	
98352.377	-6.273	9.36	5	5	1	4	4	1	0.015	
98455.636	-6.079	9.24	5	5	1	4	4	0	0.023	Y
99052.509	-5.712	76.66	15	4	11	15	3	12	0.045	
99052.559	-5.712	76.66	15	5	11	15	4	12	0.045	
99266.432	-5.854	9.21	5	5	0	4	4	1	0.039	
99422.031	-8.712	150.83	19	12	7	18	15	4	0.000	Y
99422.076	-5.806	63.35	14	3	11	14	2	12	0.038	Y
99422.084	-5.806	63.35	14	4	11	14	3	12	0.038	Y
99721.506	-5.951	50.93	13	2	11	13	1	12	0.028	
99721.507	-5.951	50.93	13	3	11	13	2	12	0.028	
99900.091	-6.153	50.83	13	2	11	13	1	12	0.017	
99900.092	-6.375	50.83	13	3	11	13	2	12	0.010	
100350.304	-5.554	19.75	8	2	6	7	3	5	0.075	
101426.663	-5.819	21.97	9	1	8	8	2	7	0.040	Y
101426.759	-5.995	21.97	9	1	8	8	2	7	0.026	Y
101427.041	-6.296	21.97	9	2	8	8	1	7	0.013	Y
101427.129	-5.995	21.97	9	2	8	8	1	7	0.026	Y
101451.058	-5.393	21.87	9	1	8	8	2	7	0.107	
101451.446	-5.393	21.87	9	2	8	8	1	7	0.107	
101475.332	-5.597	21.77	9	1	8	8	2	7	0.067	
101475.733	-5.819	21.77	9	2	8	8	1	7	0.040	
102554.696	-5.271	23.20	10	0	10	9	1	9	0.139	
102554.696	-5.271	23.20	10	1	10	9	0	9	0.139	
102562.281	-5.697	23.09	10	0	10	9	1	9	0.052	
102562.282	-5.475	23.09	10	1	10	9	0	9	0.087	
102901.559	-5.762	16.66	7	4	4	6	3	3	0.045	
106273.673	-5.505	133.47	19	7	12	19	6	13	0.059	Y
106274.498	-5.505	133.47	19	8	12	19	7	13	0.059	Y
107227.738	-6.012	100.79	17	5	12	17	4	13	0.019	Y
107227.778	-6.489	100.79	17	6	12	17	5	13	0.006	Y
107227.803	-6.188	100.79	17	5	12	17	4	13	0.013	Y
107227.843	-6.188	100.79	17	6	12	17	5	13	0.013	Y
107376.810	-5.585	100.73	17	5	12	17	4	13	0.053	
107376.851	-5.585	100.73	17	6	12	17	5	13	0.053	
107797.720	-5.649	85.66	16	4	12	16	3	13	0.047	
107797.728	-5.649	85.66	16	5	12	16	4	13	0.047	
107961.851	-6.073	85.59	16	4	12	16	3	13	0.017	
107961.859	-5.852	85.59	16	5	12	16	4	13	0.029	
107967.774	-6.171	71.55	15	3	12	15	2	13	0.014	
107967.775	-6.648	71.55	15	4	12	15	3	13	0.004	
107967.865	-6.347	71.55	15	3	12	15	2	13	0.009	
107967.866	-6.347	71.55	15	4	12	15	3	13	0.009	
108387.594	-5.616	21.59	8	3	5	7	4	4	0.060	
108434.510	-5.887	58.15	14	2	12	14	1	13	0.029	
108434.511	-5.887	58.15	14	3	12	14	2	13	0.029	
109994.365	-5.732	12.96	6	5	2	5	4	1	0.046	Y
110189.150	-5.401	24.56	9	2	7	8	3	6	0.096	
110208.702	-5.401	24.56	9	3	7	8	2	6	0.096	
110490.618	-5.795	21.42	8	4	5	7	3	4	0.039	

**Table C.6.** Continued.

Frequency MHz	log(I)	$E_U/k_B$		$Q_U$			$Q_L$			$\tau_0$
		K	J	$K_a$	$K_c$	J	$K_a$	$K_c$		
110987.131	-5.876	23.14	8	4	4	7	5	3	0.032	
112365.987	-6.059	28.22	11	1	11	10	0	10	0.020	
112365.987	-5.582	28.22	11	0	11	10	1	10	0.061	
112366.032	-5.758	28.22	11	0	11	10	1	10	0.041	
112366.032	-5.758	28.22	11	1	11	10	0	10	0.041	
112381.029	-5.581	28.01	11	1	11	10	0	10	0.061	
112381.029	-5.359	28.01	11	0	11	10	1	10	0.102	
114469.404	-5.429	164.18	21	8	13	21	7	14	0.060	
114469.992	-5.429	164.18	21	9	13	21	8	14	0.060	
115115.835	-5.451	145.61	20	7	13	20	6	14	0.060	
115115.980	-5.451	145.61	20	8	13	20	7	14	0.060	

**Notes:** Frequency: rest frequency of the transitions in units MHz; log(I): logarithm of the line intensity;  $E_U/k_B$ : energy of the upper state of the transition in units K;  $Q_U$ : quantum numbers of the upper level;  $Q_L$ : quantum numbers of the lower level;  $\tau_0$ : optical depth at the center of the line, calculated with the parameters of best fit; flag indicating which transitions have been used to create the mean map.

**Table C.7.** Most unblended transitions of  $C_2H_5OH$  used to constrain the fit. Database used: CDMS

Frequency MHz	log(I)	$E_U/k_B$		$Q_U$			$Q_L$			$\tau_0$	
		K	J	$K_a$	$K_c$	J	$K_a$	$K_c$			
85265.488	-5.151	17.50	6	0	6	5	1	5	0.157	Y	
86311.282	-5.250	74.28	5	2	4	4	2	3	0.092		
86516.482	-5.648	93.82	5	4	2	4	4	1	0.033		
86516.573	-5.648	93.82	5	4	1	4	4	0	0.033		
86555.887	-5.617	88.94	5	4	2	4	4	1	0.036		
86555.986	-5.617	88.94	5	4	1	4	4	0	0.036		
86947.280	-4.743	108.18	15	2	13	15	1	14	0.248	Y	
87716.120	-5.263	17.62	5	2	4	5	1	5	0.118		
91485.187	-5.166	22.65	6	2	5	6	1	6	0.137	Y	
91737.135	-4.784	115.42	11	0	11	11	1	11	0.207		
92156.494	-4.767	273.74	22	1	21	22	2	21	0.096		
93568.917	-4.749	292.45	23	1	22	23	2	22	0.089		
94696.389	-4.625	158.52	15	0	15	15	1	15	0.232		
95416.567	-4.599	171.24	16	0	16	16	1	16	0.229		
95924.494	-4.582	184.74	17	0	17	17	1	17	0.222	Y	
96230.720	-4.732	353.16	26	1	25	26	2	25	0.066		
96301.854	-4.570	199.01	18	0	18	18	1	18	0.211		
97139.033	-4.558	263.84	22	0	22	22	1	22	0.155		
97263.633	-4.562	281.98	23	0	23	23	1	23	0.140	Y	
97535.982	-4.552	246.48	21	1	21	21	0	21	0.171		
97536.860	-4.559	281.99	23	1	23	23	0	23	0.140		
98983.556	-4.619	146.69	14	1	14	14	0	14	0.239		
99439.978	-4.703	353.24	26	2	25	26	1	25	0.069		
99524.061	-4.578	141.48	17	3	14	17	2	15	0.269		
100194.322	-4.969	75.04	6	1	6	5	1	5	0.152	Y	
100358.937	-4.588	126.84	16	3	13	16	2	14	0.280		
100365.042	-4.925	79.72	6	1	6	5	1	5	0.164		
100452.033	-4.687	312.06	24	2	23	24	1	23	0.087		
100452.089	-7.897	385.51	26	5	21	26	5	21	0.000		
100990.113	-5.008	35.21	8	2	7	8	1	8	0.169		
101873.097	-4.548	173.44	19	3	16	19	2	17	0.239		
102282.773	-4.676	274.00	22	2	21	22	1	21	0.106		
102283.550	-4.597	113.10	15	3	12	15	2	13	0.289		
103452.151	-4.993	79.25	6	2	5	5	2	4	0.136		
103608.576	-4.674	256.14	21	2	20	21	1	20	0.116		
103890.656	-5.197	93.93	6	4	3	5	4	2	0.078		
103891.101	-5.197	93.93	6	4	2	5	4	1	0.078		
103895.500	-5.088	90.18	6	3	4	5	3	3	0.103		

**Table C.7.** Continued.

Frequency MHz	log(I)	$E_U/k_B$		$Q_U$			$Q_L$			$\tau_0$	
		K	J	$K_a$	$K_c$	J	$K_a$	$K_c$			
105162.141	-4.789	98.87	9	1	9	9	0	9	0.194	Y	
105337.356	-4.528	190.75	20	3	17	20	2	18	0.222		
106676.441	-4.916	76.13	6	1	5	5	1	4	0.160		
106723.565	-4.939	42.73	9	2	8	9	1	9	0.180		
106931.229	-4.698	222.75	19	2	18	19	1	18	0.126	Y	

**Notes:** Frequency: rest frequency of the transitions in units MHz; log(I): logarithm of the line intensity;  $E_U/k_B$ : energy of the upper state of the transition in units K;  $Q_U$ : quantum numbers of the upper level;  $Q_L$ : quantum numbers of the lower level;  $\tau_0$ : optical depth at the center of the line, calculated with the parameters of best fit; flag indicating which transitions have been used to create the mean map.

**Table C.8.** Most unblended transitions of  $gGg'-(CH_2OH)_2$  used to constrain the fit. Database used: CDMS

Frequency MHz	log(I)	$E_U/k_B$		$Q_U$			$Q_L$			$\tau_0$	
		K	J	$K_a$	$K_c$	J	$K_a$	$K_c$			
86429.874	-5.272	74.23	17	3	15	17	2	16	0.014	Y	
93016.853	-5.068	21.81	9	3	7	8	3	6	0.027	Y	
98481.089	-5.024	115.43	21	4	18	21	3	19	0.017	Y	
102758.214	-4.819	25.60	11	1	11	10	1	10	0.043	Y	
103538.434	-4.961	29.56	10	4	6	9	4	5	0.030	Y	
108867.794	-4.739	86.56	17	6	12	17	5	13	0.035	Y	
108867.930	-5.140	63.13	14	6	8	14	5	10	0.016	Y	
113997.038	-4.939	34.43	11	4	7	10	4	6	0.028	Y	

**Notes:** Frequency: rest frequency of the transitions in units MHz; log(I): logarithm of the line intensity;  $E_U/k_B$ : energy of the upper state of the transition in units K;  $Q_U$ : quantum numbers of the upper level;  $Q_L$ : quantum numbers of the lower level;  $\tau_0$ : optical depth at the center of the line, calculated with the parameters of best fit; flag indicating which transitions have been used to create the mean map.

**Table C.9.** Most unblended transitions of  $aGg'-(CH_2OH)_2$  used to constrain the fit. Database used: CDMS

Frequency MHz	log(I)	$E_U$		$Q_U$			$Q_L$			$\tau_0$	
		K	J	$K_a$	$K_c$	J	$K_a$	$K_c$			
84439.522	-4.689	13.25	8	0	8	7	0	7	0.126	Y	
85521.565	-4.868	25.71	9	4	6	8	4	5	0.077		
85522.221	-6.560	102.24	20	2	18	19	4	15	0.001		
86655.610	-4.633	18.96	9	1	8	8	1	7	0.135		
86660.118	-4.699	22.37	9	3	6	8	3	5	0.114	Y	
88366.963	-4.572	21.45	10	1	10	9	1	9	0.151	Y	
88745.339	-4.702	21.40	10	0	10	9	0	9	0.111		
88986.213	-4.907	21.47	8	4	5	7	4	4	0.069		
89708.194	-4.728	18.09	8	3	5	7	3	4	0.106		
90423.320	-5.094	24.01	10	1	9	9	2	8	0.043		
91539.725	-4.776	15.88	8	2	6	7	2	5	0.094		
95354.813	-5.007	53.52	10	8	3	9	8	2	0.034	Y	
95354.813	-5.116	53.52	10	8	2	9	8	1	0.043	Y	
96258.221	-4.602	23.412	10	1	9	9	1	8	0.128		
96259.944	-5.614	106.12	20	4	17	20	3	18	0.008		
97359.027	-4.547	19.37	9	2	8	8	2	7	0.146	Y	
97558.756	-4.669	26.83	10	3	7	9	3	6	0.106		
99082.055	-4.804	35.13	9	6	4	8	6	3	0.057	Y	
99082.055	-4.913	35.13	9	6	3	8	6	2	0.073	Y	
99509.149	-4.608	24.80	10	2	8	9	2	7	0.121		
105701.002	-4.364	28.32	11	1	10	10	1	9	0.197	Y	
106088.917	-4.510	39.38	11	5	6	10	5	5	0.132	Y	
109489.186	-4.540	34.16	10	5	5	9	5	4	0.123		
111579.436	-4.355	25.66	11	1	11	10	1	10	0.192		

**Notes:** Frequency: rest frequency of the transitions in units MHz; log(I): logarithm of the line intensity;  $E_U$ : energy of the upper state of the transition in units K;  $Q_U$ : quantum numbers of the upper level;  $Q_L$ : quantum numbers of the lower level;  $\tau_0$ : optical depth at the center of the line, calculated with the parameters of best fit; flag indicating which transitions have been used to create the mean map.

**Table C.10.** Most unblended transitions of  $\text{CH}_3\text{CN } v_8 = 1$  used to constrain the fit. Database used: CDMS

Frequency MHz	log(I)	$E_U/k_B$ K	$Q_U$			$Q_L$			$\tau_0$	
			J	$K_a$	$K_c$	J	$K_a$	$K_c$		
92175.520	-4.029	532.85	5	1	3	4	-1	3	0.150	Y
92247.240	-4.176	594.26	5	-2	2	4	2	2	0.096	Y
92247.240	-4.176	594.26	5	2	2	4	-2	2	0.096	Y
92249.653	-4.552	600.11	5	-4	3	4	4	3	0.040	Y
92249.653	-4.552	600.11	5	4	3	4	-4	3	0.040	Y
92256.288	-4.067	559.50	5	1	2	4	1	2	0.131	
92258.412	-4.249	563.40	5	3	3	4	3	3	0.086	
92261.440	-4.020	539.03	5	0	2	4	0	2	0.152	
92263.992	-4.098	540.98	5	2	3	4	2	3	0.126	
92353.516	-4.028	532.87	5	-1	3	4	1	3	0.150	Y
110609.594	-3.793	538.16	6	-1	3	5	1	3	0.214	Y
110706.340	-3.831	564.82	6	1	2	5	1	2	0.187	
110709.354	-3.950	568.72	6	3	3	5	3	3	0.141	
110712.220	-3.789	544.35	6	0	2	5	0	2	0.213	Y
110716.278	-3.843	540.98	6	2	3	5	2	3	0.188	
110823.126	-3.792	532.87	6	1	3	5	-1	3	0.214	Y

**Notes:** Frequency: rest frequency of the transitions in units MHz; log(I): logarithm of the line intensity;  $E_U/k_B$ : energy of the upper state of the transition in units K;  $Q_U$ : quantum numbers of the upper level;  $Q_L$ : quantum numbers of the lower level;  $\tau_0$ : optical depth at the center of the line, calculated with the parameters of best fit; flag indicating which transitions have been used to create the mean map.

**Table C.11.** Most unblended transitions of  $^{13}\text{CH}_3\text{CN}$  used to constrain the fit. Database used: CDMS

Frequency MHz	log(I)	$E_U/k_B$ K	$Q_U$		$Q_L$		$\tau_0$	
			J	K	J	K		
89324.555	-3.238	41.54	5	2	4	2	0.179	Y
89329.600	-3.149	15.75	5	1	4	1	0.248	Y
89331.282	-3.121	8.58	5	0	4	0	0.276	Y
107178.424	-2.808	77.36	6	3	5	3	0.320	Y
107188.500	-2.983	41.54	6	2	5	2	0.261	Y
107194.550	-2.913	20.04	6	1	5	1	0.347	Y
107196.570	-2.890	12.87	6	0	5	0	0.381	Y

**Notes:** Frequency: rest frequency of the transitions in units MHz; log(I): logarithm of the line intensity;  $E_U/k_B$ : energy of the upper state of the transition in units K;  $Q_U$ : quantum numbers of the upper level;  $Q_L$ : quantum numbers of the lower level;  $\tau_0$ : optical depth at the center of the line, calculated with the parameters of best fit; flag indicating which transitions have been used to create the mean map.

**Table C.12.** Most unblended transitions of  $\text{CH}_3^{13}\text{CN}$  used to constrain the fit. Database used: CDMS

Frequency MHz	log(I)	$E_U/k_B$ K	$Q_U$		$Q_L$		$\tau_0$	
			J	K	J	K		
91925.704	-3.070	77.62	5	3	4	3	0.578	Y
91934.531	-3.201	41.86	5	2	4	2	0.736	Y
110309.800	-2.771	82.92	6	3	5	3	0.891	Y

**Notes:** Frequency: rest frequency of the transitions in units MHz; log(I): logarithm of the line intensity;  $E_U/k_B$ : energy of the upper state of the transition in units K;  $Q_U$ : quantum numbers of the upper level;  $Q_L$ : quantum numbers of the lower level;  $\tau_0$ : optical depth at the center of the line, calculated with the parameters of best fit; flag indicating which transitions have been used to create the mean map.

**Table C.13.** Most unblended transitions of C<sub>2</sub>H<sub>3</sub>CN used to constrain the fit. Database used: CDMS

Frequency MHz	log(I)	E <sub>U</sub> /k <sub>B</sub>		Q <sub>U</sub>			Q <sub>L</sub>			τ <sub>0</sub>	
		K	J	K <sub>a</sub>	K <sub>c</sub>	J	K <sub>a</sub>	K <sub>c</sub>			
85715.423	-3.937	29.22	9	2	7	8	2	6	0.170	Y	
94913.115	-3.900	59.72	10	4	7	9	4	6	0.138	Y	
94913.227	-3.900	59.72	10	4	6	9	4	5	0.138	Y	
94913.958	-3.978	79.18	10	5	6	9	5	5	0.102	Y	
94913.959	-3.978	79.18	10	5	5	9	5	4	0.102	Y	
95325.476	-3.801	33.80	10	2	8	9	2	7	0.203		
96982.442	-3.764	27.81	10	1	9	9	1	8	0.226	Y	
101637.231	-3.686	31.49	11	1	11	10	1	10	0.252	Y	
103575.395	-3.664	30.00	11	0	11	10	0	10	0.263	Y	
104960.538	-3.680	38.84	11	2	9	10	2	8	0.237	Y	
113657.635	-3.578	44.19	12	2	11	11	2	10	0.268	Y	
113904.798	-3.712	89.66	12	5	7	11	5	6	0.147	Y	
113904.798	-3.712	89.66	12	5	8	11	5	7	0.147	Y	
113939.397	-3.607	55.06	12	3	10	11	3	9	0.233		
114621.567	-3.571	44.35	12	2	10	11	2	9	0.270		

**Notes:** Frequency: rest frequency of the transitions in units MHz; log(I): logarithm of the line intensity; E<sub>U</sub>/k<sub>B</sub>: energy of the upper state of the transition in units K; Q<sub>U</sub>: quantum numbers of the upper level; Q<sub>L</sub>: quantum numbers of the lower level; τ<sub>0</sub>: optical depth at the center of the line, calculated with the parameters of best fit; flag indicating which transitions have been used to create the mean map.

**Table C.14.** Most unblended transitions of C<sub>2</sub>H<sub>3</sub>CN used to constrain the fit. Database used: CDMS

Frequency MHz	log(I)	E <sub>U</sub> /k <sub>B</sub>		Q <sub>U</sub>			Q <sub>L</sub>			τ <sub>0</sub>	
		K	J	K <sub>a</sub>	K <sub>c</sub>	J	K <sub>a</sub>	K <sub>c</sub>			
86819.845	-3.738	24.09	10	1	10	9	1	9	0.822		
88323.735	-3.719	23.48	10	0	10	9	0	9	0.850	Y	
89297.660	-3.732	28.08	10	2	9	9	2	8	0.782	Y	
89628.485	-3.760	33.70	10	3	8	9	3	7	0.695		
91549.112	-3.694	25.35	10	1	9	9	1	8	0.855		
96919.762	-3.603	28.13	11	0	11	10	0	10	0.972	Y	
98523.872	-3.799	68.47	11	6	5	10	6	4	0.428	Y	
98523.872	-3.799	68.47	11	6	6	10	6	5	0.428	Y	
98524.672	-3.892	82.92	11	7	5	10	7	4	0.304	Y	
98524.672	-3.892	82.92	11	7	4	10	7	3	0.304	Y	
98532.084	-4.018	99.59	11	8	4	10	8	3	0.197	Y	
98532.084	-4.018	99.59	11	8	3	10	8	2	0.197	Y	
98533.987	-3.729	56.23	11	5	6	10	5	5	0.560	Y	
98533.987	-3.729	56.23	11	5	7	10	5	6	0.560	Y	
98564.827	-3.675	46.22	11	4	8	10	4	7	0.692	Y	
98566.792	-3.675	46.22	11	4	7	10	4	6	0.692	Y	
98701.101	-3.635	38.44	11	3	8	10	3	7	0.811	Y	
99681.461	-3.599	33.04	11	2	9	10	2	8	0.914		
104051.276	-3.514	33.67	12	1	12	11	1	11	1.062		
107485.160	-3.741	88.09	12	7	6	11	7	5	0.378		
107485.160	-3.741	88.09	12	7	5	11	7	4	0.378		
107486.949	-3.665	73.63	12	6	6	11	6	5	0.512		
107486.949	-3.665	73.63	12	6	7	11	6	6	0.512		
107491.574	-3.840	104.76	12	8	5	11	8	4	0.260		
107491.574	-3.840	104.76	12	8	4	11	8	3	0.260		
107502.432	-3.605	61.40	12	5	7	11	5	6	0.654	Y	
107502.432	-3.605	61.40	12	5	8	11	5	7	0.654	Y	
107503.686	-3.971	123.64	12	9	4	11	9	3	0.163	Y	
107503.686	-3.971	123.64	12	9	3	11	9	2	0.163	Y	
109650.295	-3.470	35.45	12	1	11	11	1	10	1.097		

**Notes:** Frequency: rest frequency of the transitions in units MHz;  $\log(I)$ : logarithm of the line intensity;  $E_U/k_B$ : energy of the upper state of the transition in units K;  $Q_U$ : quantum numbers of the upper level;  $Q_L$ : quantum numbers of the lower level;  $\tau_0$ : optical depth at the center of the line, calculated with the parameters of best fit; flag indicating which transitions have been used to create the mean map.

**Table C.15.** Most unblended transitions of  $C_2H_5^{13}CN$  used to constrain the fit. Database used: CDMS

Frequency MHz	$\log(I)$	$E_U/k_B$ K	$Q_U$			$Q_L$			$\tau_0$	
			$J$	$K_a$	$K_c$	$J$	$K_a$	$K_c$		
89116.016	-3.972	63.61	10	6	5	9	6	4	0.012	Y
89116.016	-3.972	63.61	10	6	4	9	6	3	0.012	Y
89235.646	-3.774	33.58	10	3	7	9	3	6	0.022	Y
96452.595	-3.617	27.99	11	0	11	10	0	10	0.031	Y
100109.732	-3.591	30.04	11	1	10	10	1	9	0.031	Y
109101.845	-3.485	35.28	12	1	11	11	1	10	0.036	Y
112101.543	-3.431	38.90	13	1	13	12	1	12	0.039	Y
115871.121	-3.561	79.02	13	6	8	12	6	7	0.023	Y
115871.122	-3.561	79.02	13	6	7	12	6	6	0.023	Y
115871.741	-3.709	110.14	13	8	6	12	8	5	0.014	Y
115871.741	-3.709	110.14	13	8	5	12	8	4	0.014	Y

**Notes:** Frequency: rest frequency of the transitions in units MHz;  $\log(I)$ : logarithm of the line intensity;  $E_U/k_B$ : energy of the upper state of the transition in units K;  $Q_U$ : quantum numbers of the upper level;  $Q_L$ : quantum numbers of the lower level;  $\tau_0$ : optical depth at the center of the line, calculated with the parameters of best fit.

## Appendix D: Moment maps of low-energy transitions

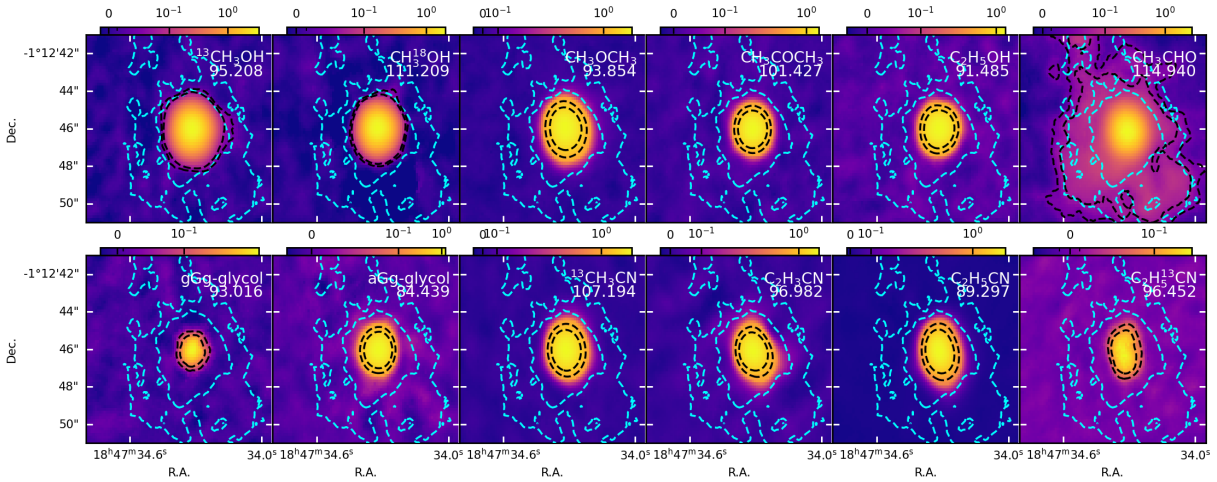


**Fig. D.1.** Moment-0 maps of low-energy transitions for the molecular species analyzed in this paper. We do not include  $CH_3OH$   $vt=1$ ,  $CH_3CN$   $v8=1$ , and  $CH_3^{13}CN$  since there were not available transitions with  $E_U/k_B < 30$  K. The moment-0 maps are not normalised to the peak intensity (i.e. to 1, as done for the mean maps shown in Fig. 1). The units are  $Jy/beam km s^{-1}$ . The black-dashed contours are the  $5rms$  and  $10rms$  contour of the color-scale image, while the cyan-dashed contours are the  $5rms$  and  $10rms$  contours of the mean map of  $CH_3CHO$  shown in Fig. 1.